

# Luminescence based temperature bio-imaging: Status, challenges, and perspectives

Cite as: Appl. Phys. Rev. **8**, 011317 (2021); doi: [10.1063/5.0030295](https://doi.org/10.1063/5.0030295)  
 Submitted: 22 September 2020 · Accepted: 30 December 2020 ·  
 Published Online: 9 March 2021



View Online



Export Citation



CrossMark

A. Bednarkiewicz,<sup>1,a)</sup>  J. Drabik,<sup>1</sup>  K. Trejgis,<sup>1</sup>  D. Jaque,<sup>2,3,b)</sup>  E. Ximendes,<sup>2,3,c)</sup>  and L. Marciniak<sup>1,a)</sup> 

## AFFILIATIONS

<sup>1</sup>Institute of Low Temperature and Structure Research, Polish Academy of Sciences, Okólna 2, 50-422 Wrocław, Poland

<sup>2</sup>NanoBIC, Departamento de Física de Materiales, Facultad de Ciencias, Universidad Autónoma de Madrid, 28049, Madrid, Spain

<sup>3</sup>Institute for Biomedical Research Ramon y Cajal (IRYCIS), Ctra. Colmenar km. 9.100, Madrid 28034, Spain

<sup>a)</sup>Authors to whom correspondence should be addressed: [a.bednarkiewicz@intibs.pl](mailto:a.bednarkiewicz@intibs.pl) and [l.marciniak@intibs.pl](mailto:l.marciniak@intibs.pl)

<sup>b)</sup>Electronic address: [erving.ximendes@uam.es](mailto:erving.ximendes@uam.es)

<sup>c)</sup>Electronic address: [daniel.jaque@uam.es](mailto:daniel.jaque@uam.es)

## ABSTRACT

The only way to get thermal images of living organisms without perturbing them is to use luminescent probes with temperature-dependent spectral properties. The acquisition of such thermal images becomes essential to distinguish various states of cells, to monitor thermogenesis, to study cellular activity, and to control hyperthermia therapy. Current efforts are focused on the development and optimization of luminescent reporters such as small molecules, proteins, quantum dots, and lanthanide-doped nanoparticles. However, much less attention is devoted to the methods and technologies that are required to image temperature distribution at both *in vitro* or *in vivo* levels. Indeed, rare examples can be found in the scientific literature showing technologies and materials capable of providing reliable 2D thermal images of living organisms. In this review article, examples of 2D luminescence thermometry are presented alongside new possibilities and directions that should be followed to achieve the required level of simplicity and reliability that ensure their future implementation at the clinical level. This review will inspire specialists in chemistry, physics, biology, medicine, and engineering to collaborate with materials scientists to jointly develop novel more accurate temperature probes and enable mapping of temperature with simplified technical means.

Published under license by AIP Publishing. <https://doi.org/10.1063/5.0030295>

## TABLE OF CONTENTS

I. INTRODUCTION .....	1
II. METHODOLOGIES AND TECHNICAL ASPECTS OF T READOUT.....	6
III. INFLUENCE OF TISSUE/SAMPLE SPECTROSCOPY ON THE TEMPERATURE READOUT.....	6
IV. TEMPERATURE DETECTION READOUT.....	8
A. Absolute intensity of luminescence .....	9
B. Spectral shift of the emission band or absorption edge .....	14
C. Relative emission bands intensities under single excitation .....	16
D. Relative emission band(s) intensities under double excitation.....	27
E. Relative emission intensity under two excitation bands.....	29
F. Spectral anisotropy .....	30
G. Luminescence decays .....	32

H. Emission bandwidth.....	38
I. Absorption edge shift.....	38
V. SUMMARY .....	38
VI. OUTLOOK AND PERSPECTIVES.....	38

## I. INTRODUCTION

Recent advances in materials science aim to address numerous challenges set by biologists and medical doctors. “Smart” drug delivery nanoparticles (NPs), specialized multiplexed luminescent labels [e.g., quantum dots (QDs), lanthanide doped nanoparticles, nanodiamonds, etc.] for imaging and flow-cytometry,<sup>1,2</sup> photostable multicolor luminescence labels for super-resolution imaging,<sup>3</sup> improved magnetic resonance imaging (MRI),<sup>4</sup> computer tomography (CT),<sup>5,6</sup> optical coherent tomography (OCT),<sup>7</sup> ultrasound imaging (USG)<sup>8</sup> contrast nanoagents, and many other purposefully designed materials have revolutionized current possibilities in the understanding of biology, feedback controlled therapies, and personalized medicine.<sup>9</sup> In

particular, optical and remotely read, sub-millimeter spatial resolution temperature mapping is very appealing due to the fact that the temperature is a fundamental quantity that is related to many natural biological processes (e.g., activity of enzymes) and that is a prerequisite tool to feedback control hyperthermia therapy of cancer.

The fundamental question regarding remote temperature sensing and imaging in biology is: why is it important to know the *in vivo*/*in vitro* distribution of temperature? As known, increased temperature modulates numerous enzymatic and biochemical processes, through modifying the proteins or enzyme activity,<sup>10,11</sup> gene expression,<sup>12,13</sup> or cell signaling.<sup>14</sup> Temperature affects membrane stiffness, and this one modulates the permeability of the cell membrane to exogenous compounds or nanomaterials. It was suggested that up to 50 °C can be reached locally in mitochondria as compared to the cytoplasm.<sup>15</sup> Despite the fact that these results are striking, it is still not clear why such a high temperature is important and how this exact value and temperature gradients affect biological systems. Furthermore, theoretical considerations have been questioning the interpretation currently given to temperature heterogeneities measured in single living cells at the nanoscale.<sup>16,17</sup> As a consequence, the temperature reading or mapping at the tissue or subcellular level could be important not only to diagnose diseases, evaluate therapeutic efficiency of drugs, and evaluate the origins of toxicity, but also may shed some light on the extent of validity of thermodynamic considerations when evaluating cellular processes in individual cells and in tissues. Temperature imaging is particularly compatible and important in combination with fluorescence microscopy imaging in biology, because a morphology (e.g., tissue structures and organelle location in cell) can be co-localized with cell machinery functioning (e.g., Ca influxed in neurons and protein activity). Despite the great interest and some progress in recent years, there are still not too many examples, where the temperature is mapped *in vivo* or *in vitro*. Apart from the biological suitability of temperature mapping and sensing, many other technological processes require evaluation of temperature distribution (e.g., electronic circuits, rotating mechanical elements, etc.) in a remote manner<sup>18,19</sup> with sub-millimeter optical resolution.

While conventional temperature recording (e.g., with thermocouples or thermistors) or imaging (with bolometric cameras) techniques are robust and reliable for most types of applications, the remote temperature detection in biology and medicine is definitely technically much more challenging. The existing techniques are not suitable to satisfy sophisticated requirements imposed by the thermometric *in vitro* microscopy or by the body *in vivo* temperature mapping. This is true mostly because they are either invasive or they prohibit temperature detection from below the skin surface. On the other hand, luminescent imaging *in vitro* and *in vivo* is a well-established method to enhance the visualization contrast of biological specimens. Numerous fluorescent labels (e.g., organic dyes, lanthanide chelates, quantum dots, and lanthanide doped nanoparticles) have been successfully used for luminescent imaging because they offer:

- (i) unprecedented optical resolution with subcellular resolution or even below the diffraction limit of light,
- (ii) penetration of both excitation and emission light through the skin, thus enabling remote/noninvasive or minimally invasive measurement from the volume of the sample,
- (iii) specific targeting of molecular, cellular, or tissue components,
- (iv) large (anti)-Stokes spectral shift enabling to easily distinguish optical stimulus from the photoluminescence,
- (v) fast response to study dynamic processes,

- (vi) quantitative evaluation of intermolecular energy transfer and interaction [like Förster resonant energy transfer (FRET) detection of biomolecule structure and reorientation, DNA hybridization, enzyme activity, etc.].

The spectral features of the same fluorescent probes are very often susceptible to variation in the local temperature, which, in turn, makes them very promising for constructing remote temperature sensing and imaging systems, with no additional investments in detection equipment.

Many of these luminescent materials (e.g., polymers, quantum dots, lanthanide and transition metal doped nanoparticles, metal complexes, diamonds, organic dyes, fluorescent proteins, hybrid materials, and metal nanoparticles, which have been extensively published and reviewed<sup>20</sup>) display temperature dependence, which made them candidates as actual temperature reporters. The susceptibility of the spectroscopic properties to the temperature change is however only a prerequisite condition and does not necessarily mean that the material is suitable for temperature imaging in biology and medicine, because such applications put very strict and interdependent requirements on the materials and methods depending on target applications.<sup>21–23</sup> Such luminescent thermometer (LT) reporters should satisfy numerous requirements to become suitable for detection and temperature imaging *in vitro* or *in vivo*. First of all, they should either passively diffuse into cells and tissues or be actively targeted to biomolecules, biostructures, cells, and tissues. While the former requirement put demands on the size of the labels to stay below 50-nm hydrodynamic diameter, the latter one requires additionally appropriate surface biofunctionalization, which has been reviewed in scientific literature.<sup>24–26</sup> The nanometric size, together with the narrow size distribution of optical thermometers, is very important for biomedical applications for one another reason. When the collection of nanothermometers strongly varies in their particle diameters,<sup>27</sup> not only different spectral properties and thus temperature response may be expected, but also the local heat transfer between the object of interest and emissive centers will vary thus also introducing artificial temperature fluctuations. The LT reporters should also be biocompatible [usually a SiO<sub>2</sub>, polyethylene glycol (PEG) shell is used to secure this] and biologically safe, with non-existent or limited nanotoxicity<sup>28</sup> at reasonable doses. They should not undergo dissolution or degradation in the harsh environment within tissues, cells, or cellular compartments (e.g., lysosomes). The LTs should be resistant to local chemical and physical conditions other than temperature,<sup>29–32</sup> for example, they should not behave differently in different pH, viscosity, presence of H<sub>2</sub>O, or radicals, as these factors are very difficult to quantify and thus are not easy to include in data analysis or correction. Moreover, the temperature readout should not depend on the LT reporter density (e.g., owing to spectral self-absorption) or the spectral signatures of the T probes should not spectrally overlap with the spectral properties of tissue/cell components—e.g., with variable oxy/deoxy hemoglobin or with the autofluorescence of the tissue components under short wavelength photoexcitation, as these two factors increase the background level and hinder quantitative analysis. The LT reporter dose is critically important from the perspective of toxicity, luminescence brightness, and signal quality. Additionally, the temperature reporters must provide a fluorescent signal, which assures good metrological conditions, i.e.,

- (i) high relative sensitivity  $S_R$  of T determination as well as high readout accuracy, trueness, precision, and measurement resolution (better than 0.1 °C),

- (ii) fast response  $<0.1$  s to kinetic changes of temperatures,
- (iii) high brightness, which is further related to technical simplicity and feasibility to read the luminescence signal,
- (iv) no accidental heating or other parasitic impact on the biological samples,
- (v) high photostability of luminescence,
- (vi) independence of readout from, *in situ* unknown excitation intensity (especially troublesome for non-linear emission such as up-conversion), and
- (vii) high luminescence signal to background (or autofluorescence) noise ratio. The feasibility to reliably quantify and map temperature is also related to the other phenomena, such as anti-Stokes emission enabling to avoid autofluorescence, photoexcitation, and scattering of emitted light in heterogeneous tissues, long and temperature dependent luminescence lifetimes and the monotonic response of LT probes to temperature.

Currently, a great challenge is also to prepare high brightness near infrared (NIR) emitting luminescent labels, which should enable deeper light penetration into solid tissue samples and allow for *in vivo* 3D imaging of specific tissue types (e.g., cancer) or biochemical/physical quantities (pH, temperature, etc.).<sup>22,33,34</sup> These NIR reporters are especially difficult to make due to efficient luminescence quenching by ligand and medium molecules.<sup>35–37</sup> While most of the fluorescent species are vulnerable to such high energy vibration, inorganic nanoparticles (QDs or lanthanide doped nanoparticles) show great advantage here—surface shells can be easily formed, which can efficiently protect the NPs and enhance their brightness.<sup>36,38–42</sup> Nevertheless, neither materials themselves nor NIR emissive labels are within the scope of the current review, and readers interested in this topic can use the above-mentioned references as a starting point for more in-depth discussion.

The developments of a novel luminescent thermometer should be concomitantly supported by proper physical models that not only are capable to allow for the targeted design of sensitive nanothermometers, but also to account for robustness, accuracy, and highest possible precision. The models should be capable to (i) replace current try-and-error or incremental approaches to finding new optical thermometers with educated guesses for new materials, (ii) understand the limits of a particular physical phenomenon, and (iii) assure sample-to-sample variation-free operation. For example, based on Boltzmann thermometers, not only sensitivity values and temperature range limits may be wisely optimized and enhanced, but also enable to construct primary thermometers to counteract known issues of thermometer recalibration *in situ*.<sup>43</sup>

Given the novelty of many thermometric reporters, some adjustments on recording and detection methods need to be proposed to assure reliable, reproducible, and accurate temperature determination and mapping. These technical issues and their impact on the metrology, however, are rarely discussed. This lack of consideration, in turn, has motivated us to review the current knowledge and achievements in the optical 2D thermometry *in vitro* and *in vivo*. Although some examples of temperature mapping exist in technology (e.g., temperature distribution in flame,<sup>44</sup> hot spots in microprocessors,<sup>45</sup> or rotating mechanical elements<sup>46</sup>), we think that the fact that T mapping *in vitro* is not well developed and widely used originates from a few, well defined reasons:

- (1) lack of sufficiently good LT probes, which are not only temperature sensitive, but can be adopted as biological reporters—i.e., assure individual nanoparticles with no aggregate formation, whose surface can be bio-functionalized for specific targeting, long circulation time, and nontoxicity;
- (2) difficulties in implementation of LT mapping, which come from the unreliability of T determination, owing to the susceptibility of the existing LT agents to numerous experimental factors, such as excitation intensity, the penetration depth of excitation and emission light, and technical complexity of measurement (e.g., spectral overlap, the brightness of LT, etc.); and
- (3) difficulties in the implementation of LT sensing with the technology available at the moment, i.e., most of the T sensitive phosphors are evaluated with high resolution and super-sensitive spectrometers or photodetectors, which hinder adoption of good T probes (satisfying conditions 1 and 2) for simple, practical, and widely accessible microscopic imaging studies.

Every new technological solution (here luminescence based thermometry and thermal imaging) follows a typical trend described in Fig. 1, which is called technology adoption curve.<sup>47</sup> In our opinion, current status of temperature imaging has entered the realism phase, where materials science achievements and various luminescent temperature probes are confronted with the demands of real-life applications and many materials fail to pass the disillusionment chasm. This is because, even though they fulfill fundamental requirements related to temperature responsiveness and sufficient sensitivity, they lack numerous other features, which are necessary to safely use these temperature reporters in 2D imaging *in vivo/in vitro*.<sup>21,48</sup> This requires setting a standardization rules to be satisfied, which should evaluate not only the temperature sensitivity factor, but also other ones, such as (i) true-ness, resolution, reproducibility of T determination (in terms of metrology) as well as (ii) susceptibility of the temperature reporters to the local environment (in terms of chemical and spectral susceptibility of the readout to surrounding tissue), (iii) brightness and (iv) spectral operation range (in terms of inherent properties of the LTs) as they also should be suitable to reliably map temperature with existing readout mechanisms and methodologies. We are convinced, it is impossible to further progress in this field, without joint work of material scientists (majorly responsible for the progress in nanothermometry field so far) with physicists, biologists, and engineers. Only then, and taking into account all aspects briefly enumerated above, we may expect transition from the *optimistic expectations* toward *mature technology* ready to be used in medical diagnosis and technology.<sup>21</sup>

After a few years of initial luminescence spectra based thermometry field development (reviewed by Vetrone and Jaque,<sup>49</sup> Carlos *et al.*,<sup>50,51</sup> Dramićanin<sup>52</sup> and others<sup>23,46,53</sup>), the catalogue of methods suitable for temperature determination can be further expanded to the more actual and complete one. Currently, at least eight methods have been known or proposed which quantify (a) temperature dependent absolute intensity, (b) shift of emission band, (c) shift of absorption edge, (d) relative emission bands intensities under single excitation, (e) relative single emission band intensity under two different excitation wavelength, (f) luminescence decays, (g) spectral anisotropy and eventually (g) emission bandwidth (Table I and Fig. 2). Each of these techniques quantifies the thermometric parameter ( $\Theta$ ) in a different way and traditionally, materials scientists who develop new thermometric

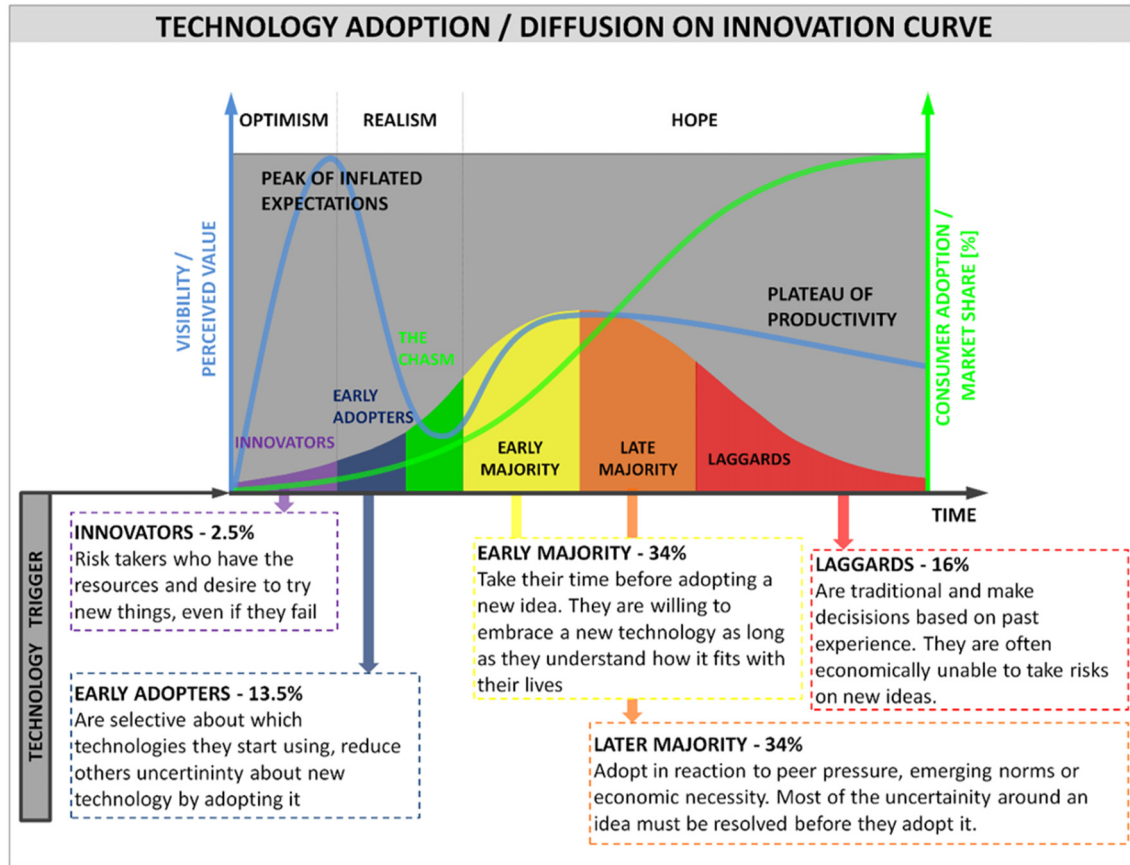
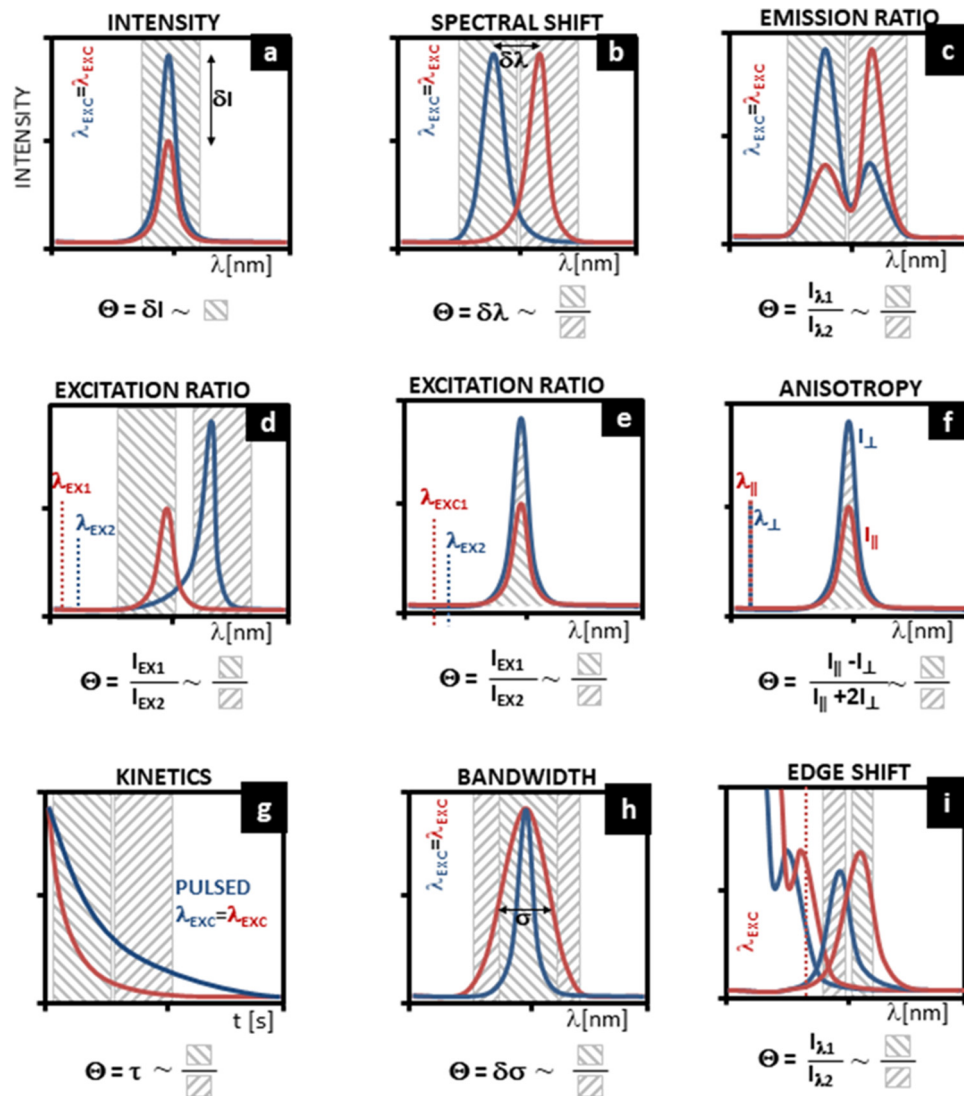


FIG. 1. Technology adoption curve.

**TABLE I.** The comparison of T determination methods ( $\Theta$ —thermometric parameter, F/C/S/Q—feasibility to implement/cost to implement/speed of readout/quality of readout (e.g., expected sensitivity, reliability of quantitative reading), ■/■/■/■—prohibitive/poor/medium/good/outstanding for routine and reliable measurements, the ■ means there are no examples, thus this particular method is of hypothetical importance).  $I(\Delta\lambda)$ —denote intensity I in the given ( $\Delta\lambda$ ) spectral band. The “ $\Theta$  definition” defines precisely the thermometric parameter, while “ $\Theta$  imaging,” simplifies the  $\Theta$  determination of luminescence image detectors.

Type of thermal induced change	Photo-excitation type	$\Theta$ definition	$\Theta$ imaging	F/C/S/Q
A Relative intensity of luminescence	$1\lambda \rightarrow 1\lambda$	$\delta I(\lambda)$	$\delta I(\Delta\lambda)$	■/■/■/■
B Shift of emission band	$1\lambda \rightarrow 1\lambda$	$\Delta\lambda$	$I(\Delta\lambda_1) / I(\Delta\lambda_2)$	■/■/■/■
C Relative emission bands intensities under single excitation	$1\lambda \rightarrow 2\lambda$	$I(\lambda_{EX1}, \lambda_{EM1}) / I(\lambda_{EX1}, \lambda_{EM2})$	$I(\Delta\lambda_1) / I(\Delta\lambda_2)$	■/■/■/■
D Relative emission bands intensities under double excitation	$2\lambda \rightarrow 2\lambda$	$I(\lambda_{EX1}, \lambda_{EM1}) / I(\lambda_{EX1}, \lambda_{EM2})$	$I(\Delta\lambda_1) / I(\Delta\lambda_2)$	■/■/■/■
E Relative emission intensity under two excitation bands	$2\lambda \rightarrow 1\lambda$	$I(\lambda_{EX1}, \lambda_{EM1}) / I(\lambda_{EX1}, \lambda_{EM1})$	$I(\Delta\lambda_1) / I(\Delta\lambda_2)$	■/■/■/■
F Spectral anisotropy	$2\lambda \rightarrow 2\lambda$			■/■/■/■
G Luminescence decays	$1\lambda \rightarrow 1\lambda$	$\tau$	$\tau$ —scanning $I(\Delta\lambda, \Delta_1, \Gamma_1) / I(\Delta\lambda, \Delta_2, \Gamma_2)$	■/■/■/■
H Emission bandwidth	$1\lambda \rightarrow 1\lambda$	$\Delta FWHM$	$I(\Delta\lambda_1) / I(\Delta\lambda_1)$	■/■/■/■
I Shift of absorption edge	$2\lambda \rightarrow 2\lambda$	$\Delta\lambda$	$I(\Delta\lambda_1) / I(\Delta\lambda_2)$	■/■/■/■



**FIG. 2.** Schematic illustration of the temperature dependent mechanisms. Blue and red colors symbolize the luminescent features at low and high temperature, respectively. The gray diagonal filled rectangles indicate, e.g., spectral [(a)–(g) and (i)] or temporal (h) windows seen by the camera. Even though there are no examples of (h) and (i) methods, they may potentially be suitable for T imaging in the future.

reporters rely on the scientific grade (highly time and spectrally resolved) spectroscopes and rarely discuss how feasible is to make a transition to detectors, which are more cost-effective and more suited for T imaging. Therefore, our motivation here is to try to determine how easy and reliably can the temperature be visualized in *in vitro* or *in vivo* conditions. Starting from these considerations on the technical feasibility to map temperature, we derive favorable properties and necessary conditions to be met by LTs. We also evaluate these technical aspects from the perspective of quality of results, robustness and cost effectiveness of imagers. Finally, we present examples of existing literature reports on *in vitro* and *in vivo* temperature imaging. The success of optical thermometry requires cooperation between many interdisciplinary fields, and try-and-error approach in searching of the most

suitable thermometers must be proceeded with defining clear requirements for materials and quantification methods,<sup>21,23</sup> understanding the physical phenomena behind thermal sensitivity<sup>21,43,54</sup> and adjusting all these issues to the available and reliable detection instrumentation (discussed here). Especially, the understanding and modeling of optical thermometers is underrepresented in scientific literature, while they are key to knowingly optimize the performance of luminescent compounds. A comprehensive and complementary study discussing the physical mechanism responsible for temperature-induced change in physical parameters was presented recently by Suta and Meijerink<sup>43</sup> and the necessary information regarding a theoretical background and physical and thermodynamic limitations of the physical models can be found there.

We believe that the current review offers an alternative perspective drawing the attention of material scientists to established problems and help them find more targeted solutions in future. We also emphasize, that further progress in the field of luminescence thermometry requires deeper understanding of physical mechanisms and materials factors known to be temperature dependent, and simultaneously increased awareness of methodologies and technical aspects of T readout.

## II. METHODOLOGIES AND TECHNICAL ASPECTS OF T READOUT

There are many scientific papers showing new materials as potential candidates for remote thermometry. Unfortunately, these examples are mostly focused on the single spot detection and the calibration or readout of such LTs usually requires high resolution excitation/emission spectra and rather sophisticated and costly spectrometer setups. However, as this technology has the ambition to be used in real *in vitro/in vivo* studies, the readout technology has to be rapid, simple, cost-effective and compatible with current imaging detectors, which put some additional technical requirements. Therefore, the major motivation for this article, was to overview existing examples of temperature imaging, from the perspective of technology required to achieve this goal. Table I and Fig. 2 compare how different physical observations ( $\Theta$  definition) can be quantified, using a simple available camera ( $\Theta$  imaging). For example, the shift of the maximum of emission band in response to temperature change, requires a spectrograph with a spectra resolution of  $d\lambda < 1$  nm. However, such a solution is usually too complex, too slow, and ineffective for imaging in raster scanning mode. Moreover, the speed of imaging is directly related to the brightness of the T probes. In opposite to the spectrograph, a CCD camera can be used to quantify emission intensity simultaneously for multiple spots on the sample in two spectral windows, which shall assure fast and simultaneous readout. Nevertheless, such ratiometric imaging is highly susceptible to artifacts, spectral overlap between T probes, and sample spectral properties. This one and the other possibilities are discussed in Sec. IV from the perspective of technical feasibility to adopt a given mechanism for 2D temperature mapping.

In particular, Table I defines the thermometric parameter in two different ways, the one ( $\Theta$  definition) seen by materials scientists and the other one ( $\Theta$  imaging) from engineers perspective. While the former one is equipped with highly (temporally or spectrally) resolved fluorescence spectrometers, the latter possess a sensitive CCD/CMOS camera, which is capable of measuring 2D intensity images in continuous wave or time resolved mode, possibly in spectral domain as well. The former offers high resolution, which, however, is typically inconvenient for imaging because of the speed of T mapping. The latter solution has technical issues with spectral resolution, but highly parallel detection offers technically simple solution for 2D mapping of spectral signatures. As presented in Fig. 2, CCD/CMOS cameras support all the types of spectral features, which are considered to be the indicators of temperature. Apart from the obvious ones, such as absolute intensity or emission intensity ratio, also spectral shift, luminescence anisotropy, kinetics, and emission bandwidth can be easily quantified by quantifying 2D spectral images. However, it requires using additional spectral filtering, low background, no autofluorescence of the sample, specific excitation wavelength, or time gated detection. Each of these methods will be discussed below in Sec. IV, and whenever

possible, will be supported with the existing scientific literature on experimental demonstrations *in vivo*, *ex vivo*, *in vitro*, or on phantoms.

## III. INFLUENCE OF TISSUE/SAMPLE SPECTROSCOPY ON THE TEMPERATURE READOUT

So far, not too many reports discussed the robustness of the temperature readout *in vivo* or *in vitro*, while serious experimental issues limit the reliability of such sensors. This originates from the fact, that the luminescence of LT may be affected by the sample spectroscopy itself, which is especially troublesome *in vivo* or *ex vivo*. The LTs are typically calibrated under spectrally “sterile” conditions, i.e., there is no autofluorescence of the sample taken into account as well as low background signal and non-existent or limited scattering are assumed, while the measurements carried out *in vivo* and *in vitro*, must consider the sample properties as well. This is clearly illustrated in Fig. 3, where absorption spectra of the tissue components are shown against the temperature dependent spectral features of different luminescent thermometers at high and low temperatures. The tissue spectroscopy may modify, e.g., the ratio of emission bands or the shape of the emission band, which is even more complicated, because tissue spectroscopy undergoes local (e.g., from site-to-site) and transient (over time) variations. Pulses of oxygenated blood, which spectrally overlap with, e.g., most well-known  $\text{Yb}^{3+}/\text{Er}^{3+}$  co-doped nanothermometers are good examples of this. Another issues come from the fact, that the tissues may significantly differ in composition (water/fat content, pigmentation, thickness, heterogeneity, blood vessels density, etc.), which complicates calibration and reliable temperature readout. These issues are discussed in more detail elsewhere,<sup>55,56</sup> but they definitely require attention and careful consideration in practical implementations of luminescence based thermometry.

It is very important to mention, the spectral characteristics of the tissue or sample, may significantly affect the temperature being read from the thermometric parameter.<sup>21,22,48</sup> In a real application, the conditions for T readout are much more complex than under laboratory conditions. For this reason, from the metrological perspective, the sensitivity of the temperature readout must not be the only important factor characterizing luminescent thermometers.<sup>48</sup> No less important are temperature readout accuracy (proximity of individual measurement to true temperature value  $T_0$ ), trueness (closeness of mean from a set of temperature measurements to true temperature value  $T_0$ ), precision (reproducibility of temperature readout  $\Delta T$  among a set of readout temperatures), and measurement resolution (smallest change in temperature that produces measurable change in thermometric parameter  $\Theta$ ).<sup>21</sup> The high resolution stems from high brightness, while high sensitivity requires a high signal to noise/background ratio, to determine the smallest  $\delta\Delta$  reliably. Since the calibration is usually performed under conditions other than the actual *in vivo* environments, and the biologically acceptable temperature variation range is limited to 0–50 °C, it is of utmost importance to examine these parameters carefully, which has been omitted so far either in materials science research or in the view of possible applications of luminescent thermometers in hyperthermia treatment. Assuming Gaussian distribution of temperature readout  $T(\Theta) \sim \exp(-(\Theta - \mu)^2/2\sigma^2)$ , the mentioned trueness, precision, and resolution of the measurement, may be therefore defined as the mean temperature of readout [ $\mu(T)$ ], variance [ $\sigma(T)^2$ ], and standard deviation [ $2\sigma(T)$ ], respectively. The temperature

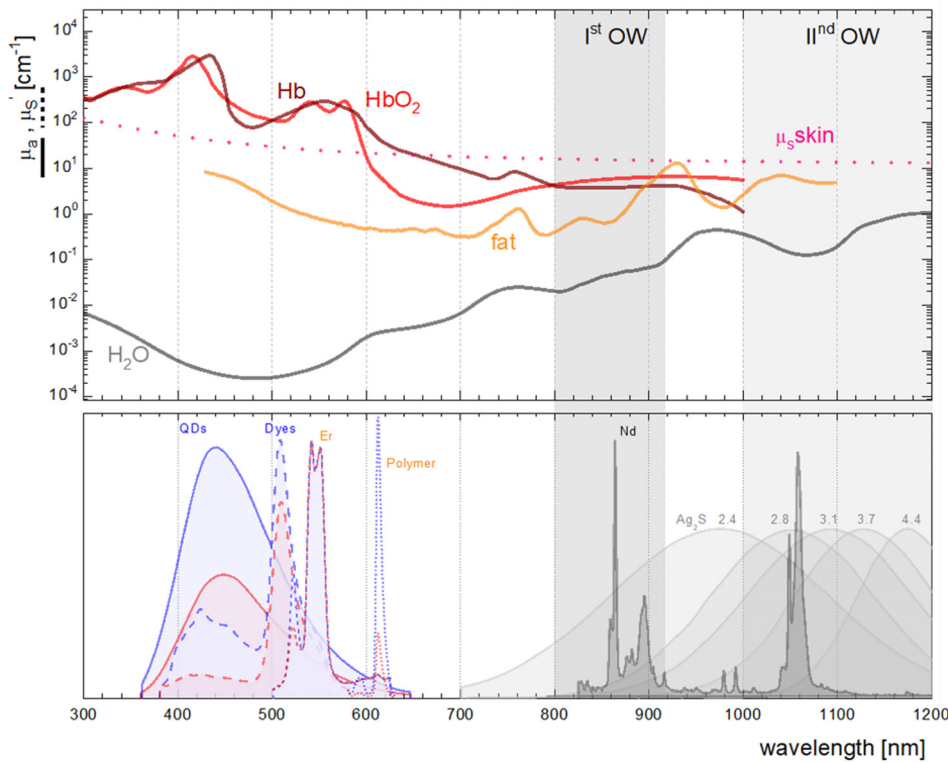


FIG. 3. Spectral properties of tissue and its main components (a) and of the most frequently used optical luminescent nanothermometers (NT) (b).

resolution is sometimes calculated as  $\delta T(T) = \delta \Theta / [S_R(T) \cdot \Theta(T)]$ , which actually is the theoretically expected statistical temperature uncertainty. It does not take into account any systematic errors that can additionally falsify the temperature measurement as discussed above and in numerous excellent research papers.<sup>43</sup> One should be aware, that there is currently no method to incorporate the material and experimental parameters (e.g., size, composition, dopant type and concentration, etc.) into universal thermometer characterization, other than to estimate  $\Theta(T)$ ,  $S_R(T)$  parameters from the experimental dataset. Although deep understanding of physical phenomena and modeling may support intentional designing of NT reporters, such studies are rare.<sup>43,54,57–60</sup> Additionally, the dependence of  $\Theta(T)$  from photoexcitation intensity, shown by some LT reporters (e.g., upconverting materials) practically disqualifies such LT materials from *in vivo* applications as one cannot actually determine excitation intensity in heterogeneous objects with sufficient accuracy. Fortunately, understanding the mechanism behind thermal responsiveness, shall let define the primary thermometers, which in some, but not all cases, should make the T measurements independent from environmental and some of the measurement factors.

To better understand the role of biological tissues when considering the temperature readout, one needs to take into account, that many physical processes that take place during the measurement. First, from a thermodynamic standpoint, a living tissue is considered to be a complex system whose temperature is determined by the interplay between its intrinsic properties (such as its mass, specific heat, and thermal conductivity), the physiological parameters of the organism (such as blood temperature, perfusion rate, and metabolic

activity), tissue conditions (such as water or fat content) and the environment conditions (mainly ambient temperature). All these variables influence the response of living tissues to thermal stimuli, which can be expressed through the well-known Pennes' bioheat equation and the corresponding boundary conditions. In such formalism, this can be written as<sup>61</sup>

$$\rho_t c_t \frac{dT_s(\vec{r}, t)}{dt} = k \nabla^2 T_s(\vec{r}, t) - \omega_b \rho_b c_b (T_s(\vec{r}, t) - T_b(\vec{r})) + Q_{met}, \quad (1)$$

where  $\rho_b$ ,  $k$ , and  $c_t$  are the mass density, thermal conductivity, and specific heat of the living tissue and  $\omega_b$ ,  $\rho_b$ ,  $c_b$ , and  $T_b$  are the perfusion rate, mass density, specific heat, and temperature of the blood. In the expression above,  $Q_{met}$  refers to the heat production caused by metabolic activity. Pennes' bioheat equation not only establishes the relation between tissue conditions and activity and tissue temperature. It also determines the spatial spread-out of temperature within tissues. For instance, it establishes that even when dealing with well-localized heat sources, the temperature changes caused in tissues can expand significantly in the three dimensional space. From a technological point of view, this could be understood as good news, because it means that we do not need superhigh spatial optical resolutions in our thermal images (for sure, at the *in vivo* level, we do not need to reach nanometric resolution).

Spatial diffusion of heat in tissues constitutes an additional difficulty when interpreting the thermal images. For instance, during thermal therapies, and advanced analysis of the thermal images of tumors will be required to determine the location of heating source and, also,

to achieve an accurate estimation of the thermal dose.<sup>62</sup> But from a positive point of view, if heat diffusion within tissues is well-known and modeled, the acquisition of multiple thermal images under different conditions (e.g., spatial scanning of heat source within tissues, acquisition of multiple and projections of thermal patterns) can be the first step toward the development of thermal tomography. This, of course, would imply a significant effort in the development of algorithms for the analysis of 2D/3D thermal images.

From the standpoint of light propagation into the tissue, on the other hand, the tissue is typically considered as a simple scattering medium in which the path of a photon is considered to be probabilistic in nature. Under this simple assumption, the main impact of the tissue on the thermal images (obtained from the analysis of fluorescence images) is losing spatial optical resolution. Even in an ideal situation, where all the photons are generated from a well-defined location, tissue-induced light scattering causes a relevant spread out of photons at the imaging plane and thus resolution loss. In principle, if the photon path within the tissue is known, it becomes possible to determine the location from which it has been emitted within the tissue from the fluorescence image. This, in turn, implies that if the photon trajectory is known, it would be possible to increase the resolution of the thermal image and, even, to localize in three dimensions the luminescence and heat source. To determine the photon trajectory through the tissue, the Monte Carlo (MC) method is generally applied.<sup>63</sup> It deals with experiments on random numbers and is applied to situations where a thorough analytical description is either lacking or too unmanageable to yield a solution. Since the scattering of individual photons is governed by the laws of quantum mechanics, this method naturally gained popularity for the description of light propagation in biological tissues. The underlying assumption in MC is that one is dealing with a sequence of random non-correlated events.<sup>64,65</sup> This would imply that the probability of a photon changing from a state to another is independent of its previous states. In other words, it has no knowledge of its own history.

A combination of both the MC method and Penne's formalism could, therefore, result in a very powerful tool for the description of the effect played by tissues in temperature readout provided by luminescent probes. Combining MC and Pennés formalisms is however not an easy task at all. The key point is that MC simulations are based on the optical properties of tissues and these depend on tissue temperature that, in turns is given by Pennés equation.<sup>66</sup> The situation becomes even more complicated with the appearance into scene of recent studies that demonstrate how at certain spectral ranges (typically used by infrared luminescent nanothermometers in the *in vivo* applications) the tissue absorption can be a dominant factor affecting the photon propagation within tissues.<sup>67</sup> Note that the tissue absorption at specific wavelengths is not considered in MC simulations. In addition, the presence of relevant tissue absorption of emitted photons also complicates the solution of Pennés's equation as it introduces an additional source of heat that will spread out all along the photon trajectory. So, both MC and Penne's formalism should be modified to include photon absorption and its impact on their trajectories and on the temperature distribution within the tissue. The adaptation of both formalisms to consider the effect of photon absorption becomes also mandatory to reconstruct the emission spectra of nanothermometers caused by tissue absorptions. Tissue induced spectral distortions make it very difficult to reach a reliable thermal readout at the *in vivo* level.<sup>68</sup> The development of algorithms, considering tissue scattering and absorption, capable of

removing these tissue-induced distortions will make possible to achieve reliable thermal reading from a simple analysis of the emission spectra collected at the *in vivo* level. In summary, challenges of luminescence-based thermo imaging do not reside only at the experimental side, but a great effort in modeling and image reconstruction techniques that consider NT materials and the same factors (Table II) will be required in short time to achieve high resolution and reliable thermal images

#### IV. TEMPERATURE DETECTION READOUT

In general, the thermometric parameter  $\Theta(T)$  is measured vs variable temperature  $T$  during the calibration procedure, which means the experimental relationship between  $\Theta(T)$  and  $T$  is recorded

$$\Theta(T) = f(T). \quad (2)$$

It is desirable to understand the mechanism behind these phenomena in order to relate these parameters in the form of an (often unknown) analytical mathematical equation  $f(T)$ . For example, assuming the temperature phenomenon as a simple Boltzmann relationship between the population of two emitting levels  $n_1$  and  $n_2$ , the thermometric parameter may be described by a simple formula<sup>69</sup>

$$\Theta(T) = \frac{I_2}{I_1} \sim \frac{n_2}{n_1} = B \cdot e^{-\frac{AE}{k_B T}}. \quad (3)$$

In the limit of zero pump power in a given temperature, the temperature  $T_0$  corresponds to no laser-induced heating and the thermometric parameter  $\Theta_0(T)$  can be calculated as

$$\Theta(T_0) = B \cdot e^{-\frac{AE}{k_B T_0}}. \quad (4)$$

Making a simple ratio of  $\Theta(T)/\Theta_0(T)$ , one gets

$$\frac{\Theta(T)}{\Theta_0(T)} = e^{-\frac{AE}{k_B} \left( \frac{1}{T} - \frac{1}{T_0} \right)}. \quad (5)$$

By making the natural logarithm of both sides of the equation, one gets

$$\frac{1}{T} = \frac{1}{T_0} - \frac{k_B}{\Delta E} \ln \left( \frac{\Theta}{\Theta_0} \right). \quad (6)$$

Therefore, the inverse function can be defined as

$$T = f^{-1}(\Theta) = \left[ \frac{1}{T_0} - \frac{k_B}{\Delta E} \ln \left( \frac{\Theta}{\Theta_0} \right) \right]^{-1}, \quad (7)$$

which enables, based on the actual  $\Theta$  value, to read the actual temperature independently from factors, which are embedded in parameter B in Eq. (4). The same  $T_0$ ,  $\Delta E$ , and  $\Theta_0$  coefficients can be used for imaging as well, where  $T(x, y)$  is obtained for every (x,y) point in the sample. If the mathematical formula describing the  $\Theta(T) \sim T$  relation is unknown, the  $\Theta = f(T)$  relationship can be fitted with a spline function or a polynomial, but "primary" features and advantages become lost. This means that the material parameters embedded in the B parameter of Eq. (3) cannot be neglected and thus the calibration of the  $\Theta = f(T)$  relationship performed under the given experimental and environmental conditions is not valid under the other conditions. For example, the readouts  $T = f^{-1}(\Theta)$  calibrated in water colloid, will not be valid under PBS or air conditions, while keeping the 'preliminary' features, enables to get the same absolute temperature independently from external conditions like PBS, water, air, etc.



**TABLE II.** Materials, experimental, and sample factors, which affect the performance and reliability of temperature readout with luminescent thermometers.  $\mathbf{Q}_S$ —quenching at the surface by ligands, defects, solvent;  $\mathbf{Q}_{NR}$ —quenching by non-radiative processes;  $\mathbf{QY}$ —emission quantum yield;  $\alpha$ —extinction coefficient;  $\mathbf{S}/V$ —the ratio of a number of surface to volume activators;  $\mathbf{M}(T)$ —mechanism of thermal sensitivity;  $\mathbf{B}$ —brightness;  $\mathbf{ET}$ —energy transfer processes, such as ETU, CR,  $\mathbf{Q}_{NR}$ ;  $\mathbf{h\nu}_{MAX}$ —maximum phonon frequency;  $\Delta E$ —energy gap between thermally coupled states;  $\Theta(T)$ —thermoreponsive parameter (e.g., LIR,  $\tau$ ,  $\delta\lambda$ );  $\mathbf{S}_R = \mathbf{S}_R(T)$ —relative sensitivity;  $\Delta T_{MIN}$ —temperature resolution;  $|T-T_0|$ —accuracy of temperature determination in respect to the actual temperature of the sample ( $T_0$ );  $\mathbf{J}_S$ —spectral self-overlap integral between LT absorption and emission;  $\mathbf{J}_E$ —spectral overlap integral between LT emission and sample absorption;  $\Delta\lambda_{STOKES}$ —Stokes shift between excitation and emission;  $\Delta\lambda_{LIR}$ —Stokes shift between wavelengths used for  $\Theta = \text{LIR}$  determination;  $\mathbf{S}/\mathbf{B}$ —a signal to background ratio;  $\mathbf{S}/\mathbf{N}$ —a signal to noise ratio.

		Affected process/quantity	Directly affected thermometer properties	Guiding rules
<i>Materials factors</i>		<i>Details</i>		
NP size and size distribution	Homogeneity of response	$S/V, QY, Q_S, \alpha$	$\Theta, S_R, \Delta T_{MIN},  T-T_0 $	<ul style="list-style-type: none"> <li>• <math>\Theta</math> and <math>S_R</math> measured experimentally</li> <li>• Primary thermometers</li> <li>• No <math>\Theta/S_R</math> excitation power dependence</li> </ul>
NP composition	Type of S/A	$\lambda_{EXC}, \lambda_{EMI}, M(T), J_S$	$\Theta, S_R$	
NP surface chemistry	Type of ligands/solvents	$QY, Q_S, \alpha_{LIG}$	$\Theta, S_R$	
NP architecture	Core(C) vs core/shell (C-S), C-S composition, number of S layers	$\lambda_{EXC}, B, ET$	$\Theta, S_R$	
Concentration of dopants (S, A, and D)	[S], [A] or other dopants [D]	$\alpha, ET$	$\Theta, S_R$	
Host	Crystalline host	$h\nu_{MAX}$	$\Theta, S_R$	
Energy gap between thermally coupled states	$\Delta E$ (cm <sup>-1</sup> )	$M(T)$	$\Theta, S_R$	
<i>Experimental factors</i>				
Temperature	Local temperature T (K)	ET	$\Theta, S_R, \Delta T_{MIN},  T-T_0 $	<ul style="list-style-type: none"> <li>• High spectral sensitivity of detector</li> <li>• Low spectral bleeding</li> </ul>
Excitation intensity density	$I_{EXC}$ (mW/cm <sup>2</sup> )	ET, QY, $\alpha, B, S/N$	$\Theta, S_R$	
Excitation mode (CW vs pulsed)	CW vs $f_{PWM}$ (Hz)	ET, QY, B, S/N	$\Theta, S_R$	
Spectral bleeding of channels		S/B	$\Theta, S_R$	<ul style="list-style-type: none"> <li>• <math>I_{EXC} \leq \text{MPE}</math></li> </ul>
Spectral sensitivity of the detector	$S(\lambda_{EMI_i})$	S/N	$\Theta, S_R, \Delta T_{MIN}$	
<i>Sample factors</i>				
Spectral properties of the sample	$\mu_S, \mu_A', g = \text{fun}(\text{time}, \lambda_{EXC}, \lambda_{EMI})$	$I_{EXC}, J_E, S/N, S/B$	$\Theta, S_R, \Delta T_{MIN},  T-T_0 $	<ul style="list-style-type: none"> <li>• Low Stokes shift <math>\Delta\lambda_{STOKES}</math></li> <li>• Low LIR shift <math>\Delta\lambda_{LIR}</math></li> <li>• Self-normalization of <math>\Theta</math></li> <li>• <math>\lambda_{EXC}, \lambda_{EMI} \in \langle \text{BW I, II, III} \rangle</math></li> </ul>
Homogeneity of the sample	$\mu_S, \mu_A', g = \text{fun}(x, y, z)$	$I_{EXC}, J_E, S/N, S/B$	$\Theta, S_R, \Delta T_{MIN},  T-T_0 $	
Concentration and homogeneity of LTM distribution	[NPs] = fun(x, y, z)	B, S/N, S/B	$\Delta T_{MIN},  T-T_0 $	

The Boltzmann population of higher energy levels is a simple explanation described by a simple equation. Unfortunately, not always the phenomena behind thermal sensitivity are easy to decipher, or there are two or more physical phenomena overlapping in different proportions in different temperature ranges. If the  $\Theta(T) = f(T)$  is smooth, it can be described, within the temperature operating range, by a polynomial, which, through appropriate series reversion,<sup>70</sup> allows to analytically find the inverse function  $\Theta = f^{-1}(T)$ . This concept relies on the mathematical foundation that every power series uniquely converges to a function it represents. Although mathematically correct or acceptable, from metrology perspective, it is much more important to understand the physical phenomenon behind temperature susceptibility, which enables to find the constraints of the proposed materials and methods and knowingly optimize such thermometers for targeted applications. Moreover, the lack of appropriate model hinders actual interpretation of thermometers behavior, determination of its operating range and its reproducibility may not be guaranteed.

### A. Absolute intensity of luminescence

The great advantage of temperature mapping by detecting the absolute intensity of luminescence changes  $\Theta = \delta I(\Delta\lambda)$  [Fig. 2(a)] is its technically simple implementation and fast readout [Table I(a)]. Moreover, most luminescent species may serve as temperature probes in this working mode. Unfortunately, this technique is suitable only for a rough estimation of temperature rise or fall. It is not very reliable, since the absolute intensity depends on the concentration of NPs per volume, penetration depth of photoexcitation intensity, and scattering and absorption properties of the biological sample and is difficult to implement in 3D tomography volumetric imaging. This approach has already been used for *in vitro* and *in vivo* temperature mapping (Fig. 4).

The thermometric parameter in this relative intensity technique (AIT) can be generally defined as

$$\Theta(T) \sim dI(\lambda_{exc}). \tag{8}$$

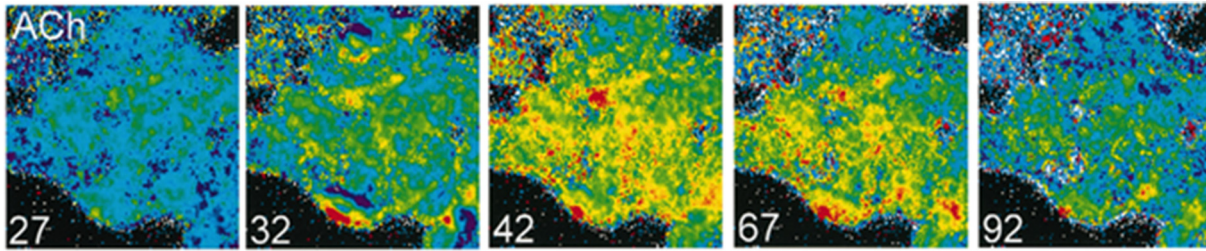


**FIG. 4.** Imaging acetylcholine chemical stimulation and heat wave propagation. Pseudo-color images (color-coded from blue through green and yellow to red for areas from lower to higher temperatures) after acetylcholine application in a cluster of cells. Numbers on the images are the frame numbers, frame interval was about 1 s. Acetylcholine puff was given in frame 27.<sup>71</sup> Reproduced with permission from Zohar *et al.*, *Biophys. J.* **74**, 82–89 (1998). Copyright 1998 Elsevier.

If the relative sensitivity changeover the studied temperature range is constant, e.g.,  $S_R = 0.5\%/^{\circ}\text{C}$ , knowing the initial temperature  $T_0(x, y)$  distribution and assuming homogenous excitation illumination and nonmoving objects, one may determine spatial temperature maps as

$$T(x, y) = T_0(x, y) + f^{-1}\left(\frac{I(x, y) - I_0(x, y)}{S_R(T)}\right), \quad (9)$$

where  $f^{-1}$  is the reverse function, which is based on given  $\Theta(T)$  reads corresponding to  $T$ . Because the starting temperature map  $I_0(x, y)$  is actually difficult to know before the experiment (e.g., mitochondria may show natural higher temperature than in the cytoplasm), the relative temperature rise in respect to the starting point can only be found in response to some stimulus (e.g., drug, toxicant, local heating, etc.). In consequence, relative temperature change can only be quantified

$$\delta T(x, y) = f^{-1}\left(\frac{I(x, y) - I_0(x, y)}{S_R(T)}\right). \quad (10)$$

One of the first demonstrations on thermal imaging of cells using relative changes in emission intensity was presented by Zohar *et al.*<sup>71</sup> in 1998, who visualized Chinese hamster ovary (CHO) cell clusters during chemical stimulation causing an increase in heat production. The measurement was based on the temperature-dependent luminescence of europium (III) thenoyltri-fluoro-acetonate (Eu-TTA), which exhibited a narrow emission line around 614 nm. With the increasing temperature, the coupling of the energy levels with the environment through molecular vibrations was increasing, and the rate of non-radiative processes was increasing as well, which led to the quenching of Eu-TTA emission. This sensor could not penetrate inside the cells, but was integrated into the liposomal membranes because of its hydrophobic nature. Unfortunately, the sensor showed photobleaching, which was approximated by the exponential decay and omitted in the processing of the data for thermal imaging. In addition, Eu-TTA emission was also dependent on pH changes (range 5–8). Thermal imaging (Fig. 4) was carried out for acetylcholine chemical stimulation and a heat wave was observed in the cells. After the initial phase of acetylcholine dilution, the emission intensity of Eu-TTA was significantly reduced, which was equivalent to the increase in temperature. After some more time, the temperature returned to its original value. Additional control experiments (using a pH-sensitive dye and a pH electrode) evidenced that the addition of the acetylcholine did not change the pH that the sensors are known to be susceptible to.

Another work describing both intracellular temperature and imaging living cells was presented by Gota *et al.*<sup>72</sup> in 2009. The authors

described a fluorescent nanogel thermometer consisting of the polyNIPAM thermosensitive polymer and DBD-AA fluorophore, whose luminescence is easily quenched by water molecules. The gelation was performed by emulsion polymerization using a cross-linking agent (MBAM). Precipitation in the intracellular environment was avoided due to the fact that a highly hydrophilic layer formed by sulfate groups (which was used in excess) was formed on the sensor. PolyNIPAM was changing its conformation depending on the temperature, i.e., at low temperature, it allowed water molecules to get inside and quench the luminescence of the DBD-AA dye, while at higher temperatures, water was pushed out of its interior recovering the luminescence of the dye. In addition, the thermal dependence of luminescence was neither susceptible to changes in pH (range 4–10) nor by the presence of proteins. Thermal images of cells at 29 and 35 °C demonstrated a significant relative increase in emission intensity, which is synonymous with the temperature increase in the cells. Slight 0.45 °C temperature rise was also observed in response to chemical stimulation using trifluoromethoxy carbonylcyanide phenylhydrazine (FCCP) reagent, which is a known uncoupler of oxidative phosphorylation in mitochondria.

Another type of the temperature sensor, which relied on the relative change of the intensity of one band as a function of temperature was also described by Ke *et al.*<sup>73</sup> in 2012. The authors used the L-DNA molecular beacon (L-MB), whose temperature induced conformational changes were modulating the distance between the donor and acceptor (quencher) molecule, which, through distance (and indirectly through temperature) FRET energy transfer was changing the luminescence signal from donor molecules. Importantly, the L-MBs were nontoxic to cells because they consisted of nucleic acids. Interestingly, the L-DNA is not a naturally occurring biological DNA form (in contrast to the D-DNA), which made it resistant to enzymatic degradation. What is more, the MBs provided a fast, accurate and sensitive temperature reading. The measurements of the L-MB emission as a function of temperature had shown that the intensity increased in the range of 20–55 °C resulting in temperature resolution  $<0.7^{\circ}\text{C}$ . It had also been shown that very small changes in sensor performance occurred when the ionic strength (150–200 mM) or pH (6.8–7.4) varied. Then, the L-MBs were introduced into HeLa cells by liposome transfection, and the temperature imaging was performed using confocal microscopy (Fig. 5) with excitation with 488 nm diode laser and emission intensity quantified at 505–535 nm.

In the years preceding 2014, Arai *et al.*<sup>74</sup> created a large database—Diversity Oriented Fluorescent Library (DOFL) containing various fluorescent dyes and found endoplasmic reticulum (ER) thermo

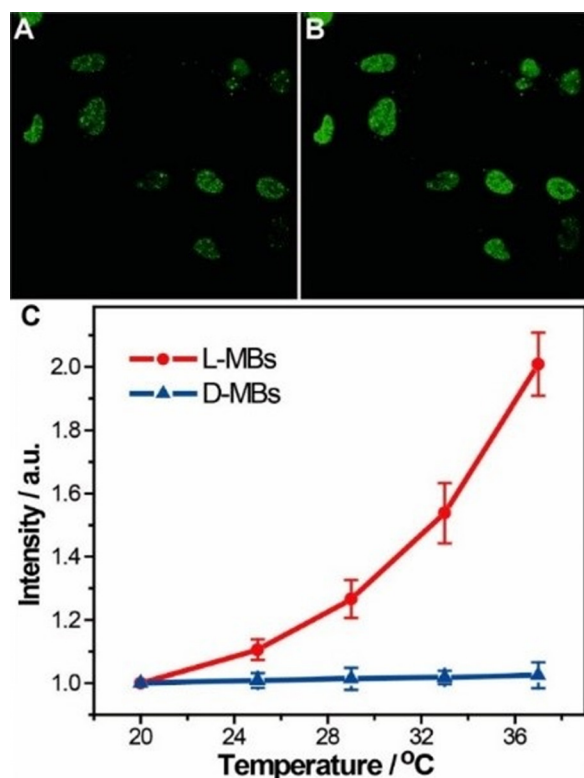


**FIG. 5.** Images from confocal microscopy of transfected HeLa cells at a temperature of (a) 20 °C and (b) 37 °C. (c) Dependence of intensity on temperature for L-MB and for D-MB.<sup>73</sup> Reproduced with permission from Ke *et al.*, *J. Am. Chem. Soc.* **134**, 18908–18911 (2012). Copyright 2012 American Chemical Society.

yellow dye to be suitable for endoplasmic reticulum (ER) targeting. This dye showed the temperature dependent luminescence at 581 nm under 559 nm excitation. The first practical application was shown using an IR laser 1064 nm for spot heating of the cells (by irradiation of the aluminum powders attached to the tip of a glass microneedle). Using a shutter, a “square wave” was obtained as a response to the cycles of local heating and cooling. Moreover, temperature gradients created in this way were visualized in living cells using different laser power (Fig. 6). A linear dependence was obtained for normalized (to its initial value) intensity as a function of temperature change reaching sensitivity of 3.9%/°C (for temperature changes from the initial temperature to 5 °C higher). In the next step, the validation of the received results for live cells was carried out in the fixed cells. In this way, the results were obtained for the cellular environment (which was significantly different from the buffers used in other cases), but with guaranteed accurate temperature control. In addition, the thermometer was found to be insensitive to the presence of  $\text{Ca}^{2+}$  ions and pH changes. Sensitivity also did not depend on the cell line used (HeLa, Chang liver, 3T3, brown adipose tissue and C2C13 myotube). In the case of a long-term measurement, the photobleaching effect could not be omitted and the results were corrected by a single exponential curve. Ultimately, the ER thermo-yellow was used to visualize the heat production caused by the addition of ionomycin (it is a  $\text{Ca}^{2+}$  ionophore). After the addition of the reagent, a decrease in emission intensity of ER thermo yellow was recorded which was equivalent to the temperature increase. The change in intensity of ER thermo yellow during this process was about –6.8%, which corresponded to a temperature elevation of about 1.7 °C. After a thorough analysis, the measurement accuracy for the area with a radius of 1.6  $\mu\text{m}$  was estimated as 0.8 °C.

Arai *et al.*<sup>75</sup> expanded their research with another dye from the designated DOFL database and conducted research on a small fluorescent molecule—Mito-thermo-yellow dye. Those molecules were tested for several heating and cooling cycles in NIH3T3 cells. The dye was incubated beforehand at 37 °C for 15 min, and glass microneedle with aluminum powders attached under 1064 nm laser excitation, was used to create a temperature gradient in a cell on a microscopic scale). The authors

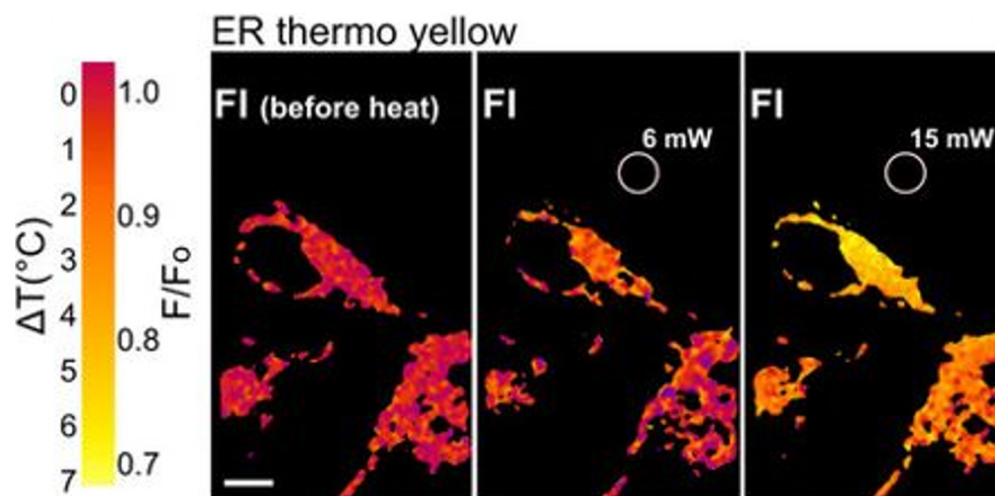


**FIG. 6.** The temperature mapping of ER thermo yellow in live HeLa cells: heating with different laser powers (none, 6 and 15 mW) outside the cells.<sup>74</sup> Reproduced with permission from Arai *et al.*, *Sci. Rep.* **4**, 2 (2014). Copyright 2014 Authors, licensed under a Creative Commons Attribution (CC BY) License.

perceived again a square wave for the point observed at a certain distance from the heating spot for the cyclic switching on and off of the heating laser. Relative intensity was obtained as a function of temperature increase and a sensitivity of  $2.7\%/^{\circ}\text{C}$  was noted, which is much higher than  $1.8\%/^{\circ}\text{C}$  for the Rhodamine B. Moreover the thermal imaging (using 561 nm laser as excitation source) was also carried out and a decrease in emission intensity was visible when switching the heating on. Then measurements were carried out also on other cell lines: 3T3, HeLa, C2C13, Chang, and mESC and a sensitivity of  $2.5\text{--}2.8\%/^{\circ}\text{C}$  was obtained. In contrast, a lower sensitivity of  $2.0\%/^{\circ}\text{C}$  was obtained for brown adipocytes (BA). This has been ascribed to differences in pH, viscosity, the presence of oxygen, etc., which actually limits their use. Moreover, calibration curves were not possible to get, because introducing the Mito-thermo-yellow into the mitochondria requires active transportation and in fixed cells the sensor was leaking out of it. Although some qualitative changes in intensity have been observed for cycling heating and cooling in multi-cellular spheroidal HeLa cells, the previously mentioned drawbacks did not provide sufficiently reproducible quantitative results.

A method based on an absolute intensity of fluorescence has also been involved in thermosensitive copper nanoclusters (CuNCs) spontaneously biosynthesized in cancer cells after injecting and 24 h incubating the copper precursors directly into cells.<sup>76</sup> Such a method proposed in 2017 by Ye *et al.*<sup>76</sup> allowed to obtain inside the MDA-MB-231 cancer cells, the nontoxic, brightly fluorescent, thermosensitive CuNCs with very small sizes of about 2.4 nm. For the same synthesis procedure in normal L02 cells, no fluorescent CuNCs formation was observed. To characterize the obtained sensors, they were extracted from the MDA-MB-231 cells and were subject of the appropriate spectroscopic measurements. Emission spectra measured as a function of the temperature in the range of  $20\text{--}45^{\circ}\text{C}$  revealed the intensity of wavelength stable 610 nm emission band (under 400 nm photoexcitation) to decrease for rising temperature increase. This observation was reproducible in several temperature cycles between  $20$  and  $40^{\circ}\text{C}$  and was explained by the increase in the probability of collisions of molecules, therefore also nonradiative transitions at higher temperatures. The relative sensitivity of the thermal changes was determined as  $3.18\%/^{\circ}\text{C}$ . Then the measurements of the CuNCs inside the MDA-MB-231 cells in which they were biosynthesized were carried out as well. The sensor nanoparticles were formed both in the cytoplasm and in the cell nucleus, however, the stronger emission from the cytoplasm was most likely associated with the enhancement of emission resulting from aggregation in this area (because most CuNCs were created in the cytoplasm), as was similarly observed in the nanoparticles extracted from the cells.

Based on the promising results Kriszt *et al.*<sup>77</sup> in 2018 continued the research on molecules selected from their DOFL database<sup>74,75</sup> in order to determine material highly sensitive to thermal changes. In this case, the ERthermAC thermosensitive dye (based on BODIPY) was described, which was created by modifying the previous ER thermo yellow sensor [that was able to target the endoplasmic reticulum (ER)] to provide greater photostability. Using the organelle tracking ER Tracker green, it was confirmed that ERthermAC was localizing in the ER region in cells. In WT-1 adipocytes cells (cellular uptake during 30 min incubation at  $37^{\circ}\text{C}$ ), a calibration curve was created for normalized intensity as a function of the measurement temperature in the  $18\text{--}43^{\circ}\text{C}$  range. It has been found that as the

temperature was increasing, the intensity of the sensor was decreasing (the same course of the curve was obtained while reducing the temperature). For the  $18.1\text{--}35.0^{\circ}\text{C}$  range a linear decrease in the intensity by  $-1.07\%/^{\circ}\text{C}$  was obtained, while for the range  $35.7\text{--}42.8^{\circ}\text{C}$ , a higher slope of  $4.76\%/^{\circ}\text{C}$  was noted. That work focused on brown adipocytes and demonstrated the heat production inside of them. To that end, isoproterenol (ISO) was added and changes in the intensity of the sensor emission in the cells were imaged. Following the ISO stimulation, most cells showed a reduction in the intensity of ERthermAC or FCCP emission, which corresponded to the increase in temperature. It was also shown that physiological concentrations of  $\text{Ca}^{2+}$  ions ( $10\text{--}1000\ \mu\text{M}$ ) do not affect the ERthermAC activity, while the pH range of  $7.0\text{--}8.1$  changes its intensity to a small extent ( $-8.5\%$ ) compared to thermally activated intensity changes.

The green synthesis process of nitrogen-doped carbon dots (N-CQDs) for applications as a sensor of  $\text{Fe}^{3+}$  ions presence, to check for cysteine presence and temperature changes in cells was described by Lu *et al.*<sup>78</sup> in 2018. The emission of the sensor was tunable and by varying the excitation wavelength from 315 to 455 nm, the emission peak shifted from 424 to 512 nm. The maximum emission corresponding to the wavelength of 439 nm was excited at 355 nm. In an aqueous solution, it was shown that after the addition of  $\text{Fe}^{3+}$  ions that act as an effective quencher, the emission intensity of the N-CQDs decreased gradually. The N-CQDs were then used to visualize HepG2 cells (introduction by incubation for 4 h at  $37^{\circ}\text{C}$ ) exploiting a confocal laser scanner, and their low cytotoxicity was demonstrated. Emission stability was shown by scanning for 10 min without a visible change in the intensity. Furthermore, the use of the N-CQDs for luminescent thermometry has been demonstrated. For measurements in water, a decrease in intensity was noted along with increasing the temperature in the range of  $1\text{--}98^{\circ}\text{C}$ . A decrease in intensity by 51.0% at  $97^{\circ}\text{C}$  revealed a relatively low relative sensitivity of  $0.52\%/^{\circ}\text{C}$ . The reversibility of the measurements was also demonstrated through several heating-cooling cycles between  $20$  and  $40^{\circ}\text{C}$ . Temperature changes in HepG2 cells were visualized with confocal laser-scanning microscopy, and at  $20^{\circ}\text{C}$  the emission intensity was higher than at  $40^{\circ}\text{C}$ , which proved the potential of N-CQDs as intracellular temperature sensors.

The nitrogen doped carbon dots were studied also by Yang *et al.* who presented first implementation of absolute emission intensity based temperature-sensitive probes not only for *in vitro* but also *in vivo* imaging. The preliminary studies enabled temperature mapping in HeLa cells cultures.<sup>79</sup> Owing to the excitation with a 400 nm beam, a strong blue emission was observed, the maximum of which was located at 475 nm. After heating the cells, the intensity of the luminescence of this single band was analyzed, and the intensity at  $20^{\circ}\text{C}$  was assumed as the reference intensity  $I_0$ . As can be seen in Fig. 7, the strong blue emission observed at  $25^{\circ}\text{C}$  decreased when the cells were heated to  $37^{\circ}\text{C}$ . After the following cooling, the intensity again reached the initial value, thus confirming the reversibility and repeatability of the process. The dependence of the luminescence intensity on the temperature was assigned to the presence of surface functional groups ( $-\text{C}=\text{O}$ ,  $-\text{NH}_2$ ,  $-\text{OH}$ , etc.) and the breaking of the hydrogen bonds at higher temperatures that was affecting the hydrodynamic radius of the particles. There were numerous advantage of this material found, such as independence of  $I/I_0$  from the concentration of N-CQDs, strong stable emission at various pHs (range from 1 to 9), for various ionic forces (unchanged even in NaCl solution with 2 mol/L

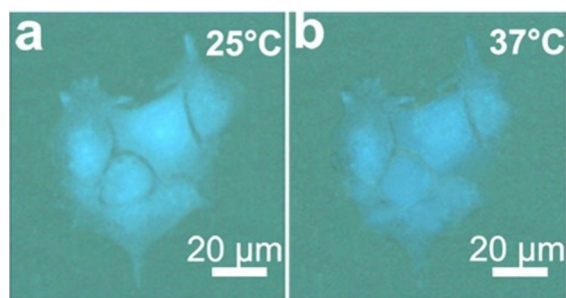


**FIG. 7.** HeLa cells imaged using luminescent N-doped carbon dots at a temperature of (a) 25 °C and (b) 37 °C.<sup>79</sup> Reprinted with permission from Yang *et al.*, ACS Appl. Mater. Interfaces 7, 27324–27330 (2015). Copyright 2015 American Chemical Society.

concentration) and the emissive properties stable in time (negligible changes after 8 months). Notwithstanding, carbon is known to be a highly absorbing material for which some of the absorbed energy can be converted into heat, which could affect the obtained results. Temperatures were assigned to a given luminescence intensity based on the heater parameters, however, it could be raised as a result of absorption and conversion of light into heat by carbon dots.

The further step was to implement those N-CDs also for *in vivo* imaging.<sup>79</sup> The nanoparticles were inserted into the back of the mice and the luminescence intensity of single band as a function of temperature was studied. The results at three different temperatures are presented in Fig. 8. There was no unambiguous information on how the given temperatures were achieved in the work. Probably, the carbon dots have been heated to a given temperature outside the living body and then injected. The signal in the spectral range of 500–700 nm with a step of 50 nm was collected immediately after the injection, however, this procedure did not allow reliable and quantitative indication of the temperature. Furthermore, the sample autofluorescence influence was not considered at all, while the photoexcitation wavelength of 400 nm is known to be strongly absorbed or scattered in the cells, reducing the penetration depth. The effects after treatment remained unknown, as the effects of the study, such as the death of mice, damage to organs or scars, have not been described. As indicated by the authors, the main advantage of the measurements based on the intensity of a single band originates from a simple measurement setup with no need to switch between emission filters.

The emission intensity of the single band in nanometric PbS/CdS/ZnS quantum dots ( $S = 1\%/^{\circ}\text{C}$  in the room temperature range)

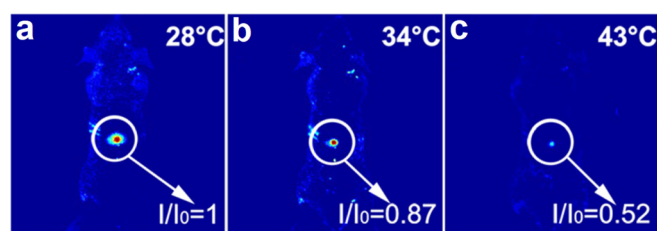


**FIG. 8.** Fluorescent images of a mouse with the injected N-CDs measured at different temperatures: 28, 34 and 43 °C.<sup>79</sup> Reprinted with permission from Yang *et al.*, ACS Appl. Mater. Interfaces 7, 27324–27330 (2015). Copyright 2015 American Chemical Society.

was also proposed to be used in the first thermometer for *in vivo* applications.<sup>80,81</sup> Owing to the outer ZnS coating, which shielded the deeper PbS core and the CdS shell from the environment, this material exhibited biocompatibility and low toxicity. The dual nature of PbS/CdS/ZnS QDs, manifested by the possibility of both heating and temperature reading, was revealed. The excitation with a single 808 nm wavelength, was followed by a non-radiative depopulation resulting in efficient light to heat conversion ( $\sim 43\%$ ) and a radiative transition evidenced by the emission band appearing in the area of the second optical window, which allowed luminescent imaging at a greater penetration depth without the autofluorescence from surrounding tissues. For this purpose, the emission intensity at 1270 nm was examined as a function of temperature (Fig. 9). The intensity of the temperature dependent emission band was strong enough to be detected with the NIR InGaAs camera even at a low concentration of QDs, and at a relatively low irradiation power density. With increasing temperature, the intensity decreased linearly and in a reversible manner. It was checked whether the photothermal heating was not affecting the ability to read the temperature. The IR emission was monitored twice in 4 min cycles after excitation with an 808 nm beam at  $2 \text{ W/cm}^2$ . Before and after each cycle, the laser power was reduced by 2 orders of magnitude to observe dots emission without the presence of significant heat. After each cycle, the intensity returned to the initial value which confirmed that the decrease in intensity during the photothermal process was associated only with temperature changes, and not with the physical or chemical degradation of the QDs.

The epidermal carcinoma A431 cells were implanted subcutaneously into the flank of the mouse and tumor growth was induced until it reached the size of  $100 \text{ mm}^3$ .  $60 \mu\text{L}$  of a QD solution in PBS at a concentration of  $5 \text{ mg/mL}$  were injected, and then, using a NIR camera, the emission spectrum of quantum dots was continuously collected in a 4-min cycle. At the same time, the surface temperature of the mouse was controlled using a thermographic imaging camera. The exponential decrease in QDs intensity within the tumor after 4 min-long irradiation with the 808 nm beam ( $1.7 \text{ W/cm}^2$ ) causing their temperature increase is presented on fluorescence images [Fig. 9(b)]. Other effects that may lead to intensity lowering (such as quenching due to enzymatic intravascular metabolism and gradual diffusion of QDs from tumor tissue) occur on a different time scale (hours or days), so the observed changes were attributed to temperature modifications. The significantly weaker intensity at the end of the process confirmed a meaningful increase in temperature in this area.

The difference between intratumoral and surface temperature as a function of the excitation power density was also examined aiming for hyperthermia of the tumor. As shown in Fig. 9(c), regardless of the power density, the internal temperature was always lower than the surface temperature, but together with the power density increase, the difference between these temperatures also increased. Such tests were carried out for power density from  $0.7$  to  $2.3 \text{ W/cm}^2$  and three ranges were found: (i) below  $1.5 \text{ W/cm}^2$ , which allowed to raise the temperature to only  $35^{\circ}\text{C}$  and merely caused the destruction of the tumor and (ii) between  $1.5 \text{ W/cm}^2$  a  $2.3 \text{ W/cm}^2$ , the area of effective photothermal therapy was determined. In this compartment, the intratumoral temperature might increase from  $35^{\circ}\text{C}$  to  $50^{\circ}\text{C}$ , which overheated the tumor without significant damage to the surrounding cells. The observed skin temperature at the end of the 4-min heating process was around  $55^{\circ}\text{C}$ ; (iii) over  $2.3 \text{ W/cm}^2$ , where excessive overheating above

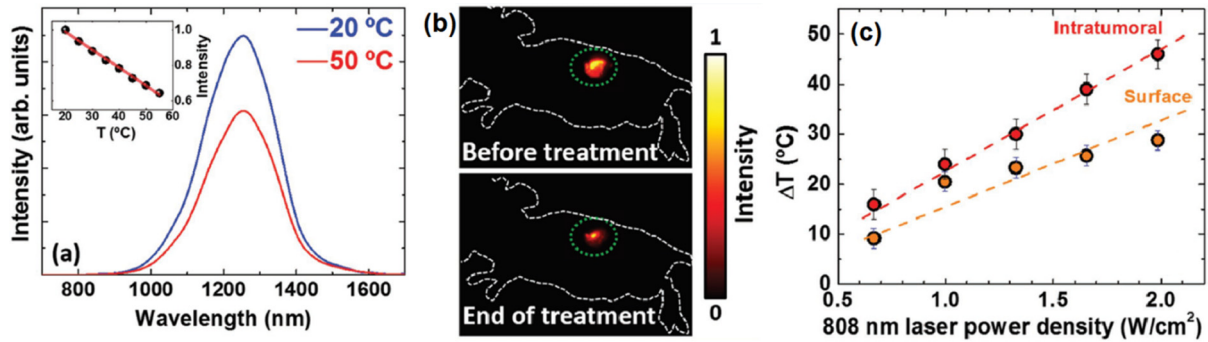


**FIG. 9.** *In vivo* thermal imaging using QDs: (a) emission intensity of the PbS/CdS/ZnS QDs centered at 1270 nm measured at different temperatures. On the inset the linear calibration curve normalized to the value at 20 °C is presented; (b) representative NIR luminescence images collected before and after 4 min treatment, where a significant decrease in the emission intensity can be seen; and (c) *in vivo* intratumoral temperature increment, as calculated from the QD emission quenching and surface temperature increment, as measured with a thermographic camera for different irradiation power densities.<sup>81</sup> Reprinted with permission from del Rosal *et al.*, *Adv. Opt. Mater.* **5**, 1600508 (2017). Copyright 2016 John Wiley and Sons.

50 °C, destruction of cells surrounding the tumor and significant skin burning were occurring. The tumor size in non-irradiated mice increased significantly, whereas in mice subjected to therapy was destroyed, leaving a burned wound on the skin, and after 3 weeks of therapy only a scar.

Taking into account the need of the nontoxicity of materials in the case of biomedical applications, in 2019, Zhang *et al.*<sup>82</sup> proposed to use gold nanoparticles (AuNCs) with excitation and emission bands at 430 and 610 nm, respectively, to image cells with a temperature resolution of 0.73 °C in the biologically relevant temperature range 35–42 °C. Temperature dependent decrease in AuNC emission intensity is typically originating from the loss of energy by reducing network rigidity and Auoplic interactions. It is also possible to reduce the binding strength of the Au core to the ligands, which reduces the charge transfer from the ligands—which consequently reduces the emission intensity. The calibration curve was examined outside the cells. After their introduction into hepatic stellate cells, and as the sample was heated from 10 to 40 °C, the AuNPs were showing less and less emission.

## B. Spectral shift of the emission band or absorption edge

The spectral shift of the emission bands [Fig. 2(b)] or absorption edge [Fig. 2(i)] is relatively complex to the image, since usually high resolution hyper-spectral imaging is required to quantify sub 10 nm shifts per 1 °C. Acousto-optical tunable filters or 32 channel PMT, which can be used for wide field or confocal raster scanned microscopy, respectively, do not offer sufficient spectral resolution. Because the recorded emission wavelengths are of the order of 500 nm to around 1500 nm (the denominator in  $S_R$  equation), while both spectral shifts and vibrationally induced broadening usually cover only a few nm (the nominator in  $S_R$ ), the relative sensitivity using the spectral shift is usually limited below  $1\%K^{-1}$ . Moreover, from practical perspective, the nanomaterials showing this effect are almost exclusively semiconductor quantum dots<sup>83</sup> whose emission spectra are relatively broad, thus hinder the determination of exact wavelength of the emission band maximum. While some indirect methods may be proposed

to quantify  $d\lambda/dT$ , such as the one presented in Fig. 2(b), the emission integrals at two closely located spectral bands must be quantified. This non-trivial task is affected by the background signal or emission band shape. The former occurs when LT photoexcitation directly initiates autofluorescence from other endogenous and exogenous fluorophores. The latter may happen, when the LT luminescence is absorbed by these chromophores, water or other non-fluorescent molecules such as hemoglobin (inner filter effect—IFE). In consequence, not only the readout will depend on the depths the temperature dependent luminescence comes from, but also may vary proportionally to the skin pigmentation and thickness or tissue composition (e.g., in response to periodic variability of oxy- to deoxy-generated blood). Similar issues are valid for either temperature shifting the emission band or shifting the absorption edge.

The thermometric parameter using the relative spectra shift technique (SST) can be generally defined as

$$T \sim \Theta(T) = [\lambda_{\max}(T) - \lambda_{\max}(T_0)] \sim \delta\lambda_{\max} \sim \frac{B_1(T)}{B_2(T)}, \quad (11)$$

where  $\lambda_{\max}(T)$  is the wavelength at which either emission or absorption band is the highest. One needs relatively narrow bands to reliably determine the  $\Delta$  directly. In the imaging mode, the  $\Delta(T)$  can be quantified as the ratio between emission intensities in two fixed, neighbor spectral bands ( $B_1$  and  $B_2$ ), by using a sharp edge dichroic or bandpass filters and a camera suitable to record 2D intensity images at the two spectral channels  $I_{B_1}(T)$  and  $I_{B_2}(T)$  under a single excitation line [Eq. (11)]. The artifacts can originate from the presence of autofluorescence in spectral windows defined by the spectral filter used for imaging, i.e.,  $A_{B_1}$  and  $A_{B_2}$ . Even if the autofluorescence will be assumed to not vary with temperature or time, its intensity affects the outcome temperature maps [Eq. (12)]. If the relative changeover studied temperature range is constant, e.g.,  $S_R = 0.5\%/^{\circ}C$ , knowing the initial temperature  $T_0$  and assuming homogenous excitation illumination and nonmoving objects, one may determine spatial temperature maps as

$$T(x, y) = T_0(x, y) + C \cdot \frac{I_{B_1}(x, y, T) + A_{B_1}(x, y)}{I_{B_2}(x, y, T) + A_{B_2}(x, y)} \cdot \frac{1}{S_R}. \quad (12)$$

Similarly to intensity based temperature mapping, the initial temperature map is actually difficult to know before the experiment, thus the temperature rise in respect to the starting conditions can be only found, in response to some stimulus (e.g., drugs, toxicants, local heating, etc.). Therefore, the relative temperature change can only be quantified

$$\delta T(x, y) = C \cdot \frac{I_{B1}(x, y, T) + A_{B1}(x, y)}{I_{B2}(x, y, T) + A_{B2}(x, y)} \cdot \frac{1}{S_R}. \quad (13)$$

Assuming of non-existent autofluorescence (e.g., by using anti-Stokes luminescence reporters) cancels the  $A_{Bn}$  terms. Using very bright reporters ( $I_{Bn} \gg A_{Bn}$ ,  $n = 1, 2$ ) diminishes  $A_{Bn}$  terms ( $A_{Bn} \rightarrow 0$ ) as well. In consequence, these two methods simplify Eq. (13). The spectral shift method is additionally susceptible to the spectral width of the emission bands (i.e., the broader the emission band, the smaller sensitivity), a reflection of the filters (i.e., to avoid spectral bleed-through) and steepness of the transmission band of the chosen filters.

The temperature measurement method based on the spectral shift of the emission wavelength as a function of temperature is best known in the case of the quantum dots. This phenomenon occurs due to a number of different effects, for example due to temperature dependent changes in the bandgap energy, quantum effects, electron phonon coupling [DOS(T)], a variation of the quantum yield, thermal expansion of crystalline lattice [ $r(T)$ ], and change of the solvent refractive index. The spectral shift in quantum dots used for thermal measurements is described by Varshni empirical law<sup>84</sup>

$$E_g(T) = E_g(0) - \frac{\alpha T^2}{T + \beta}. \quad (14)$$

The use of previously widely described materials such as CdSe QDs allows the use of their well-known emission redshift with increasing temperature. Moreover, the use of QDs provides known synthesis methods, uniform shapes and sizes, and the possibility of an easy bio-modification of their surface.

One of the first demonstrations of suitability of this method for temperature estimation in the *in vitro* environment was demonstrated in 2010 by Maestro *et al.*,<sup>85</sup> who used two-photon fluorescence microscopy of CdSe quantum dots [CdSe spherical nanoparticles of 4 nm in diameter from Invitrogen, (Qtracker 655)] to measure temperature in HeLa cervical cancer cells. This excitation allowed for a much higher sensitivity than for one-photon excitation. CdSe QDs allowed to measure the temperature in two different ways, because both the emission intensity and the position of their emission peak were strongly temperature dependent. The latter fact enabled the temperature measurement regardless of whether QDs were distributed evenly or not in the imaged region. The variation of 0.16 nm/°C was determined for the spectral shift (based on the calibration curves obtained in the PBS). To incorporate QDs into the cells, a 2-h incubation was carried out, however the distribution inside the cells turned out to be inhomogeneous. Fortunately, the temperature dependence of the spectral shift of the emission peak was independent of the QD distribution. The temperature assessed on the basis of the spectral shift proved to be constant for the cell area. Therefore, the cell temperature was changed externally via a microair-heater and an increase in temperature was observed from 25 °C to 50 °C after 3 min of heating. Despite the uneven distribution of these nanothermometers in the cell,

temperature mapping in this case was inaccurate, but showed the potential of quantum dot labels for temperature measurement in the cellular environment.

Another report on the use of commercially available quantum dots [Qtracker 655 Cell Labeling Kit (Q25021MP, Invitrogen)] for measuring cell temperature was presented by Tanimoto *et al.*<sup>86</sup> Although the described measurement was claimed to be ratiometric, actually it was based on the temperature dependent emission band red shift (0.105 nm/°C). Therefore, achieving a detection resolution of around 1 °C would require a very high spectral resolution. Instead, the authors proposed to measure the integrated intensity above and below a certain defined wavelength and the change in their ratio as a function of temperature was studied in a confocal laser scanning microscope. The authors emphasized that the use of such methodology allowed to eliminate errors, resulting for example from photobleaching (a special fitting curve was used). The temperature was additionally monitored with a thermocouple and controlled with a stage-top incubator. After the excitation of the QDs with a 405 nm laser, two spectral ranges were measured with PMT, 630–650 and 650–670 nm. In order to obtain the intensity ratio, the integral intensity of longer wavelengths (650–670 nm) was divided by the integral intensity of shorter wavelengths (630–650 nm). For a single QD measurements (outside of the cellular environment), the curve slope of the 0.062/°C was obtained in the temperature range of 31–41 °C. In addition, cyclic changes in temperature between two different temperatures (40 and 30 °C) confirmed reproducibility of measurements. Then, a similar measurement was made for a single QD introduced by incubation into SH-SY5Y living cells. In this case, the relationship between the ratio of the intensity and the temperature was also obtained and the slope of the curve was determined as 0.067/°C (i.e., no effect of the cytoplasmic environment was observed). Additionally, the authors showed the heat production by mitochondria after the addition of 10 μM CCCP (carbonyl cyanide 3-chlorophenylhydrazone) reagent. To locate the mitochondria, cells were labeled with MitoTracker Green FM (M7514, Molecular Probes) and Hoechst 33342. The intensity of a single QD emission near the mitochondrion was measured every 30 s after the addition of the reagent and an increase in temperature was recorded. The authors also described a method of imaging temperature differences in the cell body and in the nucleus. The QDs were excited by 405 nm or 488 nm lasers, and the images were captured by PMTs through appropriate dichroic mirrors and emission filters. A 0.1 difference in intensity ratio for the nucleus and cell body was found, which corresponded to the temperature difference of 1.6 °C. The maximum relative sensitivity obtained for the described method was 6.3%/°C.

A new approach allowing for temperature assessment via testing band shift without the need for nanothermometer calibration was proposed for the first time in 2019 by Savchuk *et al.*<sup>87</sup> who involved commercially available green fluorescent proteins (GFPs). This approach makes the measurement independent of the total intensity of the sample emission. The GFP shows emission in the green spectral range, and by defining two ranges: below the maximum ( $I_1$  being defined as the integral intensity between 495 and 509 nm imaged by the green channel) and above the maximum ( $I_2$  being defined as the integral intensity between 510 and 600 nm imaged by the red channel), they can be observed simultaneously and a reliable parameter depending on the temperature may be defined as  $PF = (I_2 - I_1)/I_{total}$ . Normalizing this difference to the total intensity of the band makes

temperature measurement more accurate and independent from photobleaching and other undesirable effects. Measurements were also made on HeLa cells using GFP located at the mitochondria (CellLight BacMam 2.0 Mitochondria-emGFP). Importantly, the impact of pH and ionic strength (by the addition of KCl) was verified in fixated cells, which showed that the GFP used was also independent of changes in these parameters in living cells that may occur due to some biological processes. It was demonstrated that for GFP inside HeLa cells, the shift of emission maximum from 509 nm for 20 °C to 512 nm for 35 °C was observed. Thermal uncertainty  $\delta T = 0.25$  °C and a relative sensitivity of  $S_r = 2.2\%/^{\circ}\text{C}$  was reached. Furthermore, imaging of cells in which heat production occurred under the influence of FCCP uncoupler reagent was also provided, proving that the described method is capable to trace the evolution of temperature growth by around  $\Delta T = 3$  °C after the chemical stimulus. At the same time, the method was able to evidence gradients of temperature, pointing out temperature heterogeneity. It was noted that the mitochondrial regions closer to the cell nucleus were warmer. The described nanothermometer shows a significant sensitivity of temperature readout in the biological range and enabled temperature imaging with sub-cellular spatial resolution.

Another example of nanothermometry, which can be associated with frequency shift (of continuous-wave electron spin resonance (ESR) spectrum this time), employed nitrogen-vacancy spin of color centers in nanodiamonds (Fig. 10).<sup>12</sup> The nanodiamonds are inert, robust to changes in the local chemical environment and operate in a wide (e.g., 200–600 K) temperature range with high, up to  $80 \mu\text{K Hz}^{-1/2}$  sensitivity for nanodiamonds with c.a. few hundreds to 1000 nitrogen vacancies per nanoparticle (actually 1.8 mK measurement accuracy was achieved). Such nanoparticles offer also high spatial resolution  $<200$  nm. From the other side, the magnetic field susceptibility requires a dedicated spin-echo sequence technique to eliminate the effects of an external, slowly varying magnetic field. Although successful sub cellular temperature gradients imaging in a Esingle human embryonic fibroblast has been demonstrated with very high sensitivity, the concept of temperature dependence of the zero-field splitting of the ground triplet state into its different spin projection states (recorded in microwave domain) is quite sophisticated and may be difficult to adopt widely.

### C. Relative emission bands intensities under single excitation

Ratiometric emission LTs are considered to be the most reliable temperature probes. This is because the normalization of

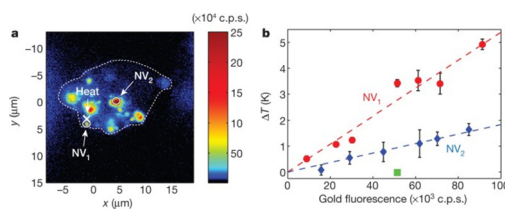


**FIG. 10.** A demonstration of nanodiamond thermometry in into human embryonic fibroblast WS1 cells ( $\lambda_{\text{exc}} = 532$  nm,  $\lambda_{\text{em}} > 638$  nm) with gold NPs nanoheaters, (a) confocal image of a single cell and (b) measured changes in temperature at the positions NV<sub>1</sub> and NV<sub>2</sub> relative to the incident laser power applied to the gold NP (and thus its fluorescence intensity).<sup>12</sup> Reprinted with permission from Kucsko *et al.*, Nature 500, 54 (2013). Copyright 2013 Springer Nature.

thermometric parameter  $\Theta$ —i.e., the intensity at one emission band is related to the intensity of the other emission band, and in principle, this ratio shall be independent of numerous experimental conditions, such as excitation intensity or variations in transmission at the path of excitation and luminescence. This is typically true for most *in vitro* studies, because up-right microscopes make the photoexcitation and luminescence penetrate in a predictable short paths, thus photoexcitation intensity can be controlled. Unfortunately, the *in vivo* experiments are not always reliable enough, due to the inhomogeneous composition and more complex tissue spectroscopy. Not only heterogeneous tissues scatter light in an unpredictable manner, but also numerous chromophores absorb or emit their own light under direct photoexcitation or indirectly—i.e., being excited by LTs luminescence. Additionally, spectral properties of tissues may dynamically change as a result of oxy- and deoxygenated blood pulses or even with temperature itself.<sup>66,88,89</sup> Other issues, such as skin pigmentation, fat content, vasculature, composition, and homogeneity may additionally impair reliable temperature mapping, especially because the calibration of LTs *in vivo* cannot, in principle, be performed.

From the perspective of temperature detection and mapping, the ratiometric technique is relatively simple to implement either *in vitro* or *in vivo*. For *in vitro* T mapping, a wide field fluorescence microscope with an appropriate switchable filter can be used, followed by image processing, i.e., co-localizing pixels and dividing one image by the other to get. Using dichroic, sharp edge optical filter enables to employ even small (anti)Stokes shifts to determine  $\Delta$ . More advanced (but more costly as well) solution is using hyperspectral tunable filters or a 3CCD cameras. On one hand, such alternatives neglect any mechanical and time-ineffective switching between the filter cubes in the microscope, on the other hand, the spectral filtering cannot prevent some spectral bleeding of signal between the channels and is affecting the sensitivity of ratiometric sensing. Confocal raster scanning with 32 Channels PMT is a rather expensive solution with limited spectral resolution sufficient for broadband emitting LTs (e.g., organic dyes), but it may not be satisfactory for narrowband LTs (e.g., QDs,  $\text{Ln}^{3+}$ , TM). Nipkow disks may improve the imaging speed in confocal highly resolvable imaging, but then at least two spectral images must be acquired for ratiometric detection. The *in vivo* ratiometric temperature mapping exploits either tunable filters or switchable static filters. The most severe drawback of this approach is the fact, that one is usually not aware of how the spectral properties of tissues affect the  $\Delta$ , and how reliably the temperature is determined.

To define thermometric parameter using the relative intensity of two emission bands  $I_{Bn}(T, \lambda_{\text{exc}})$  ( $n = 1, 2$ ) under a single excitation line ( $\lambda_{\text{exc}}$ ) is relatively simple, when sample autofluorescence  $A$  is absent (i.e., due to anti-Stokes emission or due to negligible intensity)

$$\Theta(T) = C \cdot \frac{I_{B1}(T, \lambda_{\text{exc}})}{I_{B2}(T, \lambda_{\text{exc}})} = C \frac{I_{LTB1}(T, \lambda_{\text{exc}}) + A(\lambda_{\text{exc}})}{I_{LTB2}(T, \lambda_{\text{exc}}) + A(\lambda_{\text{exc}})} \sim \frac{I_{LTB1}(T, \lambda_{\text{exc}})}{I_{LTB2}(T, \lambda_{\text{exc}})}. \quad (15)$$

One may determine spatial temperature maps as

$$T = \frac{I_{LTB1}(T, \lambda_{\text{exc}})}{I_{LTB2}(T, \lambda_{\text{exc}})} \cdot \frac{1}{S_R}. \quad (16)$$

By using simple mathematical recasting of  $\Delta$  parameter, Brites *et al.* demonstrated the so-called primary thermometer,<sup>69</sup> which eliminates



the need for recalibration of the temperature sensitive system, due to different absolute behavior of the temperature probe (e.g., owing to different medium or intensity of excitation). Such an approach, which is critical for the reliability of T readout and mapping, is rarely discussed in scientific literature, but knowing the mechanism standing behind the temperature dependent relationship, enables to define other primary thermometers.

In 2011 Ye *et al.*<sup>90</sup> used a ratiometric temperature sensor based on semiconductor polymer dots (Pdots) and an attached thermo-sensitive dye, rhodamine B (RhB). To increase the sensitivity of the temperature readout, the Pdot-RhB nanoparticles could be excited with a single excitation line, using an efficient FRET mechanism from the Pdot to the RhB [Fig. 11, Left (a) and (b)]. The use of the Pdots enabled an easy manipulation of the sensor size and ensured very high emission brightness. The rhodamine B is a dye whose emission intensity is strongly quenched by temperature, which provides the possibility of accurate ratiometric temperature readout. The authors developed two types of sensors, PEPV-RhB and PEBT-RhB, with hydrodynamic diameters of 22 and 160 nm, respectively. Excitation at 450 nm resulted in the polymer emission at around 540 nm, which coincided with the RhB absorption peak. Ratiometric Pdots intensity measurement (510 nm) and RhB (573 nm) as a function of temperature showed a linear relationship in the 10–60 °C temperature range [Fig. 11, Left (c)–(f)]. PFBT-RhB was used to measure the temperature of living HeLa cells Fig. 11. (Right) into which, the polymer was introduced via endocytosis without additional reagents. The imaging was performed using a fluorescence confocal microscope, and the temperature was controlled by the heating stage (additional temperature readout was made with a digital thermocouple dipped into the cell solution). A diode laser of 458 nm was used as an excitation line. The integration time for a single pixel was equal 1.6  $\mu$ s. Figure 11 shows

the decrease in the red channel intensity (507–518 nm integration) with the temperature change from 13.5 to 36.5 °C, while the intensity of the green channel (571–582 nm integration) remained stable. Ratiometric luminescence temperature reading in cells using PFBT-RhB was equal to  $13.2 \pm 0.9$  and  $35.7 \pm 1.8$  °C for the measured solution temperature of 13.5 °C (thermocouple error  $\pm 0.5$  °C) and 36.5 °C, respectively.

The derivative of Rhodamine B (RhBAM) was attached also to another ratiometric thermometer proposed in 2014 by Qiao *et al.*<sup>91</sup> However, this time a different green sensor, 7-nitro-2,1,3-benzoxadiazole (NBD) was used. To avoid FRET between the dyes, which was an adverse effect in this case, the dyes were attached to the separated chains of poly N-isopropylacrylamide (PNIPAm) polymer. The target ratiometric sensor was created using mixed PNIPAm-co-NBDAA and PNIPAm-co-RhBAM polymers, whose ratio was optimized and determined as 100:1. Moreover, it has been shown that the effect of various concentrations of ions, pH, and proteins demonstrated an insignificant influence on the temperature reading in the physiological temperature range. Low cytotoxicity and good biocompatibility were also confirmed. Ratiometric temperature measurement was performed at a single excitation line of 488 nm and the thermal dependence of the emission intensity ratio at 530 nm (PNIPAm-co-NBDAA) to 571 nm (PNIPAm-co-RhBAM) was investigated. The emission intensity of PNIPAm-co-NBDAA increased relatively strongly with the temperature rise (over the 28–43 °C temperature range), while the PNIPAm-co-RhBAM intensity increased only slightly. To test the effectiveness of this thermometer under biological conditions, the studies were conducted in live HeLa cells. A spontaneous uptake by HeLa cells (via endocytosis) was achieved by incubation for 3 h at 28 °C. The thermal imaging (performed on a confocal laser scanning microscope) of living HeLa cells revealed the increase in the intensity collected in the green

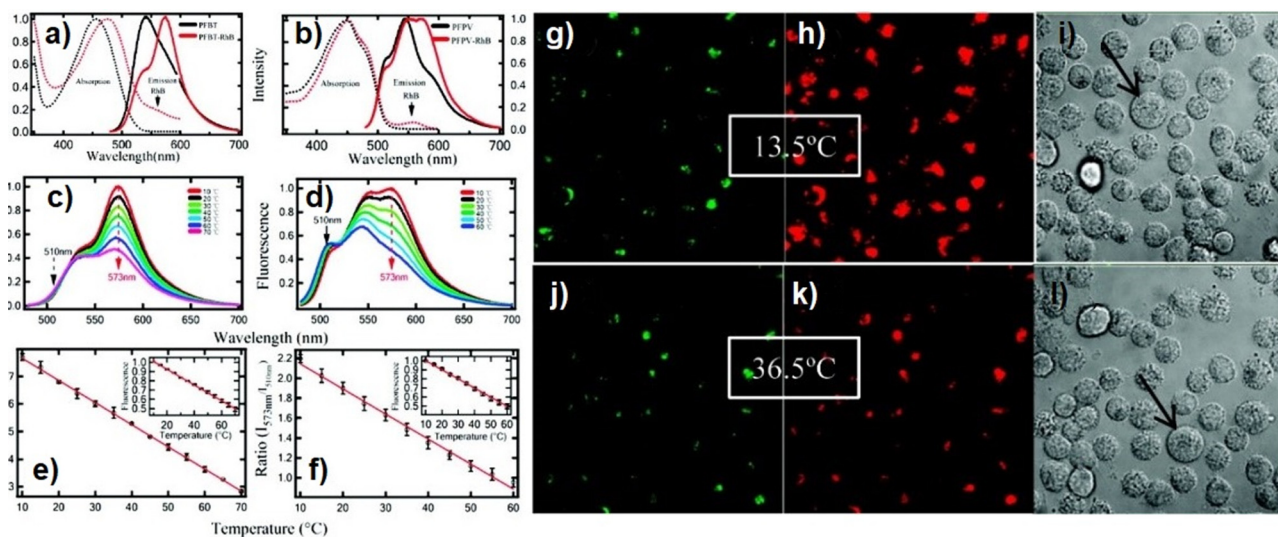


**FIG. 11.** Fluorescence imaging using rhodamine B (a) and (b) Absorption and emission spectra (the arrow shows the RhB absorption peak). (c) and (d) Fluorescence spectra at different temperatures at 450 nm excitation. (e) and (f) The ratio of 573 to 510 nm band as a function of temperature (inset: normalized band intensity 573 as a function of temperature)—error bars show the standard deviation for three independent measurements. (g), (h), (j), and (k) Images from confocal microscopy of HeLa cells with PFBT-RhB at 458 nm excitation at 13.5 °C and 36.5 °C, respectively, for 507–518 nm (green) and 571–582 nm channels (red). (i) and (l) Bright field images for the corresponding areas.<sup>90</sup> Reprinted with permission from Ye *et al.*, *J. Am. Chem. Soc.* **133**, 8146–8149 (2011). Copyright 2011 American Chemical Society.

channel (510–560 nm) and a minor increase in the red intensity (570–670 nm) when the temperature was altered from 33.3 °C to 39.2 °C. Therefore, a thermal resolution of 0.3–0.5 °C for HeLa cells was obtained. Moreover, it has been shown that the sensor described was able to visualize changes in an intracellular temperature after adding FCCP reagent.

Another temperature sensor based on the poly *N*-isopropylacrylamide (PNIPAM) polymer was described by Liu *et al.*<sup>92</sup> in 2015. Dipyren-1-yl(2,4,6-triisopropylphenyl)borane (DPTB) was modified to enable a covalent connection to PNIPAM nanogel (PNDP) to obtain green emission. To overcome the drawbacks of a single emission measurement, the Nile Red (NR) dye was freely distributed in the hydrophobic domains of the nanogel dye (enabling an efficient FRET between DPTB and NR) which served as a reference for ratiometric readout. Temperature changes could be studied even with the naked eye because the color of the emission changed from red to green–blue in the range of 30–55 °C. Absorption peak of NR at 525 nm was overlapped with the fluorescence of PNDP, thus an efficient FRET was observed with photoexcitation at 405 nm. The green luminescence of PNDP at 470 nm was enhanced by increasing temperature, while NR emission at 625 nm was slightly reduced (FRET efficiency was decreased by temperature increase). The intensity ratio of 470 nm to 625 nm showed 13-fold linear increase in response to temperature rise from 34 to 56 °C with temperature resolution equal 0.2 °C. Additional measurements confirmed the reversibility of the PNDP-NR thermometer as well as its good stability. Intracellular imaging of living cells at different temperatures (using a confocal microscope and a heating stage) was performed for NIL/3T3 cells after the previous 30 min last- ing incubation of LTs without additional reagents

In 2015 based on his previous studies, Uchiyama *et al.* modified one of the intracellular temperature sensors based on lifetime<sup>93</sup> to obtain a ratiometric readout.<sup>94</sup> This new fluorescent polymeric thermometer was based on the thermosensitive polymer *N*-*n*-propylacrylamide (NNPAM) combined with cationic 3-acrylamido-propyl-trimethylammonium (APTMA) unit and two fluorescent units: (DBThD-AA) and (BODIPY-AA). The NNPAM unit was adopting an extended structure at low temperatures and was shrinking at high temperatures. The contraction resulted in the release of water molecules (that act as effective luminescence quenchers) away from fluorescent unit DBThD-AA, what made its luminescence temperature dependent. The APTMA unit supported the spontaneous internalization of molecules by living cells and prevented aggregation. Both, DBThD-AA unit with temperature-dependent emission intensity and BODIPY-AA unit, which provided a reference signal, might be excited at 450–500 nm, and they showed distinct emission maxima at 510–515 and 560–585 nm, respectively. A strong correlation of the intensity ratio 580/515 nm with temperature was demonstrated with the sensitivity of 4.1%/°C (between 25 and 45 °C). Moreover, the sensor had been verified for its insensitivity to its own concentration, ionic strength of the medium (0.25–0.35), and surrounding pH (6–9). The fluorescence properties inside the cells were also investigated. To introduce the LTs into MOLT-4 and HEK293T cells, they were incubated for 10 min at 25 °C. The fluorescence imaging of both types of cells was performed using a confocal microscope (with a cage incubation chamber to control the temperature). The emission from the thermometer was obtained in the range of 500–600 nm with the excitation line of 473 nm. The fluorescence intensity at each wavelength was

calculated from fluorescence images by summing and averaging the fluorescence intensity in all pixels in a single HEK293T cell (thermal images of cells were not shown, only the graphs created on their basis were analyzed). For MOLT-4 cells thermal resolution of 0.01–0.25 °C was determined in the range of 25–44 °C, and for HEK293T cells 0.29–1.0 °C in the range of 27.5–37.5 °C. Interestingly, in the HEK293T cells, a temperature difference of about 1 °C between the nucleus and the cytoplasm was also observed. The authors emphasized that the use of a ratiometric method of temperature measurement was much more practical, as it allowed to obtain the temperature image in about 1 s, while the imaging method using lifetime measurements required c.a. 1 min of data acquisition.

Another polymer based thermometer proposed by Hu *et al.*<sup>95</sup> in 2015 utilized a cascade FRET mechanism to improve its the sensitivity. They engaged three CMA, NBD, and rhodamine B (RhBEA) fluorescent monomers copolymerized separately with *N*-isopropylacrylamide (NIPAM) polymer. The obtained dye-labeled PEG-*b*-P(NIPAM-*co*-CMA), PEG-*b*-P(NIPAM-*co*-NBDAE), and PEG-*b*-P(NIPAM-*co*-RhBEA) emitted blue, green, and red light, respectively. Thermosensitive NIPAM polymer altered its conformation from the open form at low temperatures to a shrunk version at high temperatures, facilitating an effective FRET by shortening of the distance between the dyes. The authors examined the phenomenon of regular (one step) FRET for pairs of dyes, but the highest temperature sensitivity and performance was obtained for a cascade FRET using all three dyes mixed in the optimized proportions. In the case of the cascade FRET, the change in the emission intensity ratio of 585/422 nm for raising the temperature from 20 to 44 °C was found to be 8.4-fold. The highest slope was 0.3 °C<sup>-1</sup> for 35.9 °C. What is more, the insensitivity of all the dyes emission to pH changes was confirmed. Cytotoxicity measurements were performed in HepG2 cells and the LTs were found to be nontoxic. Intracellular thermal mapping in HepG2 cells was performed using both ratiometric thermometer types, using one-step and cascade FRET. The calibration curve of LTs was obtained in cell extract beforehand. Three channels were investigated: blue in the range 410–450 nm, green in 510–550 nm, and red in 565–605 nm. 405 nm was the excitation line for CMA-NBDAE, CMA-RhBEA, and CMA-NBDAE-RhBEA, and 488 nm for the NBDAE-RHBEA. The obtained images clearly showed that at the increased temperature the red emission increased more significantly, in contrast to the blue one [Fig. 12(a)]. The sensitivity obtained from the curve for a ratiometric measurement [Fig. 12(b)] was lower than 1 °C for the range 34.2–40.5 °C [Fig. 12(c)] and it reached 0.40 °C at 37 °C. What is more, the authors noted the expected increase in cell temperature after the addition of 100 mM glucose [Fig. 12(a), last column].

The confirmation of the suitability of thermoresponsive polymeric materials for applications in ratiometric luminescence nanothermometry was also presented by Qiao *et al.*<sup>96</sup> in 2015. The sensor consisted of a NBDAE fluorescent dye, a temperature-sensitive polymer (NIPAM), and a NSVB monomer providing a reaction with the amino groups which could be covalently moiety toward amino groups of the Tf protein. In addition, fluorescent protein-stabilized targeting gold nanoclusters (TfAuNCs) were attached (ratiometric fluorescent unit) to the sensor. In the resulting polymer–TfAuNCs sensor, the NBDAE luminescent properties changed with temperature due to changes in the NIPAM polymer conformation (increase in emission intensity for temperature increase). What is more, the properties of

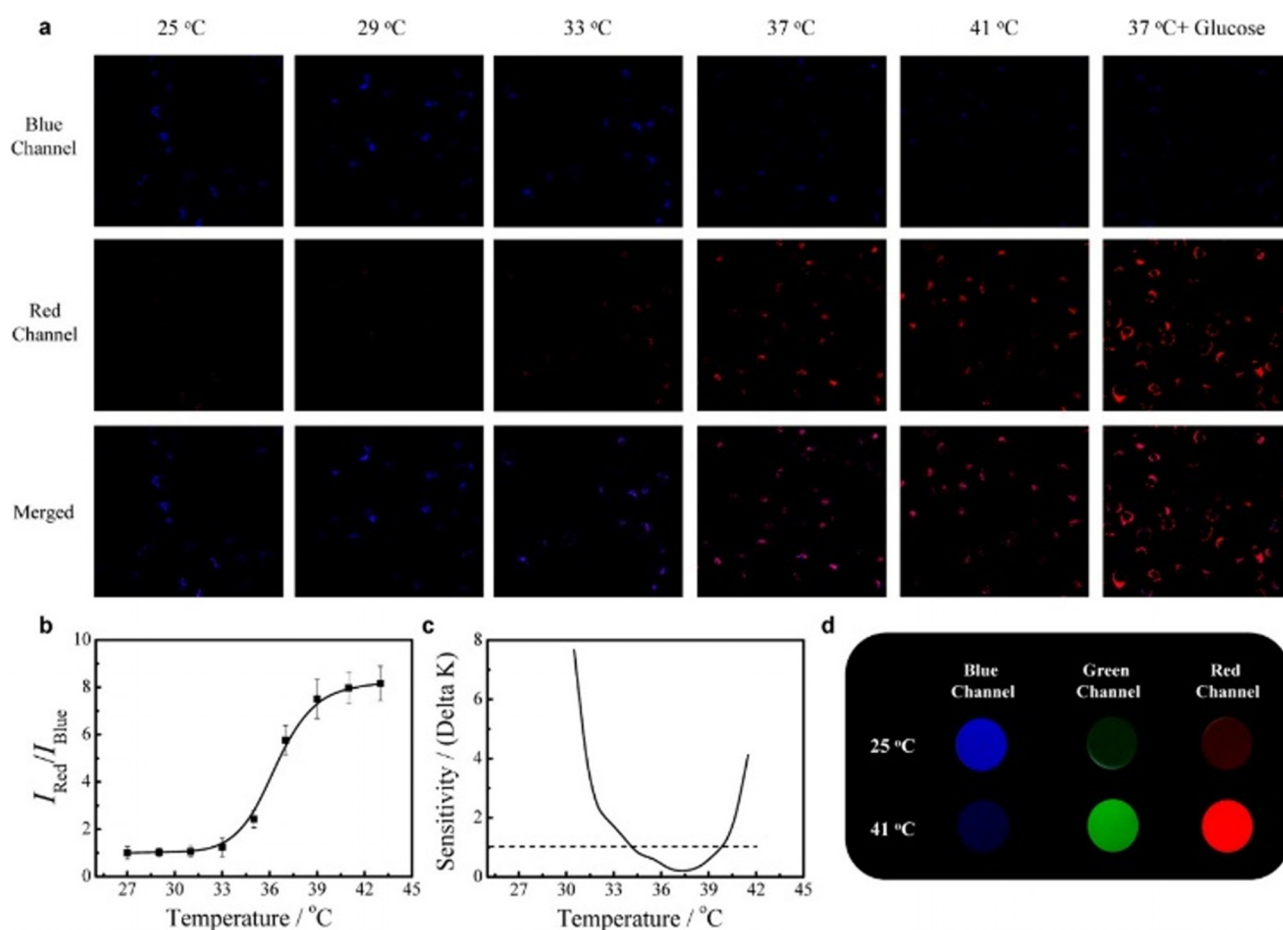


**FIG. 12.** Cascade FRET in polymers as fluorescent thermometer C3. (a) Images from confocal fluorescence microscopy for blue and red channels and merged—for temperature changes from 25 to 41 °C (columns 1–5) and for cells stimulated with glucose at 37 °C (column 6). (b) The intensity ratio of the green/blue channel. (c) Sensitivity. (d) Change in intensity shown in fluorescence images in three channels at 25 and 41 °C.<sup>95</sup> Reprinted with permission from Hu *et al.*, ACS Appl. Mater. Interfaces 7, 15551–15560 (2015). Copyright 2015 American Chemical Society.

the TfAuNCs unit also assisted the spontaneous entry of the sensor into living cells. The ability of the sensor to measure temperature was checked using a single 488 nm excitation line and the emission intensity of NBDAA at 545 nm and of the TfAuNCs at 659 nm were analyzed. The emission intensity of NBDAA strongly increased with increasing temperature, while the intensity of the TfAuNCs increased only slightly (probably due to the spectral overlap of both fluorophores) and the linear changes of the intensity ratio 545/659 nm with temperature changes were observed. The authors presented the insensitivity of the optical response in a variable temperature to electrolytes, pH (with small exceptions) and proteins, and also demonstrated its biocompatibility. Slow 40 s response time of the polymer-TfAuNCs and 20 min incubation time was necessary. HeLa cell imaging was performed at different temperatures between 25.0 and 39.7 °C and the ratiometric measurement result is shown in Fig. 13. The polymer-TfAuNCs was found to be dispersed in the cytoplasm and there was no transfer to the cell nucleus. Ratiometric images were prepared by measuring the intensities of two channels: 510–560 nm and 570–670 nm. The linearity of the calibration curve in the range of

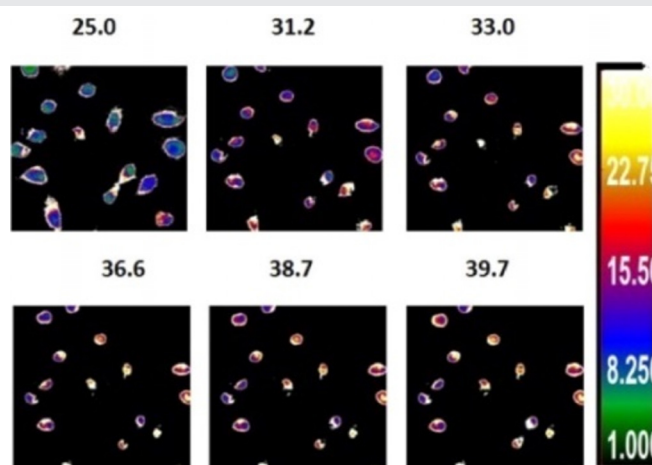


**FIG. 13.** Fluorescence (ratiometric) imaging with temperature-sensitive polymer (NIPAM) conjugated with TfAuNCs.<sup>96</sup> Reprinted with permission from Qiao *et al.*, Anal. Chem. 87, 10535–10541 (2015). Copyright 2015 American Chemical Society.

31.8–38.5 °C was obtained for the whole cell, whereas the thermal resolution in HeLa cells was determined as 0.3–0.5 °C. In order to further test the sensor, it has been shown that it allowed to register an increase in cellular heat production following calcium ions stress by the ionomycin inducement. The temperature increase from 34.5 to 39 °C was noted about 2 min after chemical stimulation.

In 2016, Wang *et al.*<sup>97</sup> proposed a ratiometric temperature sensor based on a nanohybrids composed of the carbon dots (CDs) and the gold nanoclusters (AuNCs) emitting in blue and red, respectively. This dual-emitting temperature sensor based on the carbodiimide-activated coupling of glutathione-stabilized AuNCs and amino-functionalized CDs exhibited a tunable emission depending on the excitation line used (for excitation in the 370–500 nm range, a shift of the emission peak from 456 to 550 nm could be observed). To obtain well-separated emission peaks, a 365 nm line that was used to simultaneously excite both materials, resulting in emission peaks of 430 nm (CDs) and 605 nm (AuNCs). Based on the quantum yield results measured for CDs and AuNCs separately and in the form of nanohybrids, slight energy transfer between the AuNCs and the CDs was found. The luminescent properties of nanohybrids were tested as a function of temperature in the range of 20–75 °C. The intensity of AuNCs emission was strongly quenched by the high temperature due increased rates of non-radiative recombination of holes and electrons. For the AuNCs emission, changes with a temperature of about 1.8%/°C were noted. Because the emission of CDs changed insignificantly as a function of temperature, the intensity ratio of 430/605 nm increased with increasing temperature and the ultimate emission color of the nanohybrids changed from red to violet. No spectral shifts of the emission peaks were observed in the studied temperature range. The usefulness of nanohybrids for temperature measurement was confirmed additionally by measurements of repeatability (several cycles between 20 and 60 °C), and insensitivity to pH (range 4–9), ionic strength, presence of biomolecules as well as photostability was confirmed under exposure to the Xe lamp (500 W, 150 min). Cytotoxicity was also tested for 293 T cells after 10 min lasting incubation and low toxicity of nanohybrids was observed. Cells were imaged at different temperatures using a confocal fluorescence microscope and two emission channels were observed: 415–544 and 580–620 nm. With the temperature increase, a decrease in the intensity of the red channel was observed, while the blue channel remained unchanged. Therefore, a change in the intensity ratio corresponding to the changes in temperature was observed, which proved that the nanohybrids described have the potential to image changes in the temperature of living cells.

Gold nanoclusters were utilized also by Wu *et al.*<sup>98</sup> in 2016 in dual-emitting probe. That material consisted of bovine serum albumin-stabilized gold nanoclusters (BSA-AuNCs) and fluorescein-5-sothiocyanate (FITC) therefore forming the sensor able to simultaneously measure pH and temperature. Its utility was tested in a living HeLa cell environment. The emission spectrum of this sensor exhibited two emission peaks at 525 (FITC) and 670 nm (AuNCs). The simultaneous temperature and pH measurement could be carried out due to the different quenching characteristics of these bands. The dependence of the emission intensity ratio on pH relied on the fact that the AuNCs emission was not changing, and the FITC emission was sensitive to pH changes. On the other hand, the ratiometric temperature measurement was possible due to the fact that the AuNC emission was strongly decreasing with temperature, whereas the FITC

emission could be used as a reference. Emission spectra as a function of temperature were measured at a constant pH (10 mM phosphate buffer at pH 9.0). The ratio of intensity 525/670 nm increased linearly for the temperature increase in the 1–71 °C range. The temperature accuracy in the 21–46 °C range was found to be 0.21–1.43 °C. After additional testing of the sensor response to variable pH at a constant temperature, the authors also used it for imaging HeLa cancer cells. For this purpose, the sensors were introduced into the cells by incubation at 37 °C for 1.5 h.

Another ratiometric sensor described in 2016 by Wu *et al.*<sup>99</sup> was based on rhodamine (Rhodamine B and Rhodamine 110) dye-incorporated Pluronic F-127-melamine-formaldehyde (MF) composite polymer nanoparticles (R-F127-MF NPs). The closure of the dyes in MF microspheres separated them from external conditions and allowed temperature measurements in a wide range. The optical measurement results for this sensor doped only with Rhodamine B showed a dependence of its properties on the concentration of the dye and confirmed the presence of homoresonant energy transfer (homo-RET) for higher concentrations. After the addition of the second reference dye (Rhodamine 110) in an optimized ratio of 1:400, a ratiometric temperature sensor R<sub>110</sub>-R<sub>B</sub>-F127-MF NP LTs was obtained. For the excitation line 488 nm, two peaks 520 nm (reference signal) and 582 nm (temperature dependent signal), assigned to the rhodamine 110 and rhodamine B, respectively, were observed. With the increase in the measurement temperature, an increase in the 520/580 nm intensity ratio was noted. In addition, the colloid stability and lack of dyes leakage was demonstrated even after the autoclave sterilization (121 °C, 103.4 kPa) and lyophilization (–80 °C, 1.3–13 Pa). Moreover, insensitivity to the changes in the parameters such as pH, ionic strength, and viscosity was also demonstrated. However, after the irradiation of the sensor with the 300 W high-pressure mercury lamp for 4 h, the intensity of the emission decreased to 80%, which indicated the occurrence of the photobleaching effect. Nevertheless, the ratio of the intensity of both dyes behaved uniformly for about 3 h. The LT was stable at very low and high temperatures and its operating range was found to be from –20 to 110 °C (and above, but this is the limit of the temperature controller used in the experiment, and heating in glycerol even up to 150 °C did not cause sensor degeneration). The authors determined relative sensitivity of their LTs to be equal to 4.9–15.4%/°C in the range 20–90 °C. The following measurements were performed in the living HeLa cells, into which the sensors were introduced by incubation for 4 h. It was shown that the calibration curve obtained in the cell environment did not differ significantly from the curve obtained outside the cells in PBS solution. After calibration, temperature measurements of the cells heated with microwaves were carried out (microwave therapy apparatus was used to generate microwave radiation and a planar spiral antenna was used for directionally heating the cell samples). Proportionality was found between heating efficiency and laser power—for a 40 W laser power and 250 s exposure time, a temperature increased from 28 to 46 °C (which is sufficient to cause cell death). Temperature changes were also monitored using a thermocouple thermometer and imaged using confocal microscopy after excitation with 20 mW argon-ion 488 nm laser. Observation of green and red channels showed a decrease in the intensity of the latter one as the temperature increased.

Fluorescent dyes were also incorporated in the genetically encoded ratiometric fluorescent temperature indicator (gTEMP)

proposed in 2017 by Nakano *et al.*<sup>100</sup> The authors examined several fluorescent proteins and chose two of them—one with the largest and the second one (as a reference) with the smallest fluorescence intensity change in response to temperature. After preliminary measurements, the authors chosen Sirius and mT-Sapphire dyes. Both fluorophores might be excited at around 360 nm and exhibited emission bands at 425 and 509 nm, respectively. An intensity ratio of 509/425 nm showed an increase in 210% in the range of 5–50 °C, so the change was 2.6%/°C. The insensitivity to the presence of  $K^+$ ,  $Mg^{2+}$ , and  $Ca^{2+}$  ions and to pH variations was also demonstrated. The fluorophores were linked with a *Thosea asigna* virus 2A peptide, to express equimolar amounts of Sirius and mT-Sapphire in HeLa cells (uniform expression in the cytoplasm and the nucleus). One of the most important advantages of using gTEMP was its fast, milliseconds response time. A 1 mW of 1462 nm heating laser irradiation induced a temperature increase in approximately 5 °C. Furthermore, after the addition of 10  $\mu$ M FCCP to the cells expressing gTEMP in the mitochondria, a temperature increase in about 6–9 °C was observed and imaged (Fig. 14). Great advantage of the gTEMP was the fact it located directly inside the mitochondria (mitochondria matrix), which enabled to visualize temperature distribution in the cell and a difference between the cytosol and the nucleus of 2.9 °C was found. In addition, the visualization of the *in vivo* temperature distribution was also performed by injecting mRNA of gTEMP into a fertilized medaka fish egg (at a single cell stage) and temperature changes were observed for 15 h without any toxic effects.

Because carbon dots (CDs) reveal relatively strong emission, photostability, biocompatibility, and insensitivity to the environmental changes, they act a good alternative to organic dyes, therefore, Wei *et al.*<sup>101</sup> proposed use of not only dyes but a combination of them both. The authors described ratiometric LT based on a Rhodamine B (RhB) covalently bonded (with amino reactive group isothiocyanate) to carbon dots (CDs). The independence of the CDs luminescence on the presence of salts,  $H_2O_2$  and  $ClO^-$  was confirmed. In addition, cytotoxicity studies were performed in living HeLa cells and the biocompatibility of the sensor was demonstrated. The influence of the temperature on the optical response of the sensor in the solution was tested. At excitation with a 405 nm laser line, two emission bands, 482 and 586 nm, attributed to the CDs and the RhB emission, respectively,

were observed. When changing the temperature from 5 to 50 °C, a decrease in the intensity of the RhB emission was observed, while the emission of the CDs remained almost unchanged. The intensity ratio of these 586/482 nm bands decreased linearly with the temperature. After the confirmation of the biocompatibility of the sensor, the imaging of HeLa live cells was performed. Endocytosis without additional reagents after incubation for 4 h allowed to observe the probes inside the cells, however, no high efficiency of this process was noted. Therefore, their surface was modified using a peptide that aided their introduction into cells (human immunodeficiency virus transacting activator of transcription peptide), which allowed to observe an increased fluorescence of the sensor from the cells. To visualize the temperature in the HeLa cells, the luminescence of the two channels: blue 450–510 and red 550–610 nm (bandpass filters were used) was observed. When the cells reached 5 °C after the storage for 1 h in the refrigerator, the intensity of the red channel was increased, while the blue channel remained almost unchanged from the observation performed at 37 °C. By analyzing the signals and determining the ratio of the intensity of the channels, a temperature distribution was also measured in the individual cells, which was consistent with the set temperature.

In 2017, a DNA nanomachine acting as a ratiometric LT for temperature measurements in living cells was described by Xie *et al.*<sup>102</sup> This LT was of tetrahedron shape and one of its edges was made of a temperature-sensitive molecular beacon (MB) that could shrink or stretch under temperature changes. Below a certain characteristic temperature, the MB was forming a closed structure folded into a loop, so the two faces of the tetrahedron joined by the MB were close to each other. Above this temperature, the DNA tetrahedron became expansive because the MB was unfolding and straightening. The prepared DNA machine was resistant to the nuclease degradation and could be introduced into the cells without additional reagents. To obtain a sensor with ratiometric luminescent properties, two dyes, FAM and TAMRA, which acted as the donor and acceptor, respectively, in the FRET process, were attached to the two moving tips of the tetrahedron. Therefore, by changing the temperature, the distance between the dyes could be modified, which enabled the FRET (red emission) at low temperature and prevented it (green emission) at high temperature. This made the ratio of the emission intensity of the acceptor to

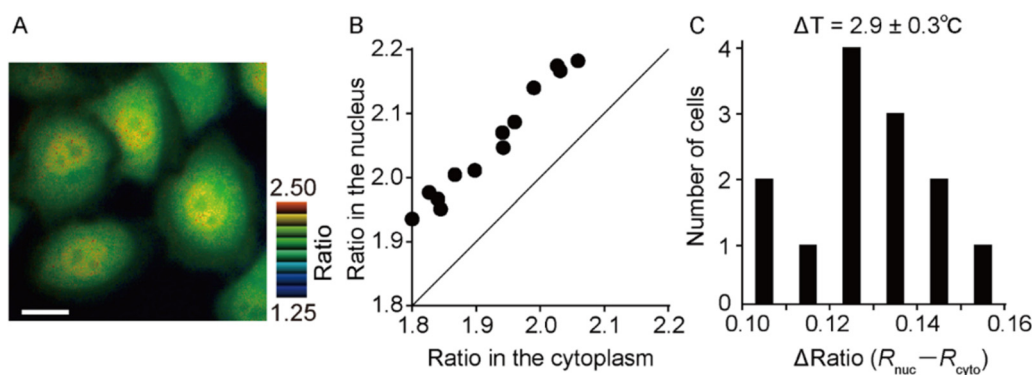


**FIG. 14.** Genetically encoded ratiometric fluorescent temperature indicator (gTEMP) (a) A pseudocolor map of the gTEMP emission intensity ratio in HeLa cells. (b) Ratio graph in the cytoplasm and nucleus in each of the HeLa cells (13 cells). (c) Histogram of the temperature differences between the ratios in the cytoplasm and in the nucleus.<sup>100</sup> Reprinted with permission from Nakano *et al.*, PLoS ONE 12, 1 (2017). Copyright 2017 Authors, licensed under a Creative Commons Attribution (CC BY) License.

the donor a parameter dependent on the temperature. Measurements of fluorescence as a function of temperature showed a gradual decrease in this intensity ratio along with the temperature increase. The temperature range of the measurement covered 27–50 °C, because the temperature above 55 °C could be destructive for this structure. A significant relative sensitivity of 5.2%/°C for the range of 30–50 °C and a good thermal resolution of less than 0.5 °C were determined. Moreover, the stability of this sensor was demonstrated for 50 cycles of temperature changes between 27 and 54 °C. The independence of the sensor on the environmental agents such as the presence of  $K^+$  ions (100, 150, 200 mM) and pH changes (6.0, 7.4, 8.0) was also tested, confirming the sensor insensitivity to factors other than temperature changes. The noncytotoxicity and resistance to nuclease degradation have also been demonstrated. Then, the sensor was introduced into live HeLa cells by 3 h incubation at 37 °C. Thermal imaging of the cells was performed using a confocal microscope and a heating stage under 488 nm laser excitation, and the changes in the FRET signal were observed at various temperatures. While the emission in the green channel increased for temperature rising from 25 to 40 °C, the red channel intensity decreased significantly. The calibration curve of the intensities ratio was acquired on the basis of the averaged value obtained from at least three cells (five measuring points: 25, 29, 33, 37 and 40 °C). Moreover, measurements and imaging of the photothermal effect in living cells were also carried out. For this purpose, gold nanowires (AuNRs) were additionally added to the cells (by subsequent incubation for 3 h). Using an NIR 980 nm laser with a power of 650 mW, a temperature increase by 15 °C was recorded after 30 min of exposure.

A ratiometric thermometer based on the DNA chain was also proposed by Wu *et al.* in 2017.<sup>103</sup> It consisted of a fluorescent short single-stranded DNA (ssDNA) with attached FAM donor and TAMRA acceptor and its working mode was based on FRET. This DNA chain was characterized by strongly temperature-dependent conformational changes. As the temperature decreased, the distance between the donor and acceptor was also reduced, and the shape of the chain changed from elongate to globular. Such shape changes of the DNA-based nanostructures with the temperature changes affected the FRET efficiency and the intensity of each of the emission bands. Due to this, the intensity ratio of the donor and acceptor signals (D/A) were used to determine the temperature. The nanothermometer was introduced into PC-3 cells (human prostate cancer cell line) using the

cubosome nanoparticles and the emission signals in cells were measured during heating on the heating stage. The experiment showed that in the temperature range of 20–50 °C, the LIR changed linearly, allowing to maintain almost constant, high sensitivity of 7.04%/°C in this temperature range. Laser scanning confocal microscopy images showing the emission intensity ratio D/A at different temperatures are presented in Fig. 15. As can be seen, the ratiometric LT based on the FRET in a fluorescent short single-stranded DNA enabled thermal mapping based on the fluorescence spectra of the used phosphors.

The advantages of this material included high biocompatibility and stability in various environments, the invariable response in several heating and cooling cycles, constancy of sensory properties regardless of the nanoparticles concentration or excitation power. However, the problem is that the donor emits 520 nm and the acceptor at 580 nm, so the emission can be disturbed by light absorption or scattering in cells, therefore before *in vivo* application, the optimization of the phosphors to emit in the red or nearinfrared range was a challenge. The luminescence intensity ratio of two bands was used for *in vivo* thermal imaging for the first time in 2015. Multifunctional  $Nd^{3+}$ :LaF<sub>3</sub> fluorescent nanoparticles with a high  $Nd^{3+}$  ions concentration, capable of *in vivo* photothermal heating, luminescence tumor localization and intratumoral temperature determination were proposed by Carrasco *et al.*<sup>81,104</sup> By optimization of  $Nd^{3+}$  ions concentration, the balance between heating capacity and IR luminescence could be obtained. By selecting a sufficiently high concentration and excitation with a beam of 808 nm (4 W/cm<sup>2</sup>), the simultaneous heating and luminescence in the spectral range of the optical transparency window was achieved. As shown in Fig. 16(a) the luminescence intensity ratio of two spectrally close localized emission bands at 865 and 885 nm of  $Nd^{3+}$ :LaF<sub>3</sub> NPs was analyzed as a temperature dependent parameter. Unluckily, the close spectral vicinity of these bands strongly hindered the temperature readout. However, the authors showed that in the biological temperature range, the  $I_{R1}/I_{R2}$  (865/885 nm) ratio revealed a linear dependence on the temperature [Fig. 16(b)]. It was shown [Fig. 16(c)] that the value of the relative sensitivity, which reached 0.25%/°C was only slightly dependent on the type of media used (such as aqueous media, powders, and different types of tissues).

In order to verify the usefulness of the nanoparticles for *in vivo* applications, the tests were carried out, confirming the lack of their toxicity and stability (Z-potential of LaF<sub>3</sub> nanoparticles: 5.6%  $Nd^{3+}$  was –23.7 mV). Human breast cancer cells were injected into a mouse

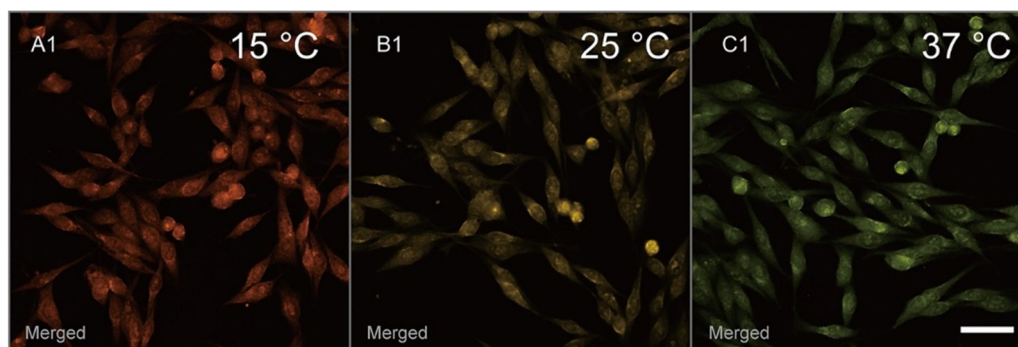


**FIG. 15.** Laser scanning confocal microscopy images of the L-FAM-12R1-TAMRA FT transfected PC-3 cells at varied temperatures.<sup>103</sup> Reprinted with permission from Wu *et al.*, ACS Appl. Mater. Interfaces 9, 11073–11081 (2017). Copyright 2017 American Chemical Society.

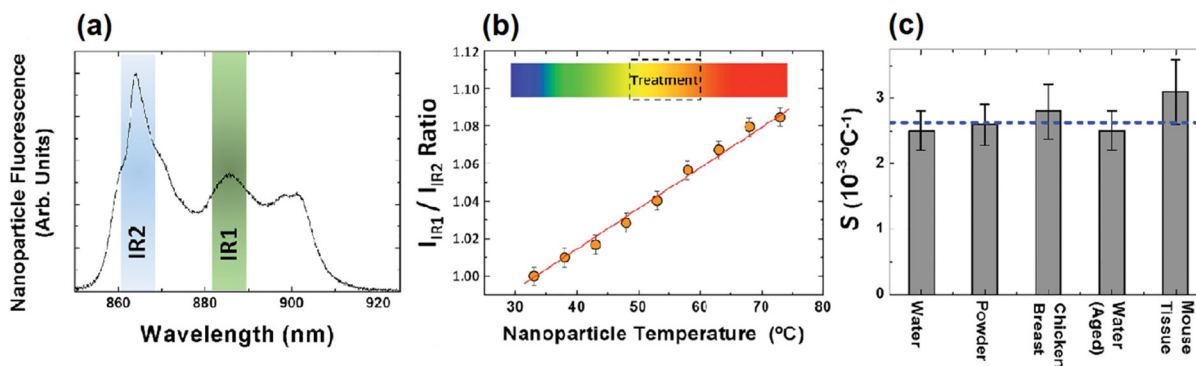


**FIG. 16.** Room temperature emission spectra of  $\text{LaF}_3$ : (a) 5.6% $\text{Nd}^{3+}$  NPs in the near infrared range with schematically indicated two spectral ranges used for thermal sensing; (b) temperature dependence of the  $I_{\text{IR1}}/I_{\text{IR2}}$  intensity ratio; and (c) thermal sensitivities of  $\text{Nd}^{3+}:\text{LaF}_3$  nanoparticles obtained in different environments. The dashed line indicates an averaged estimated value for the thermal sensitivity.<sup>104</sup> Reprinted with permission from Carrasco *et al.*, *Adv. Funct. Mater.* **25**, 615–626 (2015). Copyright 2015 John Wiley and Sons.

(one tumor on both sides) and about two weeks after the injection, when it reached  $9 \text{ mm}^3$  in size, photothermal therapy was initiated. The  $\text{LaF}_3:5.6\%\text{Nd}^{3+}$  nanoparticles dispersed in PBS at a concentration of 10% tumor weight (which is about  $7 \times 10^{13}$  nanoparticles per tumor) were introduced into the area of one tumor, while the other tumor served as a reference [Fig. 17(a)]. The infrared luminescence images of the mouse, which confirm the ability of these NPs to subcutaneous luminescence imaging are presented in Fig. 17(b). As can be seen in Fig. 17(c), the thermal images verify the capability of  $\text{LaF}_3:5.6\%\text{Nd}^{3+}$  NPs to generate heat. Simultaneously with the intratumoral temperature measurements, the surface temperature of the skin was estimated as a function of the irradiation time during 4 min-long therapy [Fig. 17(d)]. During the whole cycle, the temperature inside the tumor was c.a. 20% higher than the surface temperature. This was explained by a decrease in temperature as a result of heat exchange between the tissue and the air, which did not occur in the case of heat diffusion within tissues volume. As can be seen in Fig. 17(d), a similar trend as a function of time was also manifested by the changes in the temperature of a control tumor that has undergone the same exposure procedure. The temperature increase as a result of the residual tissue absorption still existed, but it was less than 50% of the heating induced by  $\text{Nd}^{3+}:\text{LaF}_3$  NP in the tumor subjected to photothermal therapy.

A positive result of  $\text{LaF}_3:\text{Nd}^{3+}$  NPs and 808 nm laser therapy, after which the tumor post-treatment size decreased, was presented. After 20 days of therapy only a scar on the skin was observed, while control tumors steadily increased during this time. In order to check the possible accumulation of NPs in the body after the therapy, the *ex vivo* tests were also carried out. Mice after 20 days of the treatment were euthanized and then several organs were removed and the luminescence under 808 nm excitation was examined. The presence of nanoparticles was noted in the scar and spleen, suggesting that the nanoparticles could partially leave the tumor area and enter the bloodstream, and eventually (after 20 days) get and become partially deposited in other organs of the body.

Other multifunctional nanoparticles designed for thermal imaging based on the emission intensity ratio were also analyzed by Zhu *et al.*<sup>105</sup> For this purpose, an upconverting, slightly elongated core-shell structure, additionally covered with a carbon layer— $\text{NaLuF}_4:\text{Yb}^{3+}, \text{Er}^{3+}$  at  $\text{NaLuF}_4$  at Carbon (csUCNP at C) was proposed. The undoped

$\text{NaLuF}_4$  layer (thickness 7.5 nm) between the carbon coat and the  $\text{NaLuF}_4:\text{Yb}, \text{Er}$  core, was improving the upconverted luminescence (UCL) and prevented luminescence quenching by the carbon shell (without this insulating layer, the 83% weakening of the UCL

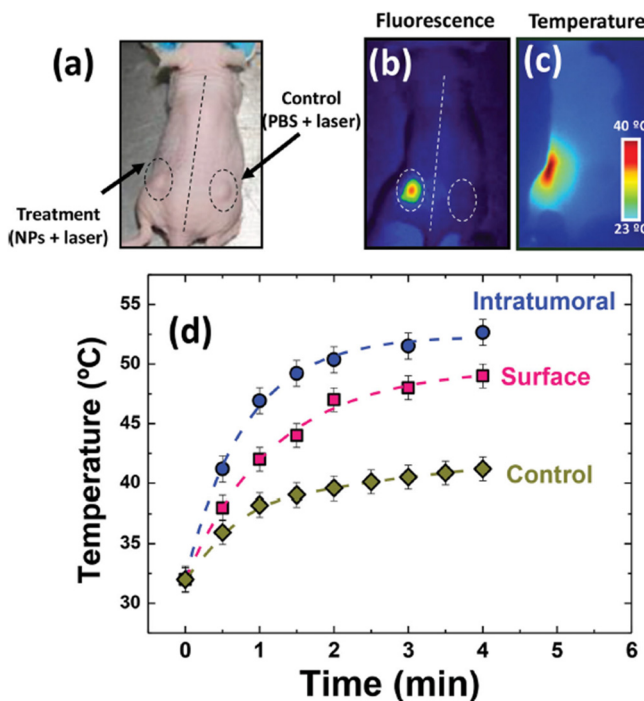


**FIG. 17.** Optical image of a representative mouse with two tumors. A solution of  $\text{Nd}^{3+}:\text{LaF}_3$  NPs was injected only in the left-side tumor whereas the right-side one was used as a reference (a). Infrared luminescence images of the mouse under 808 nm ( $4 \text{ W/cm}^2$ ) laser irradiation (b) thermal of the same mouse under the same irradiation conditions (c). Time evolution of the temperature at the tumor surface as obtained from the analysis of infrared thermal images and of intratumoral temperature obtained from the analysis of sub-tissue luminescence (d).<sup>104</sup> Reprinted with permission from Carrasco *et al.*, *Adv. Funct. Mater.* **25**, 615–626 (2015). Copyright 2015 John Wiley and Sons.

intensity was noted). Two excitation sources were used in the experiment, where the fiber-coupled 730 nm laser diode was used to excite a carbonate coat and CW 980 nm wavelength was employed to the  $\text{NaLuF}_4:\text{Yb}^{3+},\text{Er}^{3+}$  core excitation. After 730 nm excitation of a  $1\text{ W/cm}^2$  power density, the light to heat conversion occurred with an efficiency of  $\eta = 38.1\%$ . Additional experiments confirmed a lack of chemical toxicity and the heat generation of csUCNP at C able to cause the tumor cells death without excessive heating of the environment and without injuring healthy cells around. In order to determine the temperature based on the luminescence spectra, the  $525\text{ nm } (^2\text{H}_{11/2} \rightarrow ^4\text{I}_{15/2})/545\text{ nm } (^2\text{S}_{3/2} \rightarrow ^4\text{I}_{15/2})$  intensity ratio was analyzed upon 980 nm continuous wave excitation of  $50\text{ mW/cm}^2$  power density. In the temperature range of  $35\text{--}40^\circ\text{C}$ , the obtained sensitivity of this thermometer reached  $1\%/^\circ\text{C}$ . Therefore, the thermal imaging with  $0.5^\circ\text{C}$  thermal resolution and  $0.9\text{ }\mu\text{m}$  spatial resolution was achieved. The goal of the authors was to optimize the radiation dose needed for the photothermal *in vivo* therapy using a microscopic temperature measurement system that differs from the macroscopic approach. The external temperature was analyzed using a thermal imaging camera, whereas the actual temperature in the area of csUCNP at C nanoparticles after 730 nm excitation was determined by means of their emission spectra. The measurements were made for two power densities:  $0.8\text{ W/cm}^2$ , which led to overheating, and  $0.3\text{ W/cm}^2$  causing a subtle, but sufficient to cause hyperthermia, temperature increase in nanoparticles. HeLa cells (107 cells) were incubated with csUCNP at C ( $4.4\text{ pg}$  per cell) and then implanted in mice to grow the tumor. Infrared thermal images of mice with and without tumor HeLa cells with attached csUCNP at C during irradiation with a beam of 730 nm collected using an thermovising camera have shown. One can note the elevated overall temperature of the control mouse, whereas a mouse with nanoparticles showed increased temperature only in the area of the cancer. The tumor in each of the examined mice was irradiated with a 730 nm beam every day and after 5 days it shrank until complete disappearance with no relapse and regrowth. Such mice after 40 days of treatment were still alive, whereas in control animals (either no treatment, or mice exposed to 730 nm beam but without nanoparticles or mice injected with nanoparticles, but with no laser irradiation) a continuous increase in tumor size and ultimately the death of the mice after about 22 days was noted.

Unfortunately, this promising approach, had also several disadvantages. The system used two different wavelengths to simultaneously excite luminescence and generate heat, which not only complicated the experimental setup, but also caused some thermal reading uncertainty, because the penetration depths of both excitation wavelengths in the irradiated tissue were not equal. Moreover, the carbon layer could also absorb the 980 nm excitation line and radiation emitted by the core of the nanoparticle. In addition, the bands used to determine the temperature were spectrally close to each other, which could generate a problem related to filters and spectral resolution, which also limited the usefulness of this method.

The aim of the study of Miyagawa was to visualize the thermal changes of the muscle of *Dicronorrhina Derbyana* beetle during its work.<sup>106</sup> For this purpose luminescent nanoparticles were embedded in the ultrathin, elastic and simple polymer nanosheets with a large contact surface, high adhesion and a small thermal capacity. A nanopolymer on which two separated layers were deposited, was created. The first layer was formed by highly temperature-dependent EuDT

and the other one by less temperature sensitive Rhodamine 800 dye. Owing to the confinement of EuDT and Rhodamine in two separated nanosheets, the energy transfer between them was negligible. The system was equipped with two excitation wavelengths: 405 and 640 nm, and the temperature was determined based on the EuDT emission intensity ratio at 620 nm compared to 700 nm emission from Rhodamine. The emission intensity of EuDT-NS decreased practically linearly with the increasing temperature, whereas the intensity of the Rho-NS was almost temperature independent. The sensitivity to temperature changes in EuDT originated from the fact that the energy transfer rate between Eu (III) and the ligand molecule ( $\beta$ -diketonate) was varying depending on the temperature. It is worth pointing out, that due to the absorption (640 nm) and emission (700 nm) by Rhodamine 800 in the red visible range and strong emission of EuDT, the contribution of autofluorescence was relatively small.

Two experiments were carried out: imaging of the thermal changes after the “external” heating with a 980 nm beam generated by vibrations of water molecules (analyzed in the  $29\text{--}45^\circ\text{C}$  temperature range) and the thermal changes caused by the work of dorsal muscles of the main flight muscle of *Dicronorrhina Derbyana*. In the studies of the temperature changes caused by the muscle work, the heat production was observed in the so-called “preflight preparation” or “escape mode,” when the flight muscles were activated and warmed up. Such a mode was induced by a mechanical stimulation, e.g., by gently touching the legs of the beetle with a stick. When the beetle was not stimulated, the muscles underwent a natural cooling process. Several beetle stimulation cycles were performed and the result of one of them is visible in Fig. 18. In the second image, the temperature distribution due to the activation and warming up of the muscles after the stimulation of the beetle for the preflight preparation was noted. The last view shows the temperature of the muscle during rest, and thus the natural cooling of the muscle. The change of the muscle temperature during such a cycle was also filmed. At  $37^\circ\text{C}$ , a very high relative temperature sensitivity  $S = 5.26\%/^\circ\text{C}$  was obtained, and as the size of the analyzed area was reduced, the temperature resolution was increased but the maximal value was around  $0.75^\circ\text{C}$ . Unfortunately, this method only allowed surface imaging.

In order to eliminate numerous experimental obstacles, Wu *et al.* optimized the phosphors used in the fluorescent short single-stranded DNA (ssDNA) based nanothermometer for *in vivo* imaging applications.<sup>103</sup> To eliminate the problem of the absorption and scattering of FAM and TAMRA phosphors on cells, an ROX donor and ATTO 647N acceptor were used to shift the emission bands toward infrared direction (donor 610 nm, acceptor 665 nm). The ability to modulate the emission characteristics by choosing the appropriate phosphors between which FRET occurs, so that their emission maxima appear at a desirable spectral range is an undeniable advantage of such a thermometer. The usefulness of L-ROX-12R1-ATTO for an *in vivo* application has been demonstrated in mice. The  $5 \times 10^6$  PC-3 cells (prostate cancer) were injected subcutaneously (3.5 mm in depth) into both legs of the mouse and an imaging experiment was performed 24 days after the injection. Additionally, the DNA L-ROX-12R1-ATTO structure was injected only into the right leg and after 5 min from the injection, the mouse was exposed to 40 W microwave radiation to heat the tumor. Figure 19 showed the distribution of the emission changes of each of the phosphors before [situation (a) and (b)] and after [(c) and (d)] irradiation. As the temperature increased, the



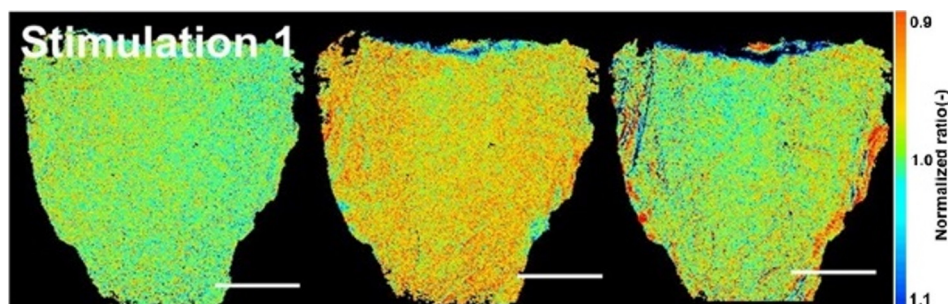


FIG. 18. Temperature mapping of dorsal longitudinal muscle during preflight preparation of *Diconorrhina derbyana* using stacked nanosheets. Stimulation was conducted three times and the normalized ratio [based on the temperature of infrared telescope (IRT) at 25 °C] changed against temperature change in three-time preflight preparations. (scale bar: 1 mm).<sup>106</sup> Reprinted with permission from Miyagawa *et al.*, ACS Appl. Mater. Interfaces **8**, 33377 (2016). Copyright 2016 ACS Publications.

emission intensity of the acceptor decreased significantly, while the intensity of the donor emission increased only slightly. Therefore, an increase in the D/A ratio with the temperature was observed in the area of the biological temperatures (20–50 °C).

However, in the work, the temperature distribution is not clearly shown, and only the distribution of the changes in the emission intensity of each phosphor separately is registered. Information on the harmful effects of the experiment and the survival of mice was also not provided. In an attempt to overcome the lack of information on the temperature inside a small animal, Ximendes *et al.* have made use of core-shell NPs doped with erbium, thulium, and ytterbium ions (specifically, Er-Yb at Tm-Yb LaF<sub>3</sub> NPs).<sup>107</sup> Such nanostructures presented thermal sensitivities as large as 4%/°C when monitoring the intensity ratio between the emitted intensity of Yb<sup>3+</sup> ions at 1000 nm (<sup>2</sup>F<sub>57/2</sub> → <sup>2</sup>F<sub>75/2</sub>) and that of Tm<sup>3+</sup> ions at around 1230 nm (<sup>3</sup>H<sub>5</sub> → <sup>3</sup>H<sub>6</sub>). The combination of a high sensitivity with the concurrent emissions in BW-II and BW-III suggested a great potential for such nanostructures in terms of high-contrast *in vivo* thermal imaging. For this reason, the authors elaborated an experiment in which they were able to see the temperature variations in a small animal model. The experiment consisted of subcutaneously injecting the NPs into a CD1 mouse and inducing a heating cycle on its tissues. Hence, by the luminescence generated by the NPs, the inference of temperature could be

straightforwardly determined. Figures 20(a) and 20(b) include the *in vivo* ratiometric thermal images obtained at different time delays during a heating transient and thermal relaxation, respectively. Though, in light of the thermal dependence of the optical properties of biological tissues,<sup>66,108</sup> the absolute values of the temperature scale are questionable, the analysis of the data were able to provide a reasonably coherent value for the thermal diffusivity, *D*, of the tissue.

To demonstrate the effects of thermal imaging in a living organism, one of the requirements was the use of a water-soluble nanothermometer. Chen *et al.* accomplished this task using the iridium (III) complexes attached to a thermally sensitive, water-soluble polymer backbone PNNPAM, was applied as the thermometer.<sup>109</sup> The dispersibility of this material in water and the solubility of such a polymer solution changed, what was related to the existence or breaking of hydrogen bonds between polymeric amide bonds and water molecules. With the temperature increase, the hydrogen bonds were broken, the water molecules were released. Therefore, the hydrophobic interactions started to play a bigger role, which led to partial aggregation (formation of micelles), decreased polarity of the iridium complexes and increased stiffness. Such a change in the polymer conformation from longitudinal to globular strongly affected the emission intensity and lifetime of the excited state of the iridium complex in this material, which allowed the creation of two types of thermometers for *in vivo* applications

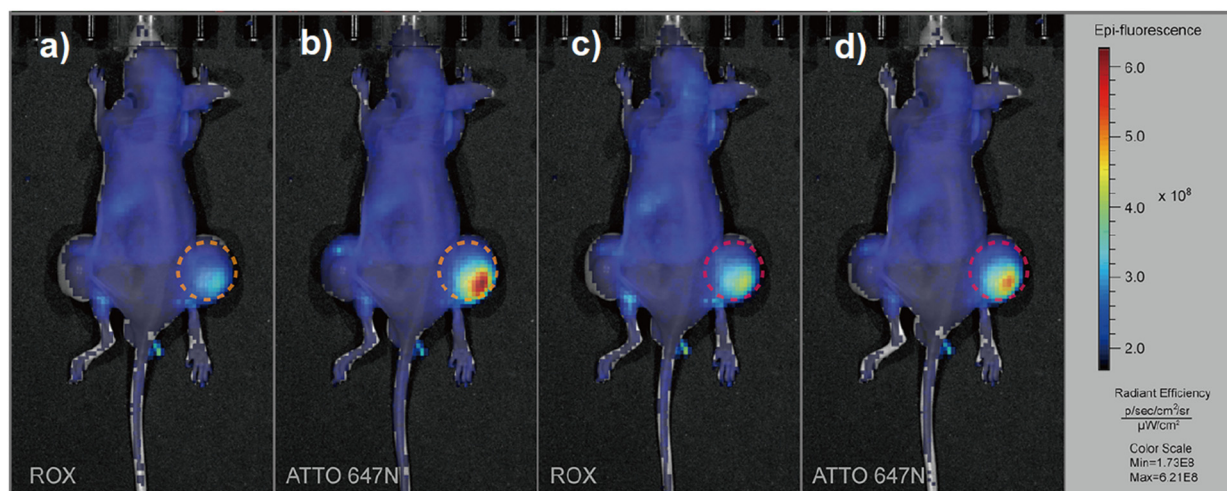
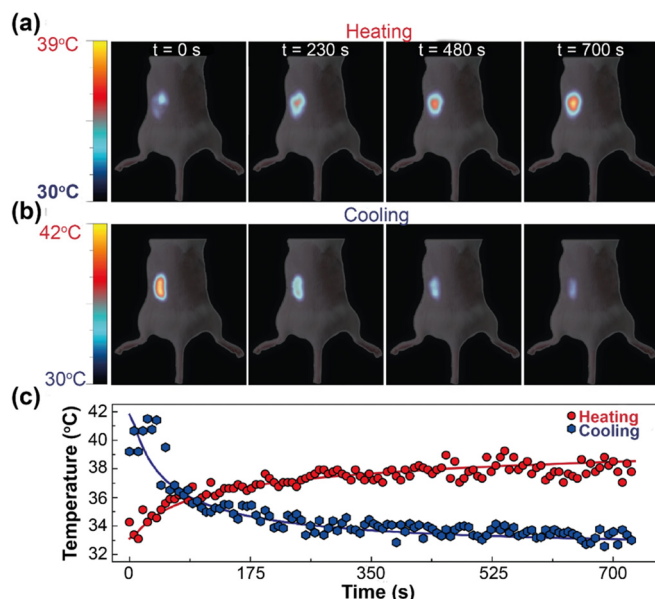


FIG. 19. Fluorescence images of the L-ROX-12R1-ATTO LT injected tumor tissues before [(a) and (b)] and after [(c) and (d)] microwave irradiation.<sup>103</sup> Reprinted with permission from Wu *et al.*, ACS Appl. Mater. Interfaces **9**, 11073–11081 (2017). Copyright 2017 American Chemical Society.



**FIG. 20.** Thermal images obtained by dividing the luminescence images at 1000 and 1200 nm during heating (a) and relaxation (b) processes. An optical figure of the anesthetized mouse was superimposed. (c) Time evolution of the average temperature of the injection area as measured by the subcutaneous LNTHs during heating and thermal relaxation processes. Reproduced and reprinted with permission for Ximendes *et al.*, *Adv. Funct. Mater.* **27**, 1 (2017). Copyright 2017 John Wiley and Sons.<sup>107</sup>

operating in the 16–40 °C temperature range: the thermometer based on the emission intensity ratio of red (570–620 nm) to green (460–510 nm) channels of iridium complexes and luminescence imaging with time resolution, which will be described later in this article (Sec. IV G). The studies were carried out in the zebrafish larva, which is widely used in research related to cancer, diabetes and genetic

cardiovascular diseases, as it is 87% identical at the genetic level to humans. As can be seen in the confocal laser scanning microscopy images shown in Fig. 21, after excitation with a 405 nm beam of 100  $\mu$ W power the luminescence was distributed in the whole of a zebrafish larva, also in the yolk sac and belly. Both the luminescence intensities of green and red channels exhibited only trifling increase with the elevation of temperatures from 22 °C to 28 °C and due to this fact, the luminescence intensity ratio of the green to red channel did not reveal any obvious increase when the temperature increased, which may be related to the effect of the intense autofluorescence.

Similar *in vivo* studies in zebrafish were also carried out using an acrylamide-based polymer thermometer with  $\text{Ir}^{3+}$  and  $\text{Eu}^{3+}$  compounds.<sup>110</sup> In this material, the thermosensitive unit was NIPAM while APTMA was used to improve cellular uptake and water solubility. Owing to the energy transfer, the  $\text{Ir}^{3+}$  compounds effectively performed the role of a sensitizer and easily expanded the excitation of the  $\text{Eu}^{3+}$  complex to the visible region (in the polymer without  $\text{Ir}^{3+}$  it was impossible to directly excite  $\text{Eu}^{3+}$ ). Upon 405 nm excitation in the temperature range of 20–42 °C (*in vivo* 25–30 °C), with the temperature rise, the increase in intensity of the band in the spectral range of 460–540 nm (related to iridium) was observed, and the intensity of  $\text{Eu}^{3+}$  peaks in the range of 580–630 nm remained unchangeable. Changes in emission intensity were explained in terms of the thermal changes in the polarity of the microenvironment. At low temperatures (below the lower critical), the PNIPAM polymer, due to the hydrogen bonds between the amide groups of the polymer and the surrounding water molecules, was well soluble in water, resulting in a small hydrodynamic radius (about 10 nm at 20 °C). With the rise of the temperature, as a result of the thermal motions of the molecules, these bonds weakened, the solubility in water decreased, and the hydrodynamic radius increased (up to 107 nm at 30 °C). The hydrophobic interactions within P- $\text{Ir}^{3+}$ - $\text{Eu}^{3+}$  began to play a more important role and led to such a chain arrangement that the water molecules were pushed out, whereby the polarity of the microenvironment around the  $\text{Ir}^{3+}$  complexes decreased causing the enhancement of the  $\text{Ir}^{3+}$

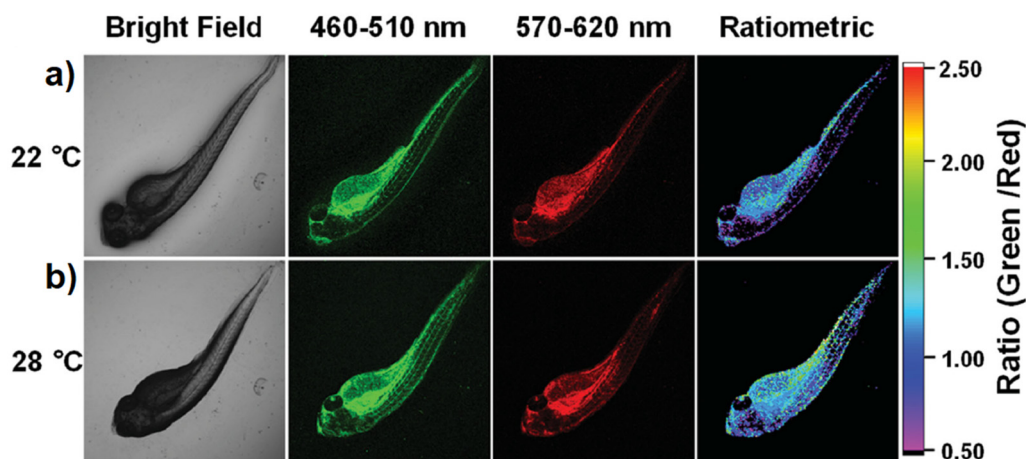


**FIG. 21.** Bright images and confocal laser scanning microscopy images of living zebrafish larva after injection of thermometer at 22 °C (a) and 28 °C (b). The green and red channels presented separately and the ratiometric luminescence images obtained from the green to red channel.<sup>109</sup> Reprinted with permission from Chen *et al.*, *Adv. Funct. Mater.* **26**, 4386 (2016). Copyright 2016 John Wiley and Sons.

luminescence intensity. Thus, after increasing the temperature from 20 to 42 °C, the hydrophilic polymer backbone transformed into a hydrophobic type, which resulted in a decrease in the microenvironment polarity. Then, the change in polarity led to a change in the complexity of the  $\text{Ir}^{3+}$ , as well as the intensity of the phosphorescence and the lifetime of the emission. It is worth noting that these processes were fully reversible. A water P- $\text{Ir}^{3+}$ - $\text{Eu}^{3+}$  was injected into the heart of a zebrafish. After 2 h from the injection, the luminescent signal was collected from the heart area, and after 12 h the polymer was found throughout the whole body confirming good biocompatibility. The temperature was determined based on the intensity ratio of  $\text{Ir}^{3+}$  (470 nm) to  $\text{Eu}^{3+}$  (615 nm). The influence of other factors on LIR was examined and this parameter was shown to be practically independent of the ionic strength (aqueous KCl,  $\text{CaCl}_2$  and  $\text{MgCl}_2$ ), pH (6–8) and polymer concentration (from 0.06 to 1.2 mg/mL). What is more, it revealed low cytotoxicity even for high polymer concentrations (0.8 mg/L). However, the autofluorescence had a strong impact and the differences in the ratio of the green channel (460–540 nm) to the red one (580–630 nm) as a function of temperature were not clear and obvious, as shown in Fig. 22.

An important requirement for imaging living organisms is the high photostability of the thermal sensor. Therefore, another dual-emission ratiometric luminescent nanothermometer based on (Eu at SiNPs) has been proposed where the intensity ratio of blue emission of silicon nanoparticles (455 nm) and red emission of  $\text{Eu}^{3+}$  ions (620 nm red emission) were considered as a temperature dependent parameter.<sup>111</sup> The insignificant toxicity was noted for these nanoparticles as well as high photostability (over many cycles of heating/cooling and UV irradiation over 45 min time period) in living cells. The intensity measured in the blue channel in 430–480 nm range decreased linearly when the temperature increased from 25 to 70 °C. Contrastingly, the red channel intensity was found to be temperature independent. The

change of their luminescence intensity ratio was as high as 4.5%/°C in the 25–70 °C temperature range (relative sensitivity calculated from the digitalized plot: from 1.5–4.5%/°C). Moreover, the Eu at SiNPs were found to have lysosome-targeting property. The heating and cooling process between 30 and 45 °C was also investigated and simultaneously cells in both channels were imaged. The same calibration curve for both cooling and heating was recorded which was consistent with the set temperatures for the cells.

#### D. Relative emission band(s) intensities under double excitation

The most reliable methods to image temperature in 2D are believed to be based on the relative measurements, which are expected to take into account and correct for non-homogenous illumination (if only the fluorescent reporters respond in a linear way) or non-homogenous distribution of the temperature reporters (unless aggregates are formed). However, these methods are less reliable, when two spectrally different excitation lines and emission bands are used. The issues originate from the fact that the spectral properties of the tissues or samples (such as light scattering  $\mu_s$  and direction  $g$ , absorption  $\mu_a$  coefficients) are strongly dependent on the wavelength, spectral range and spectral shift between the wavelengths used. Moreover, in the most complicated case, the fact that two images have to be collected, makes the temperature imaging system either fast but costly (when two cameras are used for simultaneous recording of images in two spectral windows) or cost-efficient but slow (when a single camera is used with switchable filters).

The relative emission band intensities under double excitation are solving some of the issues mentioned above. Using single emission band intensity is as cost-effective and technically as simple as intensity based temperature determination. However, the reliability is improved

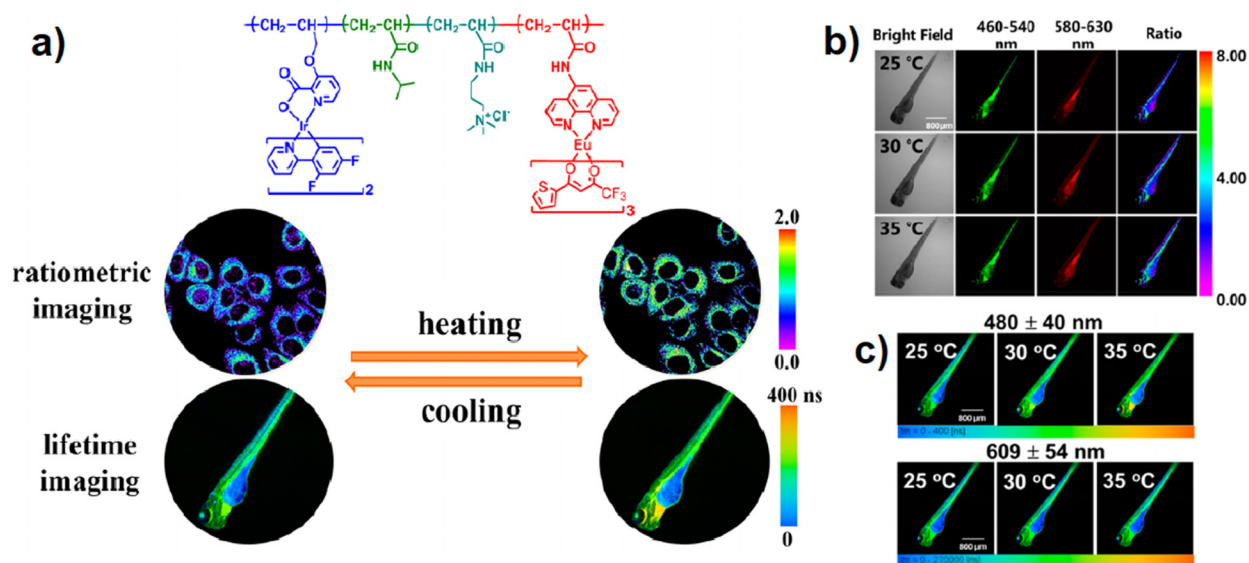


**FIG. 22.** The P- $\text{Ir}^{3+}$ - $\text{Eu}^{3+}$  based temperature imaging in zebrafish larva. (a) the P- $\text{Ir}^{3+}$ - $\text{Eu}^{3+}$  compound and the principle of ratiometric and luminescence lifetime T imaging. (b) Bright images and confocal laser scanning fluorescence (green and red channels and their ratio) microscopy images of living zebrafish larva after injection of thermometer at 25, 30, and 35 °C. (c) The phosphorescence lifetime imaging microscopy (PLIM) images of zebrafish larva at 25, 30, and 35 °C.<sup>110</sup> Reprinted with permission from Zhang *et al.*, ACS Appl. Mater. Interfaces **10**, 17542–17550 (2018). Copyright 2018 American Chemical Society.

by collecting two images which form a ratio. In contrast to another popular technique, which exploits two emission bands under single excitation line (Fig. 2, Sec. IV C), the method presented here sustains ratiometric imaging, but may offer faster frame rate, because it is technically simple and affordable to all-electronically switch between two LED or semiconductor laser sources, in order to record two images by the same optical setup—i.e., the same filter set with single camera.

To define thermometric parameter using the relative intensity of single emission band intensity  $I_B(T, \lambda_{exc})$  under two excitation lines ( $\lambda_{exc}^n$ ,  $n = 1, 2$ ) is relatively simple, when sample autofluorescence  $A$  is absent (i.e., due to anti-Stokes emission or negligible intensity)

$$\Theta(T) = C \cdot \frac{I_B(T, \lambda_{exc}^1)}{I_B(T, \lambda_{exc}^2)} = C \frac{I_{LT}(T, \lambda_{exc}^1) + A(\lambda_{exc}^1)}{I_{LT}(T, \lambda_{exc}^2) + A(\lambda_{exc}^2)} \sim \frac{I_{LT}(T, \lambda_{exc}^1)}{I_{LT}(T, \lambda_{exc}^2)}. \quad (17)$$

If the relative changeover the studied temperature range is constant, e.g.,  $S_R = 0.5\%/^{\circ}\text{C}$ , knowing initial temperature  $T_0$  and assuming homogenous excitation illumination and nonmoving objects, one may determine spatial temperature maps as

$$T(x, y) = T_0(x, y) + C \frac{I_{LT}(T, \lambda_{exc}^1)}{I_{LT}(T, \lambda_{exc}^2)} \cdot \frac{1}{S_R}. \quad (18)$$

Again, because the initial temperature map is actually difficult to know before the experiment, the temperature rise in respect to the starting point can be only found, in response to some stimulus (e.g., drug, toxicant, local heating, etc.), that is, the relative temperature change that can be quantified

$$\delta T(x, y) = \frac{I_{LT}(T, \lambda_{exc}^1)}{I_{LT}(T, \lambda_{exc}^2)} \cdot \frac{1}{S_R}. \quad (19)$$

However, this is an oversimplification. As shown recently, simple division of the two images does not provide good temperature maps, and to be useful, reference images have to be subtracted prior to division,<sup>112</sup> e.g.,

$$\Theta(x, y, T) = C \cdot \frac{I_{LT}(T, \lambda_{exc}^1) + I_{LT}(T_0, \lambda_{exc}^1)}{I_{LT}(T, \lambda_{exc}^2) + I_{LT}(T_0, \lambda_{exc}^2)} \cdot \frac{1}{S_R}. \quad (20)$$

Then, the calibration of such function over temperature shall enable to derive actual absolute temperature. An examples of the thermal imaging taking advantage from this approach was demonstrated on a non-invasive genetically encoded tsGFP cell temperature sensor, consisting

of a green fluorescent protein (GFP) and a TlpA thermosensitive protein.<sup>113</sup> The coiled-coil TlpA protein was undergoing conformational changes under the influence of temperature at around  $37^{\circ}\text{C}$ . It was a reversible structural transformation from a parallel coiled-coil dimer to unfolded monomers. These temperature-dependent conformational changes of TlpA were passed to the attached GFPs, under the influence of two excitation peaks of GFP at 400 nm (neutral, phenolic form) and at 480 nm (anionic, phenolate form) which changed their mutual intensity. An excitation ratio of 400 nm to 480 nm for emission at 510 nm was a measurable parameter informing about the temperature of the medium. It is important to note that unfused GFPs showed a smaller change in the 400/480 nm excitation ratio than tsGFP. Moreover, the authors created tsGFPs containing special sequences that allowed targeting selected organelles (plasma membrane, ER and mitochondria). They also showed the dependence of luminescent properties on the temperature, while their measuring ranges (and the temperature corresponding to the conformation change) differed slightly between the organelles, which the authors attributed to differences in temperature at different points in the cell (and not the presence of targeting sequences). What is more, the authors visualized the mitochondrial thermogenesis in HeLa cells after adding the CCCP reagent (Fig. 23). Confocal laser-scanning microscope imaging using the 405 nm line of a diode laser and the 488 nm line of an argon laser for excitation and a 505–525 nm bandpass filter for the emission of HeLa cells showed heterogeneity in the excitation ratio of 405/488 nm (although the sensor was evenly distributed in the mitochondria). However, a decrease in the ratio after the addition of CCCP was noted, which is equivalent to depicting the temperature increase in the mitochondrial areas. With the help of an additional dye JC-1 which reacts to the high potential of the mitochondrial membrane, a negative correlation with the excitation ratio 405/488 nm was shown, which suggested that the temperature was higher there, where the potential of the membrane was high. The authors also described the visualization of thermogenesis in brown adipocytes and in skeletal muscle myotubes.

The most recent optical thermometry *in vitro* imaging, where two different excitation lines (at 373 and 436 nm, for btfa- and DNPF-based micelles, respectively) and two different emission bands  $I_1$  (600–620 nm for  $\text{Sm}^{3+} \ ^4\text{G}_{5/2} \rightarrow \ ^6\text{H}_{9/2}$ ) and  $I_2$  (620–660 nm for  $\text{Eu}^{3+} \ ^5\text{D}_0 \rightarrow \ ^7\text{F}_2$ ), demonstrated maximal relative sensitivities of both samarium and europium temperature reporters to reach 1.5 and  $1.7\% \text{K}^{-1}$  for the btfa- and DNPF-containing micelles, respectively, both at 328 K. The corresponding minimum temperature uncertainty reached low value 6

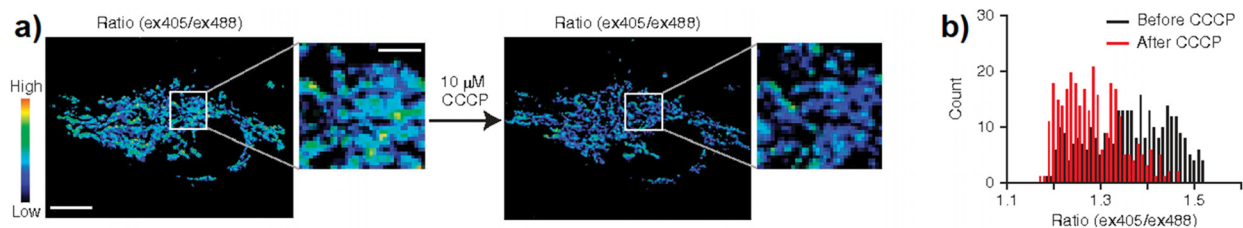


**FIG. 23.** The example of single emission band, two excitation wavelength ratiometric imaging of temperature (a) A pseudocolor map of the excitation ratio at 405 and 488 nm in HeLa cells with a mitochondrial temperature sensor tsGFP-mito before and after the addition of CCCP at  $37^{\circ}\text{C}$  (scale: 10  $\mu\text{m}$  on the larger and 3  $\mu\text{m}$  on the smaller image). (b) Histogram of the excitation ratio value of 405/488 nm excitation wavelengths.<sup>113</sup> Reprinted by permission from Kiyonaka *et al.*, *Nat. Methods* **10**(12), 1232–1238 (2013). Copyright 2013 Springer Nature.

mK (at 328 K) and 0.20 K (at 305 K). Although the demonstrated relative thermal sensitivity values were lower than that reported for similar micelles containing  $\text{Tb}^{3+}$  ions<sup>114</sup> ( $5.8\% \text{K}^{-1}$  at 296 K), the decrease in the relative uncertainty on the integrated intensity enabled to improve and get  $\delta I/I < 0.4\%$ , which is below 10 mK. The temperature maps were obtained by recording the wide field fluorescence images and simple division of the two color channels. These studies evidenced spots, where c.a. 5 K higher temperature was observed as compared to average temperature in the cells. This was explained by the intense RNA transcription activity of the nucleolus (Fig. 24).

### E. Relative emission intensity under two excitation bands

The concept of using relative emission intensity from two bands under two different excitation lines is a combination of the two methods described above. Actually, the advantages of those individual techniques are lost, because although switching excitation sources is simple and reliable (as in relative emission band intensities under double excitation, Sec. IV D), two emission bands have to be quantified (as in conventional ratiometric emission under single excitation line, Sec. IV E), bringing the same issues with either two cameras or tunable/switchable filters in front of the camera. Moreover, the spectral properties of the sample affect all four possible wavelengths (two excitations and two emissions) in a way, that is, difficult to predict and control, which definitely complicates calibration and temperature determination.

Relative emission intensity under two excitation bands was exploited by Homma *et al.*<sup>115</sup> in 2005 to measure the temperature changes of HeLa cells solution induced by a heating stage, as well as to visualize thermogenesis induced by the addition of FCCP in mitochondria. They described the new type of LT, Mito-RPT, designed to mark mitochondria (which was checked by mito-tracker green marker that was found in the same regions of the cell). This sensor consisted of two fluorescent dyes: Rhodamine B and CS NIR dye, whose excitation and emission lines were spectrally separated. Their emission intensities changed differently depending on the temperature (for Rhodamine B there was a decreasing relationship for temperature increase, whereas the CS NIR dye exhibited a constant intensity despite temperature changes), and due to this, the ratiometric measurement was possible ( $I_{\text{RhB}}/I_{\text{CS NIR}}$ ). The introduction of the sensor into the cells required 30 min incubation of the cells in a solution containing 1  $\mu\text{M}$  Mito-RPT. The authors showed that defocusing the lens or cell/organelle movement did not affect the temperature measurement carried out in this way, which was an important advantage of this measurement methodology. Regarding cell temperature measurement in a temperature-controlled solution, a non-linear dependence of the fluorescence intensity of each dye on temperature was observed (this was caused *inter alia* by a gradual defocusing along the z-axis during the measurement), however, their ratio maintained a linear characteristic. The slope of the curve obtained from the linear fit was found to be  $-2.72\%/\text{C}$ , whereas the temperature reading accuracy was estimated as 0.6  $^{\circ}\text{C}$ . The authors visualized the production of heat in the mitochondria after adding 10  $\mu\text{M}$  of FCCP to the cell solution. After the time necessary for the diffusion of the reagent into the mitochondria, the decline of the emission ratio of two dyes was noticeable, which was synonymous with the detection of heat production under the influence of chemical stimulation in HeLa cells (Fig. 25). Signals were collected in a circular region of interest (2–6 per one cell) of the

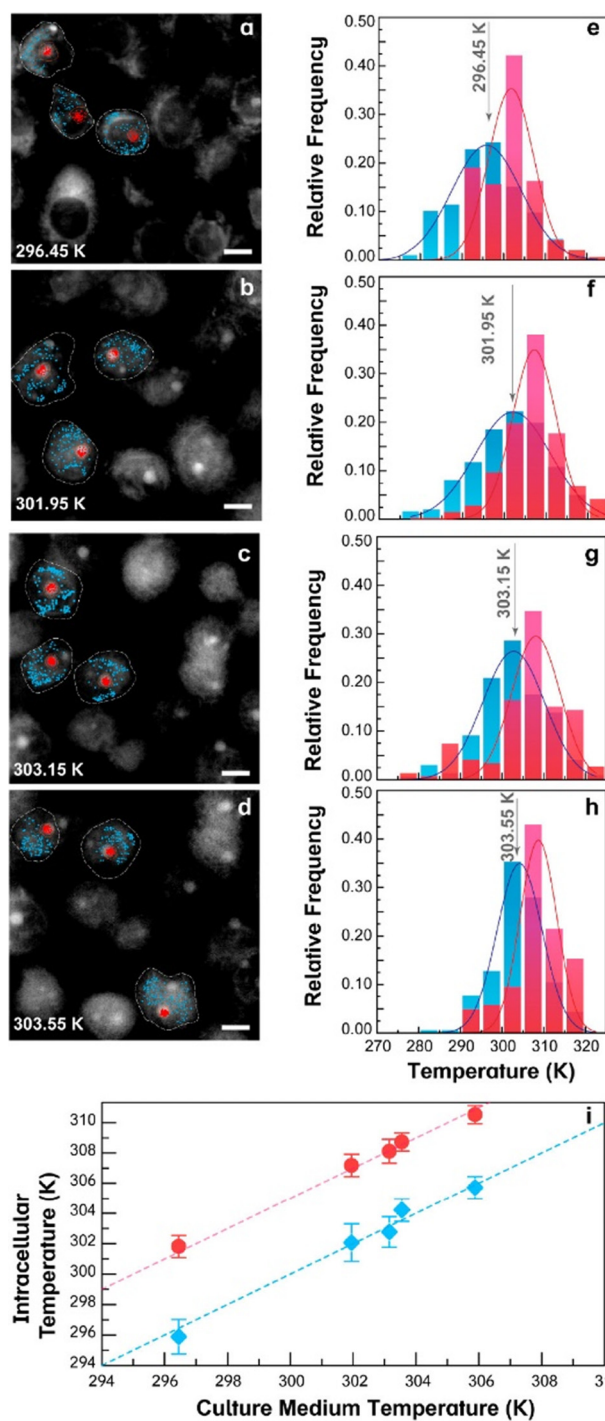
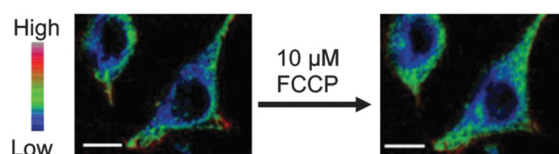


FIG. 24. Microscopy wide-field fluorescence images ( $\text{Eu}^{3+}$  emission channel) of the MDA-MB-468 cells incubated with DNPD-based polymeric micelles. Scale bar equals 10  $\mu\text{m}$ . The pink and blue histograms in (e)–(h) correspond to pink and blue regions in the cells [(a)–(d) correspondingly]. The hot spots are c.a. 5 K warmer than the surrounding cell temperatures, independently from the cell medium temperature (i).<sup>114</sup> Reprinted with permission from Piñol *et al.*, *Nano Lett.* **20**, 6466–6472 (2020). Copyright 2020 American Chemical Society.



**FIG. 25.** Example of two-excitation-two-emission band fluorescent thermometry using Rhodamine and CS NIR fluorophores. Map of the intensity ratio (Rhodamine B/CS NIR dye) in the mitochondria of HeLa cells before ( $t = -90$  s) and after ( $t = 330$  s) addition of  $10 \mu\text{M}$  FCCP; scale bar:  $10 \mu\text{m}$ .<sup>115</sup> Reproduced with permission from Homma *et al.*, Chem. Commun. **51**, 6194–6197 (2015). Copyright 2015 The Royal Society of Chemistry.

same size and shape for Rhodamine B and CS NIR dye. The intensities of the background were subtracted from the signal. The intensity ratio was calculated by division of Rhodamine B intensity by CS NIR dye intensity.

Another paper describing the ratiometric sensor with two excitation lines was presented by Xie *et al.*<sup>116</sup> in 2017. The authors desired to thermally visualize the cells of brown adipocytes (BA) and they used for this purpose two components, which were very similar due to their chemical structure, Rhodamine B methyl ester (RhB-ME) and Rhodamine 800 (Rh800). RhB-ME emission was quenched at higher temperatures, while Rh800 emission was insensitive to temperature changes. Both dyes had mitochondrial targeting properties because they were cationic dyes that could be distributed in the cell in response to a negative electrical potential, especially in the mitochondria. The imaging of the dyes in aqueous solution was performed using a confocal microscope with simultaneous excitation with 559 and 635 nm and collecting the fluorescence at 575–620 and 655–755 nm channels. The visualization of the HeLa cells showed that both dyes were located exactly in the same places (RhB-ME emission was observed in the red channel, Rh800 in the green channel). The ratio of the intensities allowed to observe the temperature distribution in the mitochondria of HeLa cell, with higher temperature inside (which is explained by the geometry of this cell). In order to further evaluate the thermometry, the described method was used to visualize thermogenesis of BA (cells were co-stained with the dyes for 1 h at  $33^\circ\text{C}$ ). Imaging of the temperature changes was carried out by studying the ratio of the intensity of Rh800 (green channel, excited at 635 nm,

collected at 655–755 nm) to RhB-ME (red channel, excited at 559 nm, collected at 575–620 nm) emissions. Thermal changes were caused by the addition of  $0.1 \mu\text{mol/l}$  NE or  $10 \mu\text{mol/l}$  carbonyl cyanide *m*-chlorophenylhydrazone (CCCP), however, in the second case the temperature increase was much higher.

## F. Spectral anisotropy

Some phosphors show different luminescent response when excited with light of different polarization, and sometimes such phenomenon is also temperature dependent. To take advantage of this fact in 2012 Donner *et al.*<sup>117</sup> utilized green fluorescent protein (GFP) under polarized light as a temperature nanosensor. When illuminated with polarized light, GFP molecules emitted partially polarized light and this phenomenon was strongly dependent on the random orientation of the molecular dipoles. An increase in the temperature resulted in an increase in the randomness of the orientation (due to Brownian motion) and thus the fluorescence polarization anisotropy (FPA) of GFP increased. The FPA depended, among others, on the fundamental anisotropy, fluorescence lifetime and the rotational correlation time, which depended on the hydrodynamic volume, viscosity and temperature. When the rotational Brownian motions were being too fast, the FPA equaled zero at each temperature, which is why the authors designed the described GFP with the appropriate hydrodynamic volume to meet the requirements regarding the possibility of observing the temperature-dependent FPA. The paper presented the thermal imaging of the transfected (this ensured even distribution of GFP inside the cells) HeLa cells both by means of emission intensity and by FPA of GFP [Figs. 26(a)–26(c)]. A calibration curve [Fig. 26(d)] was obtained for the dependence of FPA on the temperature in the intracellular environment by heating the whole sample chamber. It differed from the curve in PBS due to the different viscosity. The authors emphasized that the method using FPA was more correct than using GFP intensity, because in the case of FPA they received a homogeneous temperature distribution in transfected cells. This proved that FPA was not dependent on uneven GFP distribution in different organelles and that the intracellular viscosity for GFP molecules was homogeneous. The 473 nm beam of diode laser focused with two lenses (laser power in front of lenses: below  $1 \mu\text{W}$ ) was used to excite the GFP and the sample was scanned using a scanning mirror. The

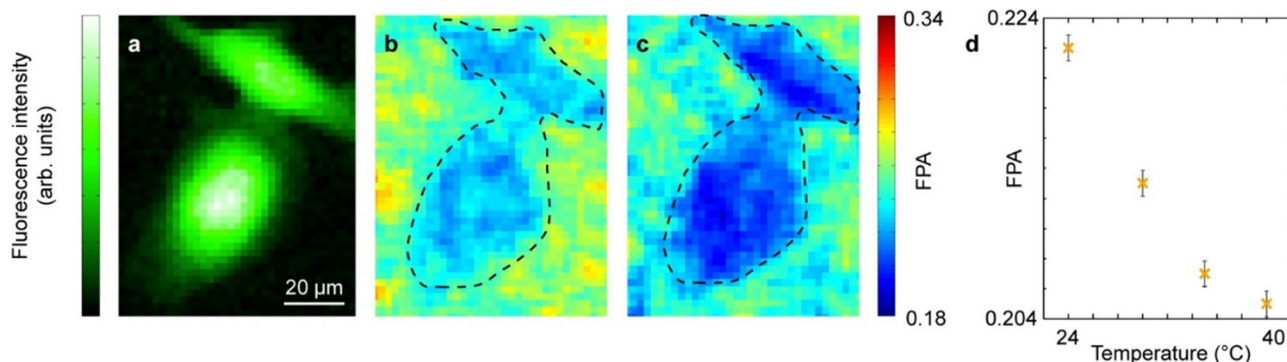


**FIG. 26.** Map of the intensity of the GFP excited with blue laser in transfected HeLa cells—(a); map of the FPA of the GFP in transfected HeLa cells at  $23^\circ\text{C}$ —(b) and at  $40^\circ\text{C}$ —(c); calibration curve for the temperature dependence of FPA—(d).<sup>117</sup> Reprinted with permission from Donner *et al.*, Nano Lett. **12**, 2107–2111 (2012). Copyright 2012 American Chemical Society.

collection time from one pixel was 20 ms. Another measurement was the thermal imaging of cells heated with gold nanorods dispersed in a cell solution and heated with an IR laser (its power was modulated). A temperature increase in about  $8^\circ\text{C}$  was observed for a laser power of 50 mW focused on a spot with a radius of  $1\ \mu\text{m}$  ( $\sim 1.6\ \text{MW}/\text{cm}^2$ ) at a distance of about 50 m from the cells tested.

The first work on *in vivo* thermal imaging using FPA technique was published in 2013.<sup>118</sup> In this case, the temperature in the nematode *Caenorhabditis elegans* (*C. elegans*) using green fluorescent protein (GFP) was determined. As it was shown by the *in vitro* studies, GFP constituted a reliable, fully controllable, robust and highly biocompatible luminescent probe<sup>119</sup> and its introduction into the body did not affect the cellular mechanisms. GFP could be bounded with selected enzymes found in only one cell type, for example in GABAergic neurons and thus serve to image selected target cells. The FPA was directly related to the rotational diffusion induced by a molecular Brownian motions. The rotational movements of the molecules were related to the temperature by means of the Debye–Stokes–Einstein equation, and as the temperature increased, the FPA decreased. As the FPA is the intensity ratio, the concentration of GFP used for imaging did not affect the measurement and the FPA was insensitive to fluctuations in the intensity of the excitation laser, photobleaching and sample migration.

Together with GFP, gold nanoparticles (GNR) were introduced into the nematode organism. GNR were responsible for raising the temperature inside *C. elegans* as a result of photoheating. As the experiment showed, the temperature increase was linearly dependent on the laser power density. In the experiment, two laser beams were used: the 800 nm wavelength from NIR laser enabled the excitation of gold nanoparticles, while the 473 nm blue laser beam was used for FPA imaging. FPA maps at different temperatures in the range of  $24\text{--}35^\circ\text{C}$  were obtained by means of the confocal scanning. The distribution of gold nanoparticles in the nematode digestive tract and GFP in neurons are presented in Fig. 27. The GFP image was obtained using two-photon fluorescence nonlinear microscopy. This allowed the imaging of thermal changes of individual neurons. The image of the neuron temperature distribution with the laser turned off was visible on the panel (b) while the panel (c) showed the temperature distribution obtained after switching the laser on. The temperature measured in one point, marked in part (c), as a function of time is visible on panel (d). A laser beam ( $63\ \text{kW}/\text{cm}^2$  power density) focused on gold nanocrystals inside the nematode was turned on after 20 s, which can be seen as the rise in the temperature depicted by a blue curve in Fig. 27, while the gray curve shows the result of a control experiment that took place in identical conditions, but for the reference *C. elegans* without gold nanoparticles. The use of GFP enabled imaging of small changes in temperature distribution and observed laser-induced temperature changes were almost  $3^\circ\text{C}$ . The reversibility of this process was confirmed by several heating and cooling cycles. However, this approach encounters several issues that exclude this method from a real application. First, the sensitivity depended on the medium to which GFP has been introduced ( $0.4^\circ\text{C}$  for those attached to GAD proteins located in cell bodies, axon branches and synapse regions in nematodes and  $0.1^\circ\text{C}$  in water) and proteins to which they were bounded, due to the different rotational time of different compounds. For another complex, new calibration curves have to be determined. Second, although the FPA did not depend on the GFP concentration, the photoheating

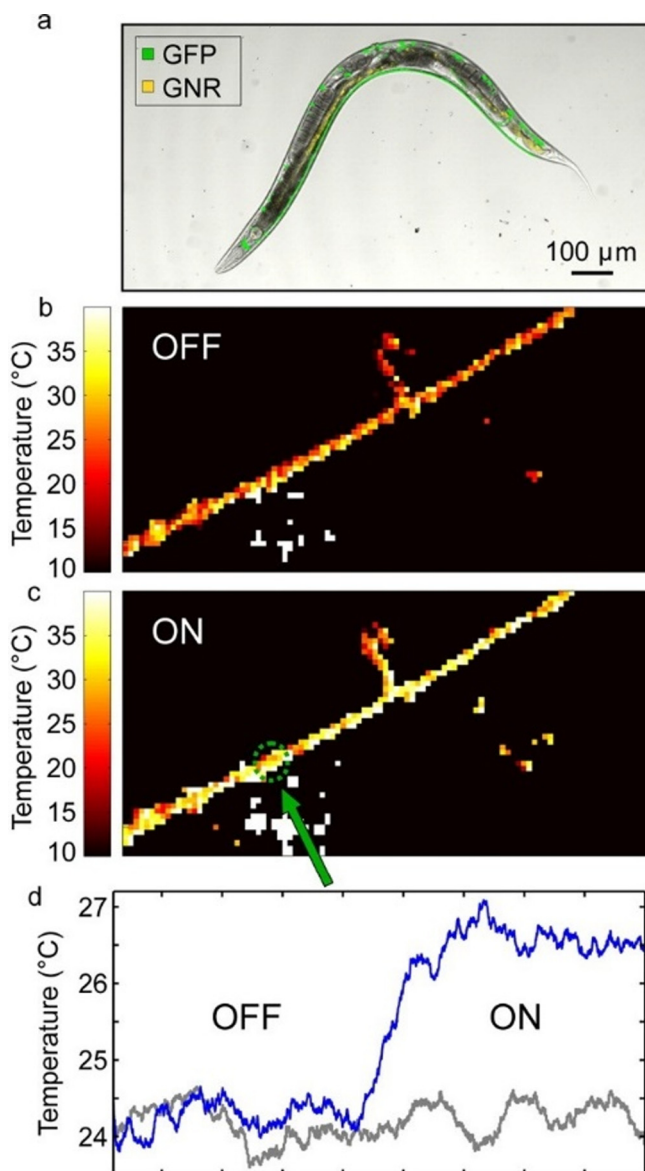


**FIG. 27.** The image of GFP luminescence intensity coming from the GABAergic neurons in *C. elegans* (marked as a green color) and the two-photon luminescence signal coming from GNRs in the digestive tract of nematode (marked yellow)—(a); temperature image of the neurons when the laser is off—(b); intracellular temperature measurements induced by internal heating generated via photothermal conversion of GNRs (when the laser is on)—(c) time dependent temperature measurement at one point marked with the green arrow. The blue curve shows the temperature change induced GNRs irradiated by laser, which was turned on at  $t = 20\ \text{s}$  ( $63\ \text{kW}/\text{cm}^2$ ), and the gray control curve performed on a nematode without GNRs under similar conditions—(d).<sup>118</sup> Reprinted with permission from Donner *et al.*, ACS Nano 7, 8666–8672 (2013). Copyright 2013 American Chemical Society.

effect depended on the concentration and distribution of the gold nanoparticles. Third, it was a green protein for which the depth of penetration can be disturbed by absorption and scattering on cells or by tissue components, thus a more appropriate solution could be red

proteins or their derivatives so that the spectrum of luminescence coincided with the biological window.

### G. Luminescence decays

The usage of the luminescence lifetimes for temperature mapping is conceptually straightforward and reliable, and stems from the fact most of the fluorophores demonstrate temperature dependent spectral and kinetic properties. The technique is relatively simple to implement, because the kinetics of a single emission  $\lambda_{\text{emi}}$  band is monitored in time after the single excitation wavelength pulse  $\lambda_{\text{exc}}$  and

$$\Theta(T) = \tau(T, \lambda_{\text{exc}}, \lambda_{\text{emi}}). \quad (21)$$

Thus, the imaging shall be directly related to the luminescence lifetime image

$$T = f^{-1}(\Theta) = f^{-1}(\tau). \quad (22)$$

Despite the conceptual simplicity of this method, the implementation is however hindered by the nature of the luminescence decay and some technical constrains. The simple Eq. (22) does not take into account the fact, that the luminescence lifetimes are often non-single exponents and that not only the temperature affects the spectral properties of the fluorescent sensors, but also the chemical environment such as viscosity or pH. Moreover, in many cases, especially given, e.g., energy transfer interactions, the decay becomes non-exponential, often accompanied by slow rise time and reliable determination of the lifetime becomes difficult. In that case, an agreement on the lifetime to be used has to be met, e.g., by calculating the average decay time that does not require explicit fitting, i.e.,

$$\langle \tau \rangle = \frac{\int_0^{\infty} I(t) \cdot t dt}{\int_0^{\infty} I(t) dt}. \quad (23)$$

Further, more simple, rapid lifetime determination algorithms exist, which integrate luminescence intensity in two or more time gated windows with variable delay after the pulse.<sup>120</sup> Frequency domain lifetime determination are also known,<sup>121</sup> but they are also not perfectly suited for multi-exponential decays. It is then possible to assess the statistical uncertainty of this luminescence decay value (by calculation of the second moment) and thus, indirectly assess the theoretically expected temperature uncertainty.

The other serious issue related to the fluorescence lifetime based temperature sensing with organic probes is the fact, their fluorescence lifetimes are similar to the lifetimes of other endogenous organic molecules (i.e., collagen, elastin, NADH, FAD, etc.), which requires careful interpretation of experimental results. In the case of substantial autofluorescence, the resulting low signal to background signal ratio is a serious issue, unless fluorescent probes are used with significantly longer (e.g.,  $\sim 150$  ns for InCuS<sub>2</sub> QDs, 0.3–0.6  $\mu$ s for iridium complexes, 1–1000  $\mu$ s for lanthanide chelates or Ln<sup>3+</sup> doped nanoparticles) luminescence lifetime. Second, the very short (orders of nanoseconds) luminescence lifetimes require very short excitation pulses. Sub-nanosecond pulses from laser diodes may be used, but such light sources, due to limited intensity, are suitable for raster scanned imaging, which, by its nature, makes the imaging rather slow. Whole field

lifetime imaging requires much larger energies to illuminate the whole field of view. In consequence, mode-locked femtosecond lasers are typically used, which significantly increase the costs of such experiments. Third, since the nanoseconds time scale kinetics has to be quantified, ultrasensitive imagers have to be used. Electron-multiplied CMOS scientific cameras are not sufficient for this purpose, and intensifier tubes or intensified cameras must be used which typically offers decreased optical resolution and again, rises the costs of the time gated technique. Although technically feasible and numerous algorithms exist that enable to convert experimental data to the lifetimes in a fast and reliable way, luminescence lifetimes are rarely used for temperature mapping.

Luminescence lifetime of lanthanide compounds (complexes, nanoparticles) are typically much longer than for organic fluorophores and quantum dots. This naturally means their luminescence lifetimes are easier to measure, but the intensities becomes compromised. Even though the photostability of such compounds are significantly higher, which enables accumulation of photons from many excitation pulses, the obvious cost is lower frame rate of the imaging. The alternative solution could be transition metal thermometers,<sup>122–124</sup> which show relatively long luminescence lifetimes (order of  $10^{-4}$ – $10^{-3}$  s) and brightness overpassing the lanthanide nanothermometers. These thermometers have not gained sufficient interest yet, and in addition to spectroscopic proof of the concept studies,<sup>125</sup> no practical *in vitro* T imaging demonstrations can be found in scientific literature.

Thermally induced changes in the luminescence decay curves were implemented to thermal imaging by Okabe *et al.*<sup>126</sup> who in 2012, showing the mapping of temperature distribution in living cells based on this approach. The authors created fluorescent polymeric thermometer (FTP) poly(NNPAM-*co*-SPA-*co*-DBD-AA) by optimizing the appropriate parameters (e.g., hydrodynamic size of 8.9 nm and in particular, selected units). Fluorescence lifetime was chosen as a temperature dependent parameter, because this approach eliminates errors resulting from heterogeneous FTP distribution in cells and different strength of the excitation of the FTP. The thermal dependence of the optical response resulted from the thermoresponsive properties of the selected polymer. At a low temperature, the poly-*N-n*-propylacrylamide (NNPAM) sequence assumed an extended structure and let in water molecules that were efficiently quenching the fluorescent DBD-AA unit. At high temperature, the emitter showed stronger luminescence, because the hydration decreased so the poly-NNPAM sequence shrank and the water molecules were pushed from the center (they no longer quenched DBD-AA unit). To obtain a calibration curve, the authors initially tested the FTP properties in the COS7 cell extract (to obtain the conditions as close as possible to the environment of living COS7 cells). As expected, an increase in the intensity of the FTP luminescence, and a prolongation of the fluorescence lifetimes during the heating of the extract was observed. The insensitivity to changes in ionic strength and pH in the range found in living cells was shown. Moreover the fluorescence lifetimes were proved to be insensitive to the differences in the FTP concentration, the presence of the proteins and viscosity. For the COS7 cells, a resolution of 0.18–0.58 °C (in the range of 29–39 °C) was obtained. The introduction of the FTP to live cells was achieved by means of the microinjection and the monitoring of the fluorescence (green) showed a good diffusion of the FTP throughout the cell. Having found the difference in the fluorescence intensity for the individual organelles, the authors decided to measure the luminescence lifetimes images (FLIM) in order to exclude the



effect of the FTP aggregation at specific locations in the cell. Using FLIM and the appropriate organelle markers, the temperature differences between the cytoplasm and some cell elements were noted [Figs. 28(a) and 28(b)]. Analysis of the data from many cells allowed to estimate the average temperature difference between the cytoplasm and the nucleus as  $0.96^\circ\text{C}$  [Fig. 28(c)] and it was shown that this difference was dependent on the cell cycle. In more than half of the examined cells, an additional warmer point (of about  $0.75^\circ\text{C}$ ) identified as centrosome [marked with arrows in Fig. 28(a)] was also noticed. Moreover, the production of heat by the mitochondria was shown. The red emission of MitoTracker Deep Red FM used in the experiment allowed to locate the mitochondria in the cell by luminescence measurements (Fig. 28). The FLIM image enabled to state that in these places the temperature is higher [arrows on the lower right

Fig. G-2(a)]. In addition, the increase in heat production by mitochondria after the addition of FCCP reagent (30 min after addition) has been shown and an increase in temperature of about  $1.02^\circ\text{C}$  has been noted [Fig. 28(e)]. Importantly, the additional measurement for the control polymer showed no change after the addition of FCCP [Fig. 28(f)]. Analogous measurements were conducted for HeLa cell line.

In 2013 Shang *et al.*<sup>127</sup> proposed to use gold nanoclusters (AuNCs) to measure the temperature at the cellular level using the dependence of the fluorescence lifetimes on the temperature. The fluorescent AuNCs have many convenient features, like a small size ( $<2\text{ nm}$ ), the stability of the colloid, simple synthesis and biocompatibility (no adverse effects to HeLa cells within 72 h after AuNCs exposure were found). During measurements of the AuNCs luminescence

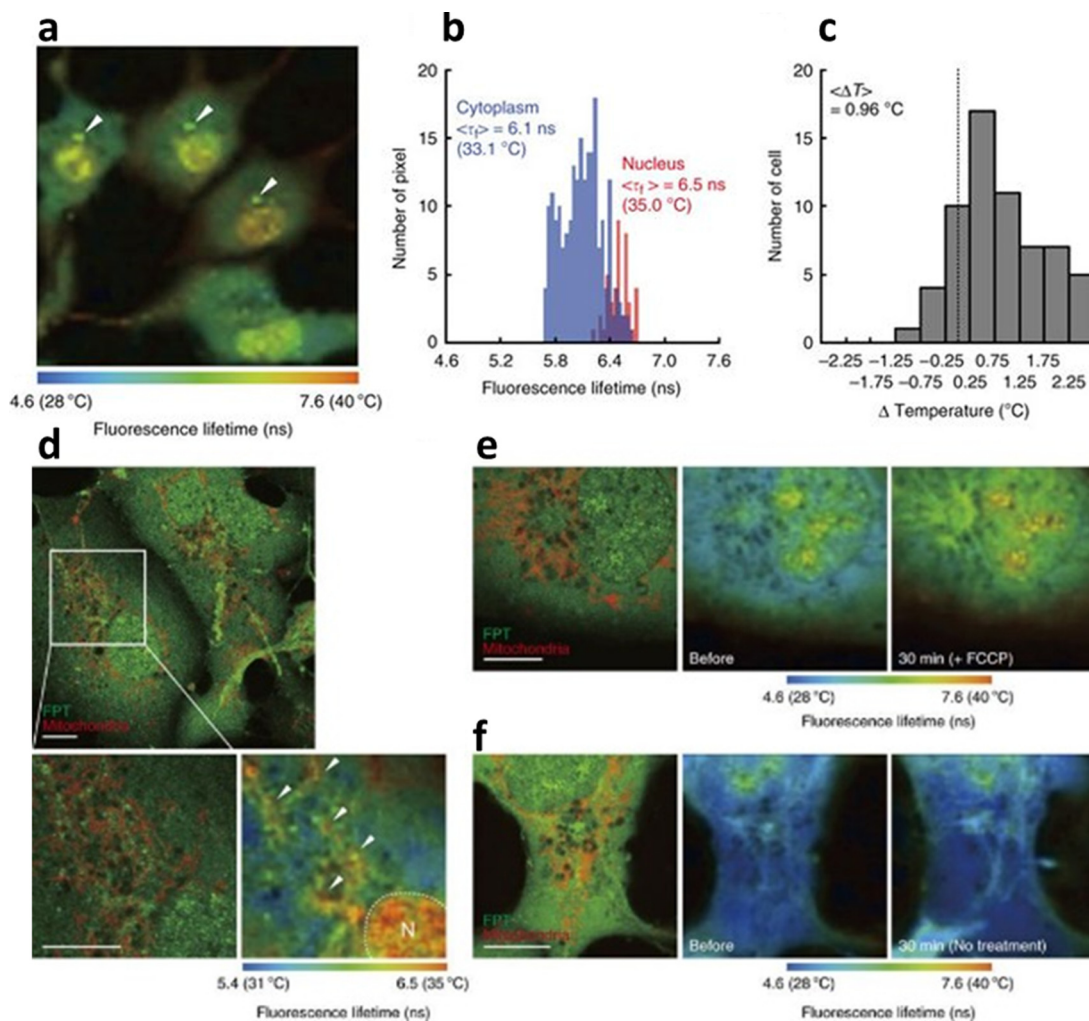


**FIG. 28.** Luminescence lifetime of as temperature reporter (a) fluorescence lifetime image of FPT in living COS7 cells. (b) Distribution of life times in the most left cell in figure (a)—in the cytoplasm and nucleus. (c) Histogram of temperature differences between the nucleus and the cytoplasm for 62 cells; (d) Confocal fluorescent images FPT (green) and MitoTracker Deep Red FM (red) in live cells COS7 and FLIM of FPT (right bottom panel). On the FLIM image, points of local heat production are marked with arrows, N indicates the nucleus. (e) Confocal fluorescence image of FPT (green) and MitoTracker Deep Red FM (red) and the temperature increase near the mitochondria after addition of FCCP presented in FLIM images. (f) Control experiment for (e)—no FCCP addition. Scale bar represents  $10\ \mu\text{m}$ .<sup>126</sup> Reproduced with permission from Okabe *et al.*, Nat. Commun. **3**, 705 (2012). Copyright 2012 Authors, licensed under a Creative Commons Attribution (CC BY) License.

properties in the PBS buffer, both a decrease in the emission intensity of the band at 700 nm (by 67% in the range of 10–45 °C, resolution 0.1–0.3 °C) and a shortening of lifetimes were noted for the temperature increase. At the same time, there was no spectral shift of the emission band. The luminescence decay times were fitted with the sum of three exponentials with components: short (24 ns), medium (130 ns) and long (600–750 ns), which turned out to be the most dependent on temperature. Then, after the 2 h lasting incubation at 37 °C the measurements in the live HeLa cells were carried out. FLIM imaging of HeLa cells at different temperatures was obtained using a home-made temperature-controlled sample stage (15 min waiting time after each temperature change). The lifetime maps were created by fitting the decay curve obtained from each pixel (Fig. 29). The increase in the temperature caused a significant shortening of the longest lifetime component, from 970 to 670 ns, in a range of 14–43 °C. The lifetimes of the AuNCs in cells were significantly extended compared to the results obtained in PBS, possibly due to the formation of a biomolecular layer around AuNCs in the cellular environment (also confirmed by measurements in the protein serum). The thermal resolution was estimated to be 0.3–0.5 °C in the investigated temperature range. The stability of the AuNCs response was tested for 2 h (excitation power 2.8 kW/cm<sup>2</sup>) and a change of <5% was obtained, also several cycles between 25 and 35 °C showed no major deviation. The AuNCs potential for the temperature difference analysis in the cells was then shown and in particular, designed heating table producing a temperature gradient was used for this purpose. The temperature profile for a single cell was obtained.

In 2015, Hayashi *et al.*<sup>93</sup> presented analogous studies on a new polymeric thermometer, which was spontaneously internalized by the cells. The authors' method of temperature measurement based on FLIM and fluorescent polymeric thermometer (FPT), which consisted of a thermosensitive (polyNNPAM) unit, an ionic unit (SPA) and a water-sensitive fluorescent unit (DBD-AA). The analogous mechanism as in their previous publication<sup>126</sup> was responsible for the dependence of the emission intensity and the lifetimes of the DBD-AA unit

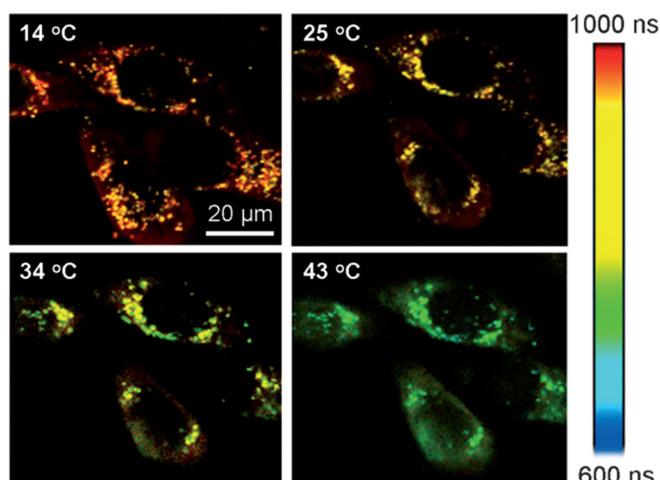


**FIG. 29.** FLIM images of HeLa cells with AuNCs nanosensors at different temperatures.<sup>127</sup> Reprinted with permission from Shang *et al.*, *Angew. Chem. Int. Ed.* **52**, 11154 (2013). Copyright 2013 John Wiley and Sons.

on the temperature. The increase and decrease in the temperature caused the closing and opening of the polymer structure, respectively. At the same time, the emission was quenched or enhanced by the presence or absence of water molecules inside the polymeric structure. Thus, this FPT exhibited stronger fluorescence and longer luminescence lifetimes for increasing temperature (temperature resolutions, calculated based on the fluorescence lifetime, were 0.05 to 0.54 °C within the range from 28 to 38 °C). Most importantly, after 10 min incubation of HeLa cells with an FTP solution (0.05 w/v% FTP in 5 w/v% glucose in water) at 25 °C, spontaneous internalization of FTP by HeLa cells was observed. FLIM images were taken using a pulsed excitation line of a TCS-SP5 confocal laser-scanning microscope equipped with a 405 laser. To obtain a photon count rate lower than 2% of pulse count rate ( $2 \times 10^7$ ) the laser power, pinhole size and detector sensitivity were carefully controlled. Fluorescence decay curves were fitted with double-exponent in each pixel using SPCImage software (after the binning procedure). FLIM performed at living HeLa cells showed that at higher temperatures of the medium, the lifetimes of the fluorescence were longer. In the next step, the temperature of the medium was maintained at 30 °C and the higher temperature (extended lifetimes of FTP luminescence) of the nucleus was observed than of the cytoplasm for single cells. After the examination of many cells, the average difference of 0.98 °C was found. The heat production near mitochondria, whose positions were found using a mitochondrial indicator MitoTracker Deep Red FM was also detected [arrows in Fig. 30(a)]. It was also confirmed that the heat production within mitochondria was increased by the addition of the CCCP reagent. Indeed, longer fluorescent lifetimes were obtained after the addition of the reagent [Fig. 30(b)] that corresponded to the temperature increase by  $1.57 \pm 1.41$  °C. The use of another control DMSO reagent that did not have such properties, did not initiate any change in the heat production in the mitochondria. Additional authentication of this FTP was obtained by performing temperature mapping also in other cell lines: NIH/3T3 (mouse fibroblast-like cell line) and COS7 (African green monkey fibroblast-like kidney cell line expressing SV40 T-antigen).

Another challenge was the relatively long time of measurements using the FLIM methodology, which was overcome in 2016 by Itoh *et al.*<sup>128</sup> Traditionally, raster scanned time-domain FLIM provides a high spatial resolution, but to acquire the whole image the long time is needed. The authors decided to compare both, the time-domain and the frequency-domain FLIM method, which significantly reduced the time of image creation (up to 10 s per frame), unfortunately at the expense of resolution. The endoplasmic reticulum (ER) targeted fluorescence thermometer ER thermo yellow as well as cytosolic mCherry sensor were used in this study. ER thermo yellow was internalized by the living cells after incubation for 30 min in 250 nM ER thermo yellow containing 0.025% DMSO in DMEM-HEPES at 37 °C, 5% CO<sub>2</sub>. Time-domain FLIM showed that the fluorescence lifetime was shorter at higher temperatures (2.50 and 2.28 ns at 25 and 37 °C, respectively). Fluorescence decay curves were fitted with double-exponents. Corresponding measurements were carried out using frequency-domain FLIM and the linear relationship (range: 23–40 °C) between temperature and the average lifetime was obtained with the sensitivity of  $-26$  ps/°C (accuracy of 1.6 °C). Moreover, using this sensor and frequency-domain FLIM, an expected increase in temperature by 0.93 °C was observed after stimulation of HeLa cells with ionomycin.

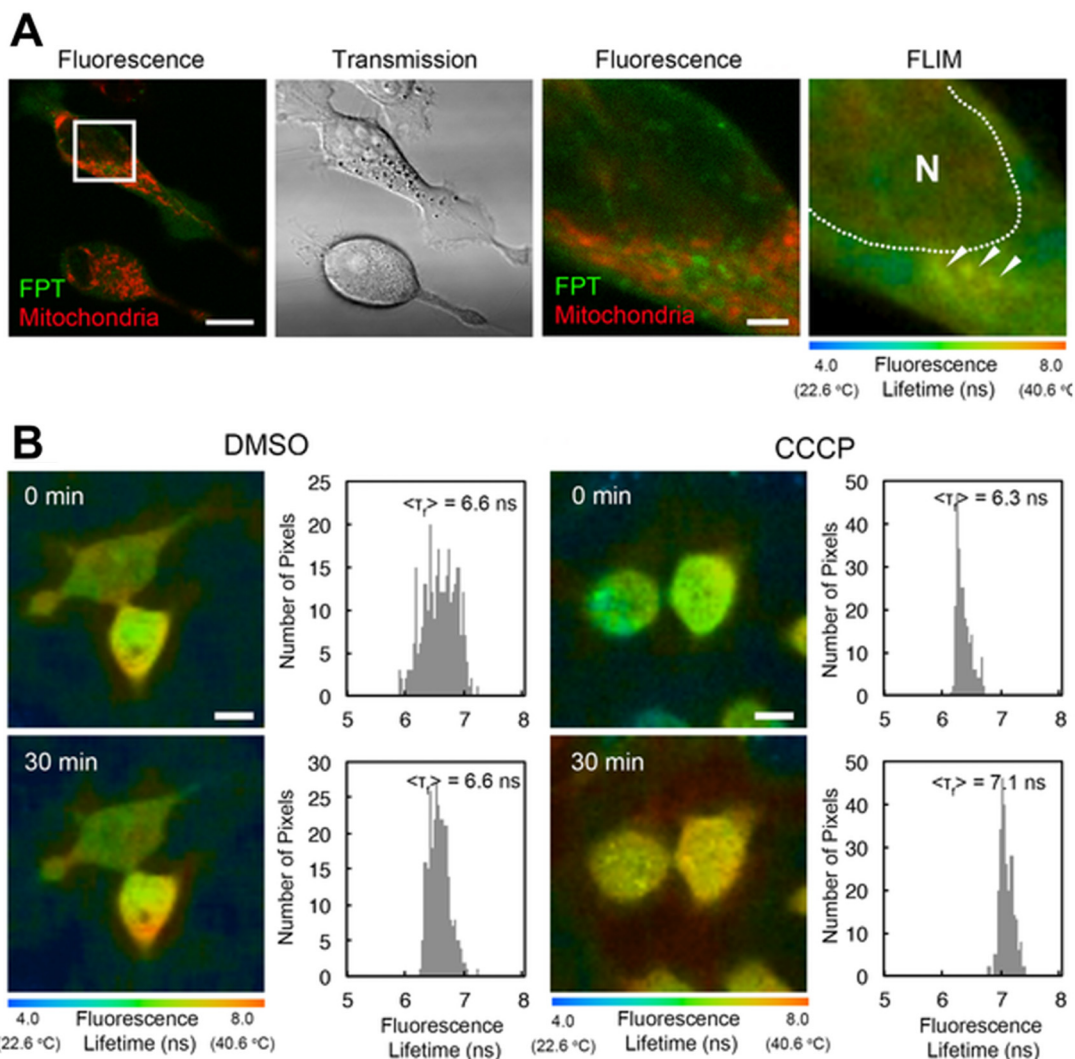


**FIG. 30.** Temperature imaging using fluorescence lifetimes of organic fluorescent molecules (a) confocal fluorescence images of the FPT (green) and MitoTracker Deep Red FM (red) in living HeLa cells at 30 °C; Transmitted light image; FLIM image, points of local heat production are marked with arrows, N indicates the nucleus. (b) FLIM image changes after addition of DMSO or CCCP; histograms of the fluorescence lifetime of cells in the field of view. Scale bars = 10  $\mu\text{m}$ .<sup>93</sup> Reprinted with permission from Hayashi *et al.*, PLoS ONE 10, 2 (2015). Copyright 2015 Authors, licensed under a Creative Commons Attribution (CC BY) License.

Subsequently, C2C13 myotubes were tested using this thermometry (Fig. 31). The authors also managed to monitor changes in heat production by myotubes after the addition of 1 mM caffeine—the luminescence lifetime of ER thermo yellow shortened after adding caffeine and after 10 min it returned to its previous state. The temperature sensitivity of the fluorescence lifetime of ER thermo yellow was between  $-24$  and  $-26$  ps per  $1^\circ\text{C}$  in living cells regardless of cell types. Moreover, the thermo yellow insensitivity to changes of pH and ionic strength was found. In addition, calibration curves in live and fixed cells were similar, which suggested the insensitivity to the viscosity of the cellular environment.

As mentioned in Sec. IV C, the extensive research on the zebrafish carried out by Chen *et al.* included also an analysis of decay times

to determine the temperature.<sup>109</sup> Using the fluorescence lifetime approach, the unwanted autofluorescence occurring for LIR based thermometers was eliminated. Figure 32 shows the FLIM image of the zebrafish larva at two temperatures: 22 and 28 °C. With the temperature increase from 22 to 28 °C,  $\text{Ir}^{3+}$  luminescence lifetime also increased from 321.3 ns to 447.5 ns. The lifetime of the excited level at  $482 \pm 35$  nm was analyzed in two temporal ranges: 0–2000 ns (pictures 1 and 2) and 150–2000 ns (pictures 3 and 4). By the selection of photons with a lifetime shorter than 150 ns (gate 0–150 nm), the autofluorescence from the yolk sac and belly of the fish was eliminated. Time resolved luminescence imaging using a polymer with attached iridium complexes, due to a good reversibility during heating-cooling processes, biocompatibility, independence on particle concentration,

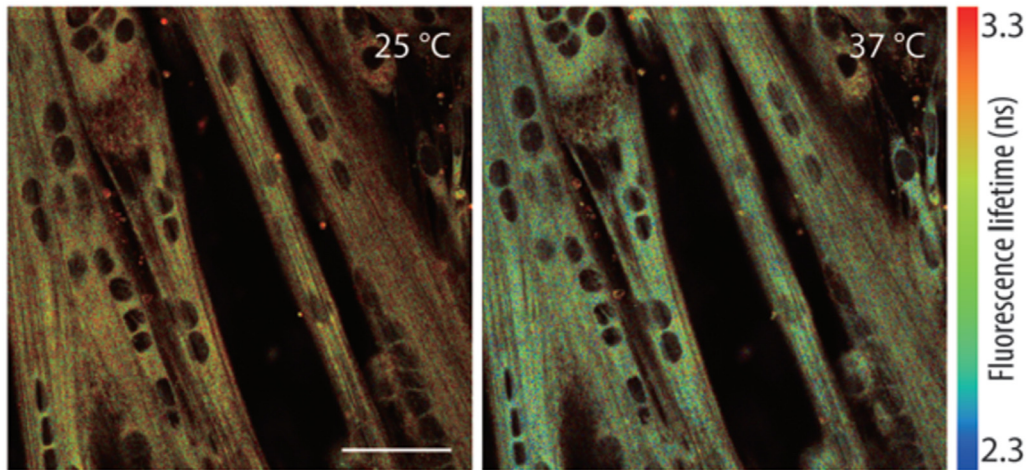


**FIG. 31.** Frequency-domain FLIM imaging of temperature. FLIM of ER thermos yellow in living C2C13 myotubes at 25 and 37 °C. Scale bar 50  $\mu\text{m}$ .<sup>128</sup> Reproduced with permission from Itoh *et al.*, *Chem. Commun.* **52**, 4458 (2016). Copyright 2016 Authors, licensed under a Creative Commons Attribution (CC BY) License.

pH values (4–10) and ionic strength and no autofluorescence effect made them a very promising tool for *in vivo* research, however it also revealed a disadvantage, namely, due to the lifetime of the order of ns, the pulses on the pico or femtosecond scale are needed for the excitation, therefore, the detection costs increase.

The lifetime approach using an acryl-based polymer thermometer with both  $\text{Ir}^{3+}$  and  $\text{Eu}^{3+}$  compounds was also studied.<sup>110</sup> As already mentioned (Sec. IV E), both the emission intensity and fluorescence lifetime of iridium compounds increased with increasing temperature, while  $\text{Eu}^{3+}$  complex acted as a reference signal, due to the constant emission intensity and lifetime at temperature changes. Time resolved imaging of luminescence in zebrafish at different

temperatures was performed. At 25, 30 and 35 °C, the lifetime of  $\text{Eu}^{3+}$  ions remained unchanged, while the lifetime of blue emission at 480 increased from around 296 ns to 390 ns. The analysis of the long life times allowed to exclude the influence of short-term autofluorescence, improve the contrast of imaging, sensitivity as well as spatial and temporal resolution. It was proven to be a sensitive and reversible method of reading the temperature with a thermal resolution from 0.18 to 0.52 °C.

Among the works that considered fluorescence lifetime as a method to achieve *in vivo* thermal imaging under a microscope, one needs to mention the hybrid nanostructures utilized by Qiu *et al.*<sup>129</sup> Such a system consisted of PbS QDs (which, under the 865 nm excitation, exhibited a short lifetime temperature response UCL emission around 810 nm) and  $\text{Nd}^{3+}$ —sensitized  $\text{Tm}^{3+}$ —UCNPs (which exhibited a long lifetime reference UCL signal also around 810 nm). A new thermometric parameter was then defined as  $R = (I_{\text{SUM}} - I_{\text{TM}})/I_{\text{TM}}$ , where  $I_{\text{SUM}}$  was the real-time intensity and  $I_{\text{TM}}$  was the 20  $\mu\text{s}$  delayed time-resolved intensity. This approach improved the accuracy of *in vivo* temperature measurement, providing an uncertainty of 0.5 K. Its thermal sensitivity, on the other hand, was as high as  $5.6\% \text{ K}^{-1}$ . To verify the UCL-NCs' temperature monitoring ability, intratumoral temperature was checked without or with a 2 mm-pork covering after irradiation with an 865 nm laser ( $500 \text{ mW/cm}^2$ ) for 30 s. Although the intensity of both real-time and time-resolved imaging exhibited marked attenuation after covering with a 2 mm-pork tissue slice, the ratio showed little difference (Fig. 33). The calculated temperatures were 35.5 and 35.2 °C, respectively. However, the 2D mapping aspect of the presented images was not completely explored as the excitation seem to be very punctual. Nevertheless, we expect that, in the near future, this principle will be improved with the development of nanostructures that emit in BW-II or BW-III and that present a relatively long lifetime. Though recent applications of such nanostructures provided high-contrast lifetime multiplexing in biological tissues, up to the present date their thermal imaging potential has never been tested.

To study biological phenomena important for the field of neuroscience in mice brain tissues, Hoshi *et al.*<sup>130</sup> used the fluorescent

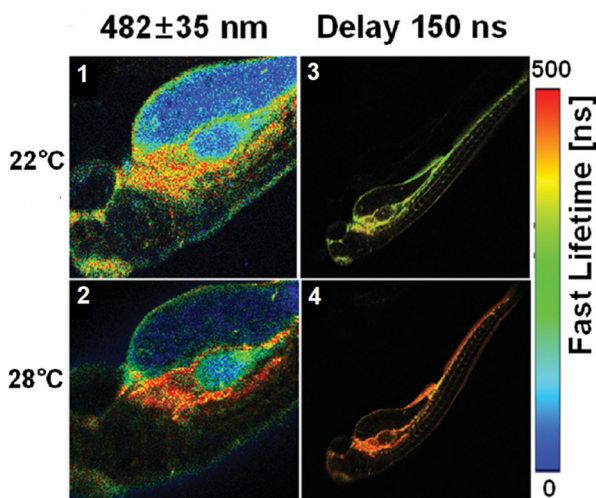


**FIG. 32.** The PLIM image of zebrafish larva at 22 and 28 °C. The lifetime of the excited level was analyzed in two ranges: 0–2000 ns (picture 1 and 2) and 150–2000 ns (picture 3 and 4).<sup>108</sup> Reprinted with permission from Chen *et al.*, *Adv. Funct. Mater.* **26**, 4386 (2016). Copyright 2016 John Wiley and Sons.

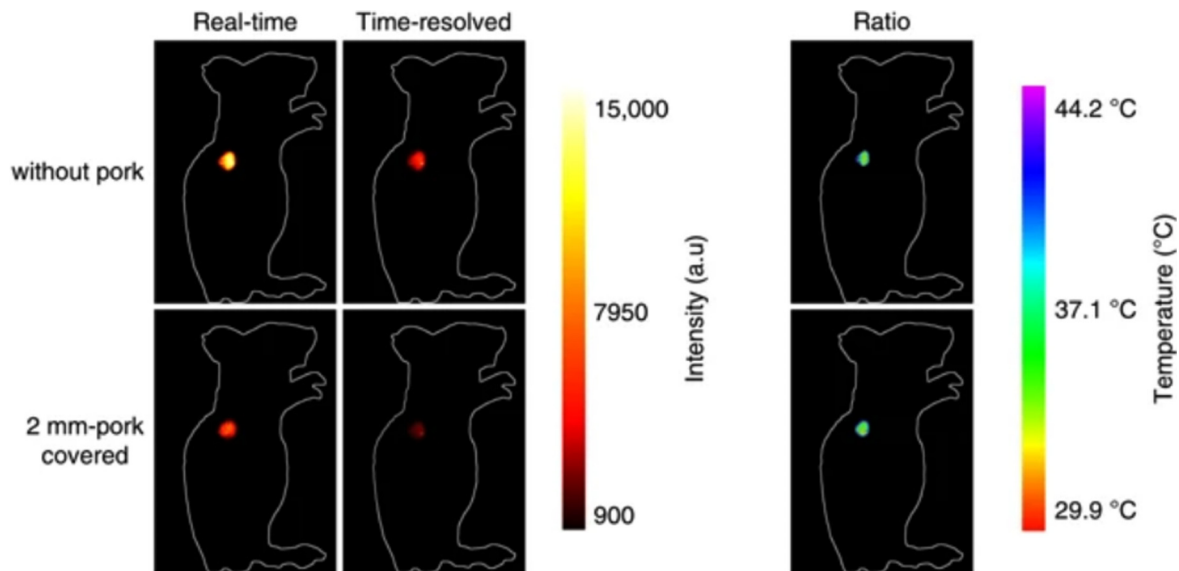


**FIG. 33.** Real-time, time-gated and ratio UCL imaging without or with a 2 mm-pork tissue slice covering *in vivo* under irradiation by a 865 nm laser ( $0.5 \text{ W cm}^{-2}$ ) for 30 s. The ratio imaging figure was obtained using image arithmetic [Ratio = (Real time – Time gated)/Time gated].<sup>129</sup> Reproduced with permission from Qiu *et al.*, Nat. Commun. 11, 4 (2020). Copyright 2020 Authors, licensed under a Creative Commons Attribution (CC BY) License.

polymer thermometer (FPT) previously described by the same authors,<sup>126</sup> which is now commercially available as a nanothermometer for measuring intracellular temperature using FLIM from Funakoshi (ultrasensitive fluorescent thermometer for cellular temperature monitoring—diffusive thermoprobe). The phenomenon of brain edema, during which the volume of the brain increases because the water content increases, has been studied. Ischemic edema was studied in model mice brain samples treated with oxygen-glucose deprivation (OGD). Edema pathology has been shown to be associated with thermosensitive cation channel TRPV4 (transient receptor potential vanilloid 4) activation, which is enhanced after elevated brain temperature, as demonstrated by tissue temperature imaging using FPT [Figs. 34(a)

and 34(b)]. OGD is associated with the release of glutamate also by the activation of glutamate receptors and TRPV4 receptors. Therefore, it has been checked that pharmacological blocking of glutamate receptors suppresses OGD-related temperature rise [Fig. 34(c)]. It was also confirmed that TRPV4 was involved in edema by testing in mice that lacked it. Thus, hyperthermia has been shown to cause TRPV4 activation and induces brain edema after ischemia. These studies can contribute to the development of ischemia intervention techniques that can help fight brain edema.

Kundu *et al.*<sup>131</sup> in 2019 described another luminescent nanothermometer utilizing the FLIM technique. For this purpose, gold nano-clusters 6-aza-2-thiothymine/l-arginine-stabilized Au NCs were used,

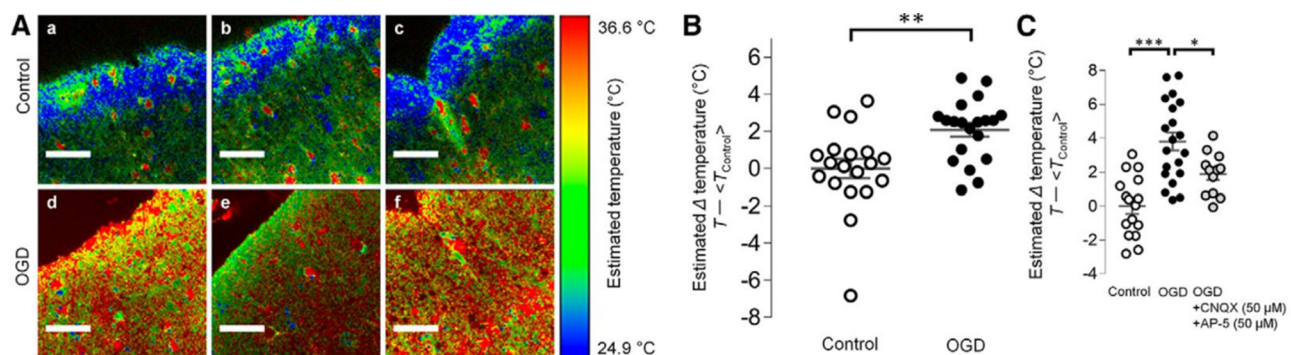


**FIG. 34.** The oxygen-glucose deprivation (OGD) treatment raises the intracellular temperature of brain slices via glutamatergic signaling. (a): Representative images of control [(a-A)–(a-C)] and OGD-treated [(a-D)–(a-F)] brain slices when the temperature of the perfusate was set at  $30^\circ\text{C}$ . Scale bars,  $50 \mu\text{m}$ ; (b): The temperature estimated by fluorescence lifetime of FPT was shown as difference between the temperature of each sample and the average of temperatures of control samples (estimated  $\Delta$  temperature, i.e.,  $T - T_{\text{Control}}$ ). The estimated  $\Delta$  temperature was significantly higher in the OGD group compared with control. The average difference of calculated intracellular temperature was  $2.12^\circ\text{C}$ ; (c): The OGD treatment significantly increased the estimated temperature of brain slices, a phenomenon blocked by co-applying the glutamate receptor antagonists CNQX ( $50 \mu\text{M}$ ) and AP-5 ( $50 \mu\text{M}$ ).<sup>130</sup> Reproduced with permission from Hoshi *et al.*, J. Neurosci. 38, 5700 (2018). Copyright 2018 Authors, licensed under a Creative Commons Attribution (CC BY) License.

showing variable optical properties as a function of temperature. Preliminary characterization of this nanothermometer revealed its advantages such as biocompatibility, photostability, facile cellular uptake and cytoplasm placement, emission with a maximum around 530 nm. Contrary to regular semiconductor quantum dots, only negligible changes in position or intensity of the absorption band for different temperatures in the tested range were observed. However, the emission intensity dropped by 84% in response to temperature increase from 15 to 55 °C. The average relative sensitivity ( $\Delta I/I_{\text{ref}}\Delta T$ ) was determined as  $-2.1\%/^{\circ}\text{C}$  in the whole range of tested temperatures, and  $-3.14\%/^{\circ}\text{C}$  for temperatures in the range 36–43 °C. The AuNCs were introduced into MG-63 cells and the temperature of the sample was altered. The FLIM images show the decrease in intensity of AuNCs emission inside cells proportionally to temperature increase and the histograms of lifetimes shifted to the shorter lifetimes as the temperature elevated. Unfortunately, although the authors note that the dynamics of the decay times change after changing the medium, i.e., after the introduction of AuNCs into the cells, no new calibration curve has been created.

## H. Emission bandwidth

The great potential advantage of using emission bandwidth (e.g., FWHM—full width half maximum) as an indicator of temperature is the fact the self-normalization occurs at single excitation and single emission bands. In practice, a single excitation band and two (narrow and broadband) bandpass filters have to be used to quantify the FWHM in the 2D image, where the pixel value corresponds to FWHM thermometric parameter. The potential disadvantages are related to the situations where the T probes emission overlap spectrally with the autofluorescence, due to the reabsorption of the thermometer reporter emission by its own absorption or due the internal filter effect (absorption of luminescence from temperature sensors by the compounds building the tissues, e.g., hemoglobin, collagen, elastin, water) may additionally affect the calibration of such thermometers. Variable spectral properties (e.g., oxygenated and deoxygenated blood) are especially troublesome for *in vivo* temperature mapping. *In vitro* experiments should be less susceptible to such artifacts. We are not aware of any *in vitro* or *in vivo* application of emission bandwidth for luminescence thermometry.

## I. Absorption edge shift

Temperature affects the absorption and emission properties of many luminescent nanomaterials. The temperature dependent changes in the absorption coefficient or the absorption edge shift will definitely translate to changes in luminescent properties—either luminescence intensity or spectra. These changes differ between particular materials and various mechanisms can be ascribed.

In lanthanides the narrowband absorption bands become thermally broadened due to electron–phonon coupling and temperature induced Stark components population. However the strongest various are observed in cryogenic temperatures. Temperature dependent charge-transfer band (CTB) edge shifts to longer wavelength, leading to enhanced excitation efficiency at a certain wavelength in the tail of the CTB. Under appropriate excitation wavelength, the luminescence intensity of the emitting ions (e.g., lanthanide or transition metals) will increase rapidly with temperature increasing. Temperature dependent

charge-transfer between vanadate ( $\text{VO}_4^{3-}$ ) group and  $\text{Sm}^{3+}$  or  $\text{Er}^{3+}$  lanthanide has been shown to be useful for temperature sensing with reasonable  $>2\%/^{\circ}\text{C}$  relative temperature sensitivity.<sup>132,133</sup> Because the CT bands are stronger than absorption bands of lanthanides themselves, this is a promising direction for achieving bright and sensitive thermometers. Alternatively, the temperature dependence of two intervalence charge transfer states (CTS) between  $\text{Tb}^{3+}$ ,  $\text{Pr}^{3+}$  in  $\text{NaGd}(\text{MoO}_4)_2$  were proposed and a maximal  $S_R$  value of  $2.05\%/^{\circ}\text{C}$  was obtained at 403 K.<sup>134</sup> A serious disadvantage is the fact, the CT bands are located in UV spectral region, which is not compatible with biomedical requirements, neither in terms of light absorption/scattering and safety reasons.

In transition metal complexes a *change* in electron distribution between the metal and a ligand gives rise to *charge transfer* (CT) bands, which is known to strongly depend not only on temperature, but also concentration, solvent polarity, etc. In some fluorescent molecules, like *N,N*-dimethyl-4-((2-methylquinolin-6-yl)ethynyl)aniline twisted-intramolecular-charge-transfer (TICT) induced emission, a positive temperature coefficient was demonstrated (rising fluorescence intensity with rising temperature), which was owing to activating vibrational bands of the TICT state, as compared to non-emissive de-excitation with a rise in temperature.<sup>135</sup> This system showed a ratio-metric temperature a sensing as well with sensitivity of c.a. 0.5%/C.

In quantum dots, the size not only determines the energy gap but also the absorption edge. Temperature can also efficiently change the electron–phonon interaction parameters<sup>84,136–138</sup> low-energy edge of the exciton absorption peak shifted toward higher energies as *temperature was* dropping with constant slope (i.e., linear relationship), which was explained by the interaction between excitons and longitudinal acoustic phonons.

Although there are experimental studies on using the above-mentioned effects for luminescence temperature determination, we are not aware of biomedical imaging using the spectral shifts of absorption edge of luminescent reporters. The fundamental problem with such methods originates from the fact that usually short wavelength absorption of these fluorophores overlap strongly with the absorption of various endogenous dyes and molecules. Moreover, short wavelength light is particularly susceptible to light scattering in highly heterogeneous tissues and cells, which hinders proper calibration and forces to perform this unavoidable step specifically for every sample to be studied.

## V. SUMMARY

Below, a summary of existing temperature imaging studies is presented for *in vitro* (Table III) and *in vivo* (Table IV) experiments. The reading method, sensitivities, artifacts and issues, heating methods, and additional information are provided in a comparative way.

## VI. OUTLOOK AND PERSPECTIVES

Although temperature imaging is a well-established technology and advanced T imagers (i.e., bolometric cameras) are commercially available, this technology is only suitable to image the temperature of the surface of objects. Such technology is sufficient for industrial (e.g., thermal hot spot detection in electronic circuits or mechanical devices, thermomodernization of buildings, etc.), military or security (e.g., noctovision, border inspection, etc.), and limited medical applications (e.g., diabetes foot monitoring, breast cancer screening, remote fever

**TABLE III.** Comparison of *in vitro* T imaging studies. The relative sensitivity, when not explicitly calculated in the articles, was assessed by us using the provided experimental data (unless not available—NA). Abbreviations: PL—photoluminescence, CW—continuous-wave, QY—quantum yield, AF—autofluorescence of tissue, VIS—visible spectral range, FLIM—fluorescence lifetime imaging,  $S_R$ —relative sensitivity,  $S_A$ —absolute sensitivity, and AuNPs—gold nanoparticles.

Material	Cells	T imaging method	Mechanism behind T sensing	Artifacts	Relative sensitivity (%/°C)	Source of heat	Temperature calibration	Comments	Reference
CuNCs biosynthesized in cells	MDA-MB-231	PL intensity	Collision of molecules, quenching at higher T	Aggregation due to biosynthesis in cells	3.18	The temperature was adjusted using a heater	Linear dependence in 20–45 °C	The presence of the sensor was observed both in the cytoplasm and in the cell nucleus; however, the stronger emission from the cytoplasm was most likely associated with the enhancement of emission resulting from aggregation in this area because most CuNCs were created in the cytoplasm)	76
Europium (III) thenoyltri-fluoro-acetate (Eu-TTA)	Chinese hamster ovary (CHO) cell clusters	PL intensity	Molecular vibrations; emission quenching at higher T	Photobleaching, emission was also dependent on pH changes	NA	Acetylcholine chemical stimulation	NA	This sensor does not penetrate inside the cells, but is integrated in the liposomal membranes because it is hydrophobic	71
Nanogel consisting of a polyNIPAM polymer and a DBD-AA fluorophore	COS7 cells	PL intensity	Conformation of PolyNIPAM; quenching of the DBD-AA luminescence at low T by water molecules	Luminescent response of the sensor dependent on $[K^+]$	NA	External chemical stimulus	Based on fluorescence intensity of nanogel within a single COS7 cell and temperature	Independent on pH and presence of proteins. Sensors were unevenly distributed in the cytoplasm and did not pass to the nucleus.	72
L-DNA molecular beacon	HeLa cells	PL intensity	Conformational changes resulting in changes of donor-acceptor distance; FRET modulated luminescence signal	Very mild dependence on ionic strength (150–200 mM) and pH (6.8–7.4)	NA	Heating stage; 10-min irradiation with 808 nm beam	Fluorescence intensity at 20 °C as reference	Nontoxic; L-DNA is not a naturally occurring biological form (in contrast to the D-DNA), which makes it resistant to enzymatic degradation; high repeatability for changes between 20 and 50 °C	73
Eu-TTA dye embedded in the polymeric poly(methyl methacrylate) (PMMA) network	HeLa cells	PL intensity	Motility of endosomes/lysosomes; thermal acceleration of movement of monitored organelles		Absolute sensitivity was 2.2%/°C on average at T = 25 °C	1-s irradiation with 1455 nm infrared laser beam on the outside of the HeLa cells	NA	pH (4–10) and ionic strength (0–500 mM) do not affect the fluorescence intensity; the spatial and temperature resolutions are 5.3 nm and 0.3 °C, respectively; the photobleaching of the nanothermometer was corrected using a single exponential curve.	139
Poly-L-lysine-coated silica nanoparticles doped with a Ruthenium(II)tris(bipyridyl) (Ru(bpy) <sub>3</sub> <sup>2+</sup> ) (PLL-coated RSNPs) and gold nanorods	HepG2 cells	PL intensity	The triplet metal-to-ligand charge transfer (3MLCT) state from which electronic transition occurs is thermally deactivated through crossing to a near higher-lying metal-centered (3MC) level; emission quenching at higher T		−1.26 %/°C	CW 808-nm laser with an output power of ~0.44 W·cm <sup>−2</sup> ; longitudinal surface plasmon resonance absorption at ~808 nm of gold nanorods	Linear fitting of PL in the range of 20 to 49 °C under a 450-nm excitation	Biocompatible owing to poly-L-lysine coating; the outer silica layer reduces oxygen quenching	140

TABLE III. (Continued.)

Material	Cells	T imaging method	Mechanism behind T sensing	Artifacts	Relative sensitivity (%/°C)	Source of heat	Temperature calibration	Comments	Reference
NPs: (Fe <sub>3</sub> O <sub>4</sub> at SiO <sub>2</sub> at (pNIPAM-co-RhBITC)/Au)	HeLa cells	PL intensity	Thermally induced changes of the polymeric layer thickness; the distance between the dye and Au NPs (luminescence quencher)	The major limitation is that the sensors have to be incorporated into cells before they can sense the cellular temperature	-4.84 %/°C	Cell culture dish on a thermo-plate	Linear fitting of PL intensity acquired from HeLa cells as a function of the cellular temperature in a range (from 26 to 41 °C)	Additional magnetic properties which affect the density of observed cells; the superparamagnetism of the nano-thermometer could provide a strong contrast effect; with the aid of an external magnetic field, the targeted temperature sensing can be achieved; ability to simultaneously realize magnetic field guided targeting and temperature sensing	141
ER thermo yellow dye (BDNCA346 compound ER targeting)	HeLa cells, skeletal muscle cells, Chang liver, 3T3, brown adipose tissue and C2C13 myotube	PL intensity	Non-radiative quenching	Thermosensitivity of a fluorescent molecule is affected by the rotational freedom of its substituent groups or by solvation, thus differ in various environments	3.9%/°C	Spot heating by focused IR laser 1064 nm (6 to 15 mW) on aluminum powders attached to the tip of a glass microneedle); or heterogeneous change in temperature produced by ionomycin (cytosolic [Ca <sup>2+</sup> ] ionophore)	A linear fitting of normalized PL intensity	The method revealed the dynamics of production of readily dissipated heat in real time at a subcellular level; the fluorescence intensity of ER thermo yellow was unaffected neither by [Ca <sup>2+</sup> ] nor pH changes within a physiological range (5.0–8.0); the average of the normalized fluorescence intensity was calculated from a total cell area with respect to each cell; Photobleaching was corrected by fitting to a single exponential curve	74
The copper nano-cluster (CuNCs)	MC3T3-E1 human cancer cells	PL intensity	Quenching due to molecule collision and the nonradiative quenching	High concentrations of CuNC are harmful to organisms; agglomeration of CuNC reduces PL intensity	NA	Heater stage	NA	The thermal quenching was fully reversible; good repeatability of the sensor in 15–70 °C range; good biocompatibility of the CuNCs for MC3T3-E1 cells; the presence of CuNCs was found both in the cytoplasm and in the cell nuclei, indicating the suitability of the CuNCs to cellular imaging	142
Mito thermo yellow (derivative of rosamines)	NIH3T3 cells, 3T3, HeLa, C2C13, Chang and mESC, BAT; multi-cellular spheroidal HeLa cells	PL intensity	T sensitivity depends on rotational freedom of the substituents	T sensitivity depends on the chemical environment (pH, viscosity, oxygen, etc.), thus no chance to obtain a universal calibration curve in the cellular environment	2.0–2.8%/°C depends cells being examined	1064 nm laser heating a glass microneedle with aluminum powders attached	The average intensity from the whole cell area and normalized in each cell (F/F <sub>0</sub> ) to the average of a whole cell area before heating (F <sub>0</sub> )	The sensitivity was independent of the dye concentrations	75
Hydrogel poly(NIPAM-co-BODIPY-AA)	BHK (Baby hamster kidney) cells	PL intensity	T induced changes in conformation of the polymer and therefore in the polarity	T sensitivity affected by BSA which modifies the polarity of the solvent	NA	Heating stage	The linear fitting of PL intensity of the hydrogel	The sensor showed no sensitivity to [K][Cl] ions nor pH; the reversibility of properties for cyclical changes between 37 and 47 °C; the sensor was present in the cytoplasm, but not in the cell nuclei	143



TABLE III. (Continued.)

Material	Cells	T imaging method	Mechanism behind T sensing	Artifacts	Relative sensitivity (%/°C)	Source of heat	Temperature calibration	Comments	Reference
ERthermAC dye	Mouse brown adipocytes cells (BAs) and human Bas	PL intensity	Non-radiative relaxation pathways by altering the structural dynamics of the ERthermAC molecule that, in turn, decreases its fluorescence intensity. reduction in ERthermAC; mitochondrial depolarization	Chemical and physical properties of environment impairs accuracy of T measurements	$-1.07\%/^{\circ}\text{C}$ (18.1–35.0 °C), and $-4.76\%/^{\circ}\text{C}$ (37–43 °C)	Isoproterenol (ISO)-stimulated and forskolin-stimulated heating due to increased mitochondrial respiration and glycolytic activity	<i>In situ</i> normalized PL intensity as a function of the measurement temperature in the 18–43 °C range	Physiological concentrations of $\text{Ca}^{2+}$ ions (10–1000 $\mu\text{M}$ ) do not affect the ERthermoAC activity, while the pH range of 7.0–8.1 changes its intensity to a small extent (–8.5%) compared to thermally activated intensity changes; only negligible bleaching under harsh conditions (continuous irradiation with high laser power at 543 nm)	77
Nitrogen-doped carbon dots (N-CQDs)	HepG2 cells	PL intensity	The mechanism is not explained	The temperature readout could be affected by $\text{Fe}^{3+}$ ions or cysteine presence	$0.52\%/^{\circ}\text{C}$	Homogenous; heater	The calibration curve obtained from PL intensity of N-CQDs dispersion against T-linear relationship with a high coefficient of 0.9874	Sensor of $\text{Fe}^{3+}$ ions presence, cysteine presence and temperature changes in cells; reversibility in heating-cooling cycles in the range of 20–40 °C	78
Carbon dots doped with nitrogen (N-CDs)	HeLa cells	PL intensity	The surface functional groups (–C = 0, –NH <sub>2</sub> , –OH, etc.) and the breaking of hydrogen bonds at higher temperatures affect the hydrodynamic radius of the particles	Some of the absorbed energy can be converted into heat	$-0.85\%/^{\circ}\text{C}$	Homogenous; heater	Linear fitting of the dependence of $I/I_0$ on temperature, where $I_0 = 20^{\circ}\text{C}$	The reversibility and repeatability after heating-cooling process; practically no $I/I_0$ dependence on the concentration of N-CDs, strong stable emission at pH range from 1 to 9, for various ionic forces and stable in time	79
Nanometric PbS/CdS/ZnS quantum dots	Chicken breast tissue	PL intensity	Nonradiative de-excitation pathways, including phonon-assisted processes and energy transfer to surface states.	Changes in excitation light intensity or [QD] could be wrongly interpreted as T variations; overheating possible	$1\%/^{\circ}\text{C}$	808 nm laser followed by a non-radiative depopulation resulted in efficient light to heat conversion (~43%)	Linear fitting of PL intensity of PbS/CdS/ZnS QDs centered at 1270 nm normalized to the value at 20 °C as a function of T	Owing to the ZnS coating, which shields the deeper PbS core and the CdS shell from the environment, this material exhibits biocompatibility and low toxicity; the possibility of both heating and temperature reading; the emission band appearing in the area of the second optical window, allowing imaging at a greater penetration depth without the autofluorescence effect	80,81,144
CdSe QDs	HeLa cells	Spectral shift and PL intensity	Thermally induced variation of the bandgap energy, QYs, thermal expansion, emission redshift with increasing temperature	Uneven distribution of NTs made T mapping inaccurate;	Coefficient of T $0.16\text{ nm}/^{\circ}\text{C}$ ; no information about S	Externally via a microair-heater	The integrated PL intensity and peak wavelength investigated as a function of temperature; calibration curves obtained in the PBS	Two-photon excitation in NIR allows for a much higher sensitivity than for one-photon excitation; Two-photon excitation allows for the generation of visible luminescence under NIR illumination, offering additional advantages for bioimaging applications, such as minimization of autofluorescence, increase of penetration depths and reduction of laser induced tissue damage	85

TABLE III. (Continued.)

Material	Cells	T imaging method	Mechanism behind T sensing	Artifacts	Relative sensitivity (%/°C)	Source of heat	Temperature calibration	Comments	Reference
Quantum dots Qtracker 655 Cell Labeling Kit (Q25021MP, Invitrogen)	SH-SY5Y living cells (human derived neuronal cell line)	Spectral shift and luminescence intensity ratio	Thermally induced changes of the electron–phonon coupling.	T dependent shift requires a spectrograph with a high resolution, which is too slow; photobleaching effect has to be included	0.105 nm/°C (spectral shift based method) Max.S <sub>R</sub> 6.3%/K (ratiometric method)	Via stage-top incubator	Measured in 30–42 °C temperature range and calibrated by the temperature dependent photobleaching curve	No significant size-dependent spectral shift	86
Genetically encoded tsGFP cell consisting of a green fluorescent protein (GFP) and a TlpA thermosensitive protein	HeLa cell; the mitochondria of brown adipocytes and the endoplasmic reticulum of myotubes.	Relative PL intensities under double excitation	The dimer to monomers conformation change of TlpA induced by temperature	tsGFPs do not exhibit T sensitivity below 35 °C <sup>101</sup>	NA	Heated perfusion tube	Linear dependence of the T dependent changes of PL intensity ( $I/I_0$ , 20 °C) excited at 480 nm	tsGFPs containing special sequences that allow targeting selected organelles (plasma membrane, ER and mitochondria); Temperature-dependent fluorescence changes were unaffected by Mg <sup>2+</sup> or Ca <sup>2+</sup> at physiological intracellular concentrations, pH changes (6.3–8.5), reductive and oxidative conditions	113
Semiconductor polymer dots (Pdots) and an attached thermosensitive dye, rhodamine B (Pdot-RhB nanoparticles)	HeLa cells	Relative PL intensities under single excitation	Efficient FRET energy transfer from the Pdot to the RhB (the donor emission overlaps with acceptor absorption)	Emission in the visible range affected by autofluorescence of tissues, therefore the penetration depth can be limited	1%/°C.	Heating stage	Linear fitting of the LIR of the red channel intensity (507–518 nm integration) to the green channel (571–582 nm integration) with the T (13.5 to 36.5 °C)	Ratiometric temperature reading in cells using PFBT-RhB was 13.2 ± 0.9 °C for the measured solution temperature of 13.5 °C (thermocouple error ± 0.5 °C) and 35.7 ± 1.8 °C for 36.5 °C, confirming good reliability of sensor temperature readout	90
Mixed polymers PNIPAm-co-NBDAA and PNIPAm-co-RhBAM (NBD—green dye, RhBAM—derivative of Rhodamine B)	HeLa cells	Relative PL intensities under single excitation	Temperature dependent hydrogen bonding ability of NBDAA dye	Very narrow useful T range; PL in VIS range can be affected by the AF of tissues	NA	Heating stage (heating rate was 1 °C/min:25–50 °C)	Linear dependence a calibration curve for PL intensity ratio on temperature in the 34.0–39.0 °C range	Both dyes were attached to the poly N-isopropylacrylamide (PNIPAm) polymer, but to separate chains to avoid an adverse FRET energy transfer in this case	91
DPTB covalently connected with PNIPAM nanogel (PNDP) and Nile Red (NR) dye freely distributed in the hydrophobic domains of the nanogel dye	NIL/3T3 cells	Relative PL intensities under single excitation	Thermally induced rearrangement of the fine structures in the polymer; efficient FRET energy transfer between DPTB and NR	Emission in the VIS range can be affected by AF	NA	Heating stage	Good linear relationship of the intensity ratio (470 nm/625 nm) with the temperature increase from 34 to 56 °C	Reading the temperature with such a system could be carried out even with the naked eye because the color of the emission changed from red to green-blue in the range of 30–55 °C	92

TABLE III. (Continued.)

Material	Cells	T imaging method	Mechanism behind T sensing	Artifacts	Relative sensitivity (%/°C)	Source of heat	Temperature calibration	Comments	Reference
Polymer NNPAM combined with APTMA, DBthD-AA and BODIPY-AA	MOLT-4 cells and HEK293T cells	Relative PL intensities under single excitation	T induced shape changes of NNPAM unit resulting in the release of the water molecules which quench fluorescent unit DBThD-AA	Thermal images of cells were not shown, only the graphs created on their basis were analyzed	4.1%/°C	Cage incubation chamber	A calibration curve was obtained using polystyrene standards, and 1-methyl-2-pyrroli-dinone containing LiBr (5 mM) was used as the eluent	The APTMA unit supports spontaneous internalization of molecules by living cells and prevents aggregation. DBThD-AA unit reveals temperature-dependent emission intensity and BODIPY-AA unit provides a reference signal; a temperature difference of about 1 °C was also observed between the nucleus and the cytoplasm for HEK293T cells. ratiometric method enabled 1 frame/s rate, using FLIM led to 1 frame/min	94
PEG- <i>b</i> -P(NIPAM- <i>co</i> -CMA), PEG- <i>b</i> -P(NIPAM- <i>co</i> -NBDAA), and PEG- <i>b</i> -P(NIPAM- <i>co</i> -RhBEA)	HepG2 cells	Relative PL intensities under single excitation	Cascade fluorescence resonance energy transfer (FRET); NIPAM polymer altered its conformation from the open at low T to shrank at high T enabling effective FRET between the mixed dye-labeled components	NA	<1 °C (34.2–40.5 °C)	Heating stage and heat generation within living cells upon glucose treatment	The calibration curve was obtained in the cell extract before	Regular (one step) FRET for pairs of dyes was examined, but the best results in temperature readout were obtained for a cascade FRET using three dyes mixed in the optimized proportions; great reversibility; nontoxic for HepG2 cells	95
polymer–TfAuNCs sensor- NBDAA fluorescent dye, a temperature-sensitive polymer (NIPAm), and an NSVB monomer + gold nanoclusters (TfAuNCs)	HeLa cells	Relative PL intensities under single excitation	Changes in the NIPAm polymer conformation (increase in emission intensity for temperature increase)	Plat 545 nm can be affected by tissues AF	NA	Cellular heat production following calcium ions stress by the ionomycin inducement (temperature increase 2 min after chemical stimulation)	The calibration curve obtained for whole cells from the intensity ratio 545/659 nm in the range of 31.8–38.5 °C showed a linearity with a coefficient of 0.973	The sensor's ability to measure temperature was checked using a single 488 nm excitation line and the PL intensity of NBDAA at 545 nm and of the TfAuNCs at 659 nm were observed; the polymer-TfAuNCs was found to be dispersed in the cytoplasm and there was no transfer to the cell nucleus	96
Nanohybrids composed of the carbon dots (CDs) and the gold nanoclusters (AuNCs)	293T cells	Relative PL intensities under single excitation	PL intensity of AuNCs is quenched at higher T due to the increase of the rate of non-radiative recombination of holes and electrons	The PL properties can be affected by quantum size effects or surface states	1.8%/°C	Homogenous, heater stage	Linear fitting of the emission intensity ratio ( $I_{430}/I_{605}$ ) vs the temperature	The CDs exhibit a tunable PL depending on the excitation line (for excitation in the 370–500 nm range, a shift of the emission peak from 456 to 550 nm can be observed); these NTMs were reproducible, insensitive to pH (range 4–9), ionic strength, presence of biomolecules as well as exposure to the Xe lamp; low cytotoxicity	97
Bovine serum albumin-stabilized gold nanoclusters (BSA–AuNCs) and fluorescein-5-	HeLa cells	Relative PL intensities under single excitation	PL intensity of AuNCs is strongly quenched at higher T due to the increase of the rate of non-radiative	PL as a function of T were measured at a constant pH = 9.0, the results can be	NA	Homogenous, heater stage	FITC/BSA–AuNCs intensity ratio reveal a good linear response	Simultaneous pH and temperature sensing due to the different quenching characters of the emission bands at 525 nm (FITC) and 670 nm (AuNCs); the ratiometric T	98

TABLE III. (Continued.)

Material	Cells	T imaging method	Mechanism behind T sensing	Artifacts	Relative sensitivity (%/°C)	Source of heat	Temperature calibration	Comments	Reference
isothiocyanate (FITC)			recombination of holes and electrons	affected if the pH will be changed				measurement is possible because AuNCs PL decreases with T, whereas the FITC emission can be used as a reference	
rhodamine (rhodamine B and rhodamine 110) dye-incorporated Pluronic F-127-melamine-formaldehyde (MF) composite polymer nanoparticles (R-F127-MF NPs)	HeLa cells	Relative PL intensities under single excitation	Nonradiative depopulation of Rhodamine B excited states	Photobleaching of fluorophores	$S_R$ NA; $S_A$ 4.9–15.4%/°C in the range 20–90 °C (7.6%/°C – 1 from –20 to 110 °C)	Cells heated with microwaves	The calibration curve was obtained by averaging the data on temperature-related PL intensity ratios of five samples	Owing to addition of second reference rhodamine 110 dye, the concentration dependence was excluded; good biocompatibility; good stability in solutions with varied pH, ionic strengths, and viscosities and have similar working curves in both intracellular and extracellular environments	99
Genetically encoded gTEMP with two fluorescent proteins (Sirius and mT-Sapphire dyes)	HeLa cells	Relative PL bands intensities under single excitation	At higher T fluctuation of an atom or molecule is amplified	Emission wavelength of both dyes is shifted by only 85 nm → spectral separation of PL bands may become an issue	2.6%/°C	IR 1462 nm laser was used to heat the cells; chemical stimulation by the addition of 10 μM FCCP	Extrapolation of the linear fitting curve of the PL intensity ratio of gTEMP expressed in HeLa cells in a temperature range from 30 to 40 °C controlled with a stage top incubator	Fluorescence ratio was calculated by dividing the mT-Sapphire intensity by the Sirius intensity within the region of interest; the insensitivity to the presence of $K^+$ , $Mg^{2+}$ and $Ca^{2+}$ ions and to pH variations was demonstrated; uniform expression in the cytoplasm and the nucleus; the fast response time of gTEMP (in the order of milliseconds); gTEMP is located directly in the mitochondria matrix	100
rhodamine B covalently bonded with carbon dots synthesized from bovine serum albumin proteins (CDs–RhB)	HeLa cells	Relative PL intensities under single excitation	The thermal quenching of Rhodamine B intensity	Overlap of emission bands occurs	NA	By heater stage, 5 °C was obtained with a refrigerator	By calculating ratio between PL ( $I_{586}/I_{482}$ ), a T dependent linear calibration curve from 5 to 50 °C	Two PLs at 482 and 586 nm were observed, which can be attributed to the CDs and the RhB emission, respectively; a low cellular translocation efficiency of this probe owing to the negative charge of the probe required surface modification	101
DNA nanomachine with molecular beacon on edges with attached FAM and TAMRA dyes	HeLa cells, HepG2 and L02 cell lines	Relative PL intensities under single excitation	T induced conformation changes of DNA tetrahedron shape; FRET between dyes	Useful T range = 27–50 °C, T > 55 °C could destroy the structure	5.2%/°C (30–50 °C)	Heating stage and using an NIR 980 nm laser [after adding gold nanowires (AuNRs)]	Averaged PL ratio from at least three cells vs T (five measuring points: 25, 29, 33, 37 and 40 °C)	Insensitivity to the presence of $K^+$ ions (up to 200 mM) and pH changes (6–8), changes in probe concentration; possess noncytotoxicity	102
Short single-stranded DNA (ssDNA) with attached FAM donor (D) and TAMRA acceptor (A)	PC-3 cells (human prostate cancer cell line)	Relative PL intensities under single excitation	T induced changes in the shape of the chain (from elongate to globular); FRET between dyes	Spectral bleed through between D and A may be affected by light scattering on cells	7.04%/°C (20–50 °C)	Heating stage	Almost linear dependence of the D/A ratio on temperature changes in the range of 0 – 100 °C	High biocompatibility and stability in various environments, invariable response in several heating and cooling cycles, invariability of sensory properties regardless of the nanoparticles concentration or excitation power	103

TABLE III. (Continued.)

Material	Cells	T imaging method	Mechanism behind T sensing	Artifacts	Relative sensitivity (%/°C)	Source of heat	Temperature calibration	Comments	Reference
Nd:LaF <sub>3</sub> NPs	Chicken breast	Relative PL intensities under single excitation	Thermal population of higher Stark components	Spectral overlap of 865 and 885 nm	0.25%/°C	Laser at 808 nm	A linear dependence of PL intensity ratio of the emission bands the biological T range	NPs capable of <i>in vivo</i> photothermal heating, luminescence tumor localization and intratumoral temperature determination; By choosing the appropriate, sufficiently high Nd ions concentration and excitation line, the simultaneous heating capacity and IR luminescence in the area of the optical window can be achieved; the value of relative sensitivity was almost unchanged in different environments (from water to mouse tissues)	81,104
poly N-n-propylacrylamide (PNNPAM) with attached iridium (III) complexes	HeLa cells	Relative PL intensities under single excitation	T induced changes in the polymer conformation from longitudinal to globular with T increase and breaking or creating of hydrogen bonds between polymeric amide bonds and water molecules when T changes	Dependence of thermal sensitivity on the environment	NA	Heating stage	Approximating the relationship between averaged LIR = $I_{470}/I_{590}$ (n = 9) and temperature to the sextuple polynomial	The ratios only depended on the temperature, and were independent of the dose of sensor, incubation time, or power of excitation laser	109
acrylamide-based polymer thermometer with iridium (III) and europium (III) compounds	HeLa cells	Relative PL intensities under single excitation	Thermal motions of the molecules; weakening of hydrogen bonds and thermal changes in the polarity of the microenvironment	There is a strong impact of AF	NA	Heating stage	Linear dependence of LIR = $I_{470}/I_{615}$ on temperature	Owing to the energy transfer, Ir compounds effectively performed the role of a sensitizer and easily expanded the excitation of the Eu (III) complex to the visible region; nontoxicity	110
Mito-RPT consist of two fluorescent dyes: Rhodamine B and CS NIR dye	HeLa cells	Relative PL intensity under two excitation bands	The rotation of diethylamino groups on the xanthene ring of Rhodamine B dye		-2.72 %/°C	A stage top incubator with four types of heaters (top cover, stage, water bath and lens heaters); thermogenesis induced by addition of FCCP in mitochondria	Obtained from the linear fit of the LIR = $(I_{756}/I_{587})$	PL intensity ratio did not change when the pH was varied (PH = 4–10) and the ionic strength (0–500 mM KCl) (stable fluorescence property against environmental parameters within the physiological range); no significant cytotoxicity; Mito-RTP was able to negate the effects of defocusing along the z-axis caused by cellular movements and concentration changes in the fluorophore	115
rhodamine B methyl ester (RhB-ME) and rhodamine 800 (Rh800)	Brown adipocytes (BA) cells, HeLa cells	Relative PL intensity under two excitation bands	Thermal quenching of RhB-ME emission at higher temperatures		NA	Chemical stimulation via 0.1 $\mu\text{mol/L}$ NE or 10 $\mu\text{mol/L}$ carbonyl cyanide m-chlorophenyl hydrazone (CCCP)	The fit of LIR = $I_{575-620}/I_{655-755}$ with Arrhenius equation	Visualization of HeLa cells showed that both dyes were located exactly in the same places (RhB-ME emission was observed in the red channel, Rh800 in the green channel); Both RhB-ME and Rh800 are insensitive to pH, Ca <sup>2+</sup> , or Mg <sup>2+</sup>	116

TABLE III. (Continued.)

Material	Cells	T imaging method	Mechanism behind T sensing	Artifacts	Relative sensitivity (%/°C)	Source of heat	Temperature calibration	Comments	Reference
Green fluorescent protein (GFP)	HeLa cells, U-89 MG cells	Fluorescence polarization anisotropy	Brownian motion causing random orientation of the molecular dipoles	For each complex, new calibration curves have to be determined photo-heating effect depends on the concentration and distribution of the AuNPs	No information	Cells heated with gold nanorods dispersed in a cell solution and heated with an IR laser	Obtained from the dependence of FPA on the temperature in the intracellular environment by heating the whole sample chamber	Homogeneous temperature distribution in transfected cells	117
poly(NNPAM-co-SPA-co-DBD-AA) with FPT (green) and MitoTracker Deep Red FM dyes	The COS7 cell, HeLa cell	Luminescence decay	T induced changes in the shape and therefore in the hydrophilicity of polymer; the water molecules are responsible for luminescence quenching		NA	Chemical-heat production by mitochondria after the addition of FCCP reagent	Fluorescence decay curve in each pixel was fitted with a double-exponential function; Calibration curve obtained from the COS7 cell extract (to obtain the conditions as close as possible to the environment of living COS7 cells).	The insensitivity to changes in ionic strength and pH in the range found in living cells was shown. Moreover the fluorescence lifetimes were proved to be insensitive to the differences in the FTP concentration, the presence of the proteins and viscosity; the temperature difference by about 0.96 °C between the cytoplasm and some cell elements were noted	126
Fluorescent gold nanoclusters (AuNCs)	HeLa cell	Luminescence decay		The lifetime of the order of ns requires pico or fs scale excitation pulses and increases the detection costs	0.5%/°C	Home-made temperature-controlled sample stage	Linear regression of the average fluorescence lifetime vs T; PL decay times were fitted with the sum of three exponentials with components: short (24 ns), medium (130 ns), and long (600–750 ns), which turned out to be the most dependent on temperature	The lifetime maps were created by fitting the decay curve obtained from each pixel; invariability to the local probe concentration or changes in fluorescence excitation conditions; the average lifetime of AuNCs at room temperature is more than 500 ns; that is, two orders of magnitude above the lifetime of cellular autofluorescence	127
polyNNPAM unit with an ionic unit SPA and a water-sensitive fluorescent unit DBThD-AA).	HeLa, NIH/3T3 and COS7 cells	Luminescence decay	T induced changes in the shape and therefore in the hydrophilicity of the polymer; luminescence quenching via water molecules	The lifetime of the order of ns requires pico or fs scale excitation pulses and increases the detection costs	7.01%/°C at 29 °C	Chemical stimulation with CCCP reagent induced heat production in the mitochondria	The calibration curve for the temperature imaging of HeLa cells was obtained by approximating the relationship between the averaged PL lifetime of the FPT in HeLa	Polymer exhibits stronger PL and longer PL lifetimes for increasing T	93

TABLE III. (Continued.)

Material	Cells	T imaging method	Mechanism behind T sensing	Artifacts	Relative sensitivity (%/°C)	Source of heat	Temperature calibration	Comments	Reference
ER thermo yellow and cytosolic mCherry sensor	HeLa cells and C2C13 myotubes	Luminescence decay		Lifetime in order of 1–2 ns requires shorter excitation pulses what induces the higher detection costs	–26 ps/°C (ER thermo yellow in HeLa) –14 ps/°C (mCherryin myotube)	Cia a stage top incubator; chemical stimulation using Ca <sup>2+</sup> shock with ionomycin and caffeine	cell extract (in triplicate) and the T to the sixth-degree polynomial; decay curves were fitted with a double-exponent in each pixel Fluorescence decay curves were fitted with double-exponents; the linear relationship (range: 23–40 °C) between T and the average lifetime of ER thermo yellow was obtained from about 25 HeLa cells and of cytosolic mCherry in living single C2C13 myotubes;	The frequency-domain FLIM method, which significantly reduces the time of image creation (up to 10 s) was used; temperature sensitivity of the fluorescence lifetime of ER thermo yellow was between –24 and –26 ps per 1 °C in living cells regardless of cell types; calibration curves in live and fixed cells were similar, and it suggests insensitivity to the viscosity of the cellular environment	128

TABLE IV. Comparison of *in vivo* T imaging studies. The relative sensitivity, when not explicitly calculated in the articles, was assessed by us using the provided experimental data (unless not available—NA). Abbreviations: PL—photoluminescence, CW—continuous-wave, QY—quantum yield, AF—autofluorescence of tissue, VIS—visible spectral range, FLIM—fluorescence lifetime imaging, S<sub>R</sub>—relative sensitivity, S<sub>A</sub>—absolute sensitivity, and AuNPs—gold nanoparticles.

Material	Cells	T imaging method	Mechanism behind T sensing	Artifacts	Relative sensitivity (%/°C)	Source of heat	Calibration	Comments and reference	Reference
Carbon dots doped with nitrogen (N-CDs)	The back of the mice	PL intensity	The surface functional groups (–C = 0, –NH <sub>2</sub> , –OH, etc.) and the breaking of hydrogen bonds at higher T affect the hydrodynamic radius of the particles.	400 nm excitation can be absorbed or scattered by tissue reducing the penetration depth	NA	NA	Linear fitting of the dependence of I/I <sub>0</sub> on temperature, where I <sub>0</sub> = 28 °C	Mice were anesthetized using isoflurane during imaging	79

TABLE IV. (Continued.)

Material	Cells	T imaging method	Mechanism behind T sensing	Artifacts	Relative sensitivity (%/°C)	Source of heat	Calibration	Comments and reference	Reference
Nanometric PbS/CdS/ZnS quantum dots	A431 cells (model human cell line—epidermal carcinoma) implanted subcutaneously into the flank of mice	PL intensity	Activation of different nonradiative de-excitation pathways, including phonon-assisted processes and energy transfer to surface states.	Changes in the excitation light intensity or QD concentration could hinder temperature readout;	1%/°C	808 nm light to heat conversion (~43%)	Linear fitting of emission intensity of the PbS/CdS/ZnS QDs centered at 1270 nm normalized to the value at 20 °C as a function of temperature	Owing to the outer ZnS coating, which shields the deeper PbS core and the CdS shell from the environment, this material exhibits biocompatibility and low toxicity; the possibility of both heating and temperature reading; the emission band appearing in the area of the second optical window, allowing imaging at a greater penetration depth without the autofluorescence effect; These intensity-based QD nanothermometers are very suitable for evaluating temperature variations in relatively short procedures in which no misleading concentration changes are expected to occur.	80,81,144
Nd:LaF <sub>3</sub>	Human breast cancer cells injected into mice	Relative PL bands intensities under single excitation	Thermal population of higher Stark components	Small spectral separation of bands; a calibration curve of Nd:LaF <sub>3</sub> NPs incorporated into tissues implies several technical problems, such as tissue drying and difficulty to obtain a homogeneous tissue temperature.	About 0.003%/°C	LaF <sub>3</sub> :5.6% Nd <sup>3+</sup> NPs with 808 nm line excitation	A linear dependence of the intensity ratio of bands at 865 and 885 nm on temperature in the biological temperature range	Lack of toxicity; human breast cancer cells were injected into both sides of mice and about two weeks after the injection, when the tumor reached 9 mm <sup>3</sup> , photothermal therapy was initiated. The LaF <sub>3</sub> :5.6%Nd <sup>3+</sup> nanoparticles were introduced into the area of one tumor, and the other tumor served as a reference; during <i>ex vivo</i> experiment the presence of NPs was noted in the scar and spleen, suggesting that the nanoparticles could partially leave the tumor area and enter the bloodstream, and eventually get to other organs of the body	81,104
Carbon-coated core-shell upconversion nanocomposite NaLuF <sub>4</sub> :Yb,Er at NaLuF <sub>4</sub> at Carbon (csUCNP at C)	HeLa cells incubated with csUCNP at C injected into mice	Relative PL bands intensities under single excitation	T sensitive upconversion; thermal population of higher levels according to Boltzmann distribution	Overheating; carbon layer can absorb the 980 nm excitation line and radiation emitted by the core of the nanoparticle. two different wavelengths to measure T and generate heat	1%/K (35–40 °C)	730 nm beam absorbed by carbon layer	Based on three measurements of UCL spectrum with different T changed by T controller and average values of I <sub>525</sub> /I <sub>545</sub> under different T were fitted	The un-doped NaLuF <sub>4</sub> layer (thickness 7.5 nm) between the carbon coat and the NaLuF <sub>4</sub> :Yb,Er core, improves the upconverted emission and prevents the luminescence quenching by the carbon shell; the lack of toxicity and of excessive heating of the environment and killing of healthy cells	105



TABLE IV. (Continued.)

Material	Cells	T imaging method	Mechanism behind T sensing	Artifacts	Relative sensitivity (%/°C)	Source of heat	Calibration	Comments and reference	Reference
Luminescent particles embedded in ultrathin, elastic and simple polymer nanosheets formed by EuDT and Rhodamine 800 dye.	The beetle <i>Dicronorrhina Derbyana</i>	Relative PL intensities under single excitation	T dependent probability of energy transfer rate between $\text{Eu}^{3+}$ (in EuDT) and the ligand molecule ( $\beta$ -diketonate)	This method only allows surface imaging	5.26%/°C at 37 °C	Heating with a 980 nm laser on H <sub>2</sub> O molecules (29–45 °C) and thermal changes caused by the work of dorsal muscles of the main flight muscle of <i>Dicronorrhina Derbyana</i>	PL intensity of EuDT-NS decreases practically linearly with T	Two excitation wavelengths: 405 and 640 nm, T was determined based on the EuDT PL intensity ratio at 620 nm vs 700 nm emission from Rodamine; due to absorption (640 nm) and emission (700 nm) in the red VIS range by Rodamine 800 and strong PL of EuDT, the contribution of AF is relatively small; The working mode of muscles was induced by mechanical stimulation, e.g., by gently touching the legs of the beetle with a stick; muscle temperature changes were not only imaged, but also filmed for the first time	106
Short single-stranded DNA (ssDNA) with attached ROX donor (D) and ATTO 647N acceptor (A)	PC-3 cells injected into mice's legs	Relative PL intensities under single excitation	T induced changes in the shape of the chain (from elongate to globular); FRET between dyes	T distribution is not clearly shown, and only the distribution of changes in the PL intensity of each phosphor separately is registered	NA	Microwave irradiation to heat tumor	Almost linear dependence of the D/A ratio on temperature changes in the range of 0 – 100 °C.	High biocompatibility and stability in various environments, invariable response in several heating and cooling cycles, invariability of sensory properties regardless of the nanoparticles concentration or excitation power; The ability to modulate the emission characteristics by means of appropriate matching of FRET phosphors, which have emission maxima at different wavelengths	103
poly N-n-propylacrylamide (PNNPAM) with attached iridium (III) complexes	Zebrafish larva	Relative PL intensities under single excitation  Luminescence decay	T induced changes in the polymer conformation from longitudinal to globular with T increase and breaking or creating of hydrogen bonds between polymeric amide bonds and water molecules	The strong AF impact; no obvious T induced increase of green and red PL due to lifetime in ns range, the detection costs increase and pulses on the pico or fs scale are needed for the excitation	Average $S = 6.82\%/^{\circ}\text{C}$ in the 12–40 °C temperature range  Average green $S_R = 3.44\%/^{\circ}\text{C}$ And red $S_R = 0.65\%/^{\circ}\text{C}$ in the 15–35 °C	Heating stage	Approximating the relationship between averaged $\text{LIR} = I_{470}/I_{590}$ (n = 9) and T to the sextuple polynomial from the double exponential decay fits	The luminescence was distributed in the whole of zebrafish larva, also in yolk sac and belly. Due to the reduction of photons with a lifetime shorter than 150 ns, autofluorescence from the yolk sac and belly of the zebrafish occurring for LIR based thermometers was eliminated.	109

TABLE IV. (Continued.)

Material	Cells	T imaging method	Mechanism behind T sensing	Artifacts	Relative sensitivity (%/°C)	Source of heat	Calibration	Comments and reference	Reference
acrylamide-based polymer thermometer with iridium (III) and europium (III) compounds	Zebrafish larva	Relative PL intensities under single excitation	T motions of molecules; weakening of hydrogen bonds and thermal changes in the polarity of the micro environment	Impact of AF	Average $S = 6.96\%/^{\circ}\text{C}$ in the 20–42 °C	Heating stage	Linear dependence of $LIR = I_{470}/I_{615}$ on temperature	Owing to the energy transfer, Ir compounds effectively performed the role of a sensitizer and easily expanded the excitation of the Eu (III) complex to the visible region; Good biocompatibility confirmed via adequate distribution of the polymer throughout the whole body 12 h after injection into the heart of a zebrafish.	110
		Luminescence decay		Due to the iridium complex lifetime of the order of ns, the detection costs increase and pulses on the pico or fs scale are needed for the excitation	Average $S = 2.8\%/^{\circ}\text{C}$ in the 20–40 °C temperature range		Linear relationship between lifetime and temperature of P–Ir–Eu in PBS solution with band-pass filter $480 \pm 40$ nm	The lifetime of AF in zebrafish was much shorter than the lifetime of the excited level of iridium compounds (several hundred nanoseconds) and shorter than much longer europium lifetime (several hundred $\mu\text{s}$ ). The analysis of long lifetimes allowed to exclude the influence of short-term AF, improve the contrast of imaging, sensitivity and spatial and temporal resolution.	
Green fluorescent protein (GFP)	nematode <i>Caenorhabditis elegans</i> ( <i>C. elegans</i> )	Fluorescence polarization anisotropy	Directly related to rotational diffusion induced by molecular Brownian motion	For each complex, new calibration curves have to be made; photoheating effect depends on the concentration and distribution of the AuNPs; slow temporal resolution	0.4%/°C for GFP attached to GAD proteins; 0.1%/°C in water	Photothermal heating in GNRs with the 800 nm laser	Linear dependence of FPA on temperature measured in each media	GFP can be bounded with selected enzymes found in only one cell type; the concentration of GFP used for imaging does not affect the measurement and the FPA is insensitive to fluctuations in the intensity of the excitation laser, photobleaching and sample migration; allows the imaging of thermal changes of individual neutrons	

detection on airports, etc.). The principle behind the bolometric camera operation relay on using 7–15  $\mu\text{m}$  emission and black-body radiation law. Due to the spectral detection range, neither below the skin surface nor of sub-cellular optical resolution (using optical microscopes) temperature mapping is nevertheless possible with present technologies. In the view of existing needs created by novel therapies (i.e., hyperthermia of cancer, targeted therapies, and temperature induced drug release) and to understand fundamental processes in biology (like thermogenesis and enzyme activity), in this review, we focused on summarizing current knowledge about remote imaging (i.e., 2D mapping) of temperature in biology and medicine using luminescent thermometry. Despite the fact that some examples of experimental biomedical T imaging can be found, most of the current research activities are dedicated to develop reliable T sensors using fluorescent molecules, proteins, polymers, and numerous inorganic nanoparticles. However, understanding how they work, how their spectroscopic properties depend on the microenvironment (pH, viscosity, pressure, etc.), and how sensitive they are teaches that performing reliable absolute temperature determination in 2D space is not a trivial task. The influence of the environment on T accuracy determination is not negligible, as not only chemical but also spectral properties of biological samples may affect spectral properties of the LNTs owing to the highly heterogeneous composition of the biological samples, sample autofluorescence, and light scattering, re-absorption by the sample and by the LT probes themselves. Such studies definitely require further attention and work.

As more and more reliable luminescence based temperature (nano)reporters are demonstrated and the luminescent (nano)thermometry matures, a transition from purely materials science and chemistry research to application driven technology requires comprehensive understanding and ranking of various materials; however, numerous reading methods have to be evaluated from various perspectives. Obviously, not only thermal relative sensitivity is a single figure of merit parameter, but other factors, such as the simplicity and cost-effectiveness, spatial and temporal resolution, 2D and 3D T determination capability *in vivo/in vitro*, background and artifact free detection, specificity of T detection, and simple data correction and analysis must be taken into account, when new versatile technology is to be developed.

The comparative analysis presented in this review, which considers the advantages and drawbacks of each of the particular nine temperature readout approaches and thermographic material used, enables to enumerate the features of the model-based luminescent thermometers. Temperature variable luminescence intensity is the simplest approach to temperature determination, but relative temperature changes may only be detected, and numerous artifacts, such as excitation intensity at the LT probes location, sample spectral properties on the way for excitation source to the LT probes and from LT probes to the detector may change to the absolute temperature being derived. Spectral band shift or bandwidth are relatively simple to implement for visualization, both with spectral detectors or 2D cameras, but this detection method is susceptible to some artifacts which disturb the pure LT probes luminescence spectra shape, such as sample autofluorescence or LT probe emission reabsorption, thus extensive data correction may be necessary to get reliable absolute temperatures. The ratiometric luminescence approach was originally considered as most reliable, but in the course of the studies, it is now obvious the self-reabsorption and interaction with the sample

absorption or scattering may significantly change the outcome of the readings. Primary thermometry in this case is of some help, and selection of emission bands which are spectrally close to each other but all these new rules change the paradigms and require more detailed studies. Single emission ratiometric excitation gives some hope as a new temperature determination mechanism, in which only one emission band is studied under two excitation wavelengths. Such an approach allows us to speed up and simplify optical setups to acquire temperature maps, also offering Stokes emission (unlike many anti-Stokes upconverting nanothermometers) and positive temperature sensing coefficients (i.e., rising temperature increases the brightness). The artifacts that however must be considered to originate from the spectral transmittance of the sample at two distinct excitation wavelengths. From the presented analysis, it can be concluded that the most reliable technique of remote temperature sensing, which shows the smallest impact of the object itself on the detected temperature, is based on the kinetics of the excited state—i.e., luminescence lifetimes of the temperature probes. On the other hand, depending on the optically active luminescent material used, the considered lifetime may vary from sub-nanoseconds to tens of milliseconds. The shorter the luminescence lifetime, the more complicated and costly the equipment and brighter the probes must be to acquire sufficient number of photons to derive the temperature. Although commercial FLIM systems exist, the slow frame-rate and/or constricted field-of-view may limit the wider adoption of photo-unstable fluorescent molecular probes for this purpose. Therefore, lanthanides and transition metals, with their long sub-ms to ms luminescence lifetimes seem to be the optimal choice, but such reliable LT probes are still under construction.

The balance between these materials science and imaging capability technical aspects needs to be found depending on the application. Future work should be oriented to develop a nanosized temperature sensor that exhibits bright emission, high chemical, and mechanical stability without photobleaching effect. Additionally, the interactions between nanoparticles themselves (like energy diffusion or reabsorption) may lead to the erroneous temperature readout. Therefore, phosphors of large Stokes shift are especially desired from this perspective. The model-based LT should possess absorption and emission bands which overlaps with the optical biological windows (OBWs) spectral range in order to minimize the effect of object-thermometer interaction and to maximize the light penetration depth in the biological system. Last but not least, the spectroscopic properties of such an ideal photoluminescent sensor should be strongly susceptible to temperature changes providing high accuracy and precision of temperature determination. If all of these requirements are met by one thermometric phosphor, the dissemination of luminescence thermometry technology, as one of the most reliable and accurate methods of temperature determination *in vitro* and *in vivo* imaging, will become possible. In consequence, not only new information about the dynamics of the biological processes will be revealed but, above all, the effectiveness of a new targeted therapies will be enhanced above the extent, which enables their wide and commercial use.

## ACKNOWLEDGMENTS

A.B. acknowledges the financial support from Grant No. 2017/27/B/ST7/01255 NCN OPUS 14. Ł.M., J.D., and K.T. acknowledge the financial support from Grant No. 2017/27/B/ST5/02557 NCN

OPUS 14. Financial support from NanoTBTech-H2020-FETOPEN (801305) “Nanoparticle-based 2D thermal bioimaging technologies” is greatly acknowledged. The work was supported by the Ministerio de Ciencia, Innovación y Universidades (No. PID2019-106301RB-I00). E.X. is grateful for a Juan de la Cierva Formación scholarship (No. FJC2018-036734-I).

## NOMENCLATURE

CCD	charge coupled device
CMOS	complementary metal–oxide–semiconductor
CT	computer tomography
ET	energy transfer
FRET	Förster resonant energy transfer
MRI	magnetic resonance imaging
NIR	near infrared (i.e., light)
OCT	optical coherent tomography
PMT	photomultiplier
QD	quantum dot
USG	ultrasound imaging
Vis	visible (i.e., spectral range)

## DATA AVAILABILITY

Data sharing is not applicable to this article as no new data were created or analyzed in this study.

## REFERENCES

1. S. Tanev, W. Sun, J. Pond, V. V. Tuchin, and V. P. Zharov, *J. Biophotonics* **2**, 505 (2009).
2. Y. Li, X. Zhang, M. Zheng, S. Liu, and Z. Xie, *RSC Adv.* **6**, 54087 (2016).
3. D. Jin, P. Xi, B. Wang, L. Zhang, J. Enderlein, and A. M. van Oijen, *Nat. Methods* **15**, 415 (2018).
4. J. Estelrich, M. J. Sánchez-Martín, and M. A. Busquets, *Int. J. Nanomed.* **10**, 1727 (2015).
5. L. Cheng, J. Liu, X. Gu, H. Gong, X. Shi, T. Liu, C. Wang, X. Wang, G. Liu, H. Xing, W. Bu, B. Sun, and Z. Liu, *Adv. Mater.* **26**, 1886 (2014).
6. R. Popovtzer, A. Agrawal, N. A. Kotov, A. Popovtzer, J. Balter, T. E. Carey, and R. Kopelman, *Nano Lett.* **8**, 4593 (2008).
7. J. M. Tucker-Schwartz, K. R. Beavers, W. W. Sit, A. T. Shah, C. L. Duvall, and M. C. Skala, *Biomed. Opt. Express* **5**, 1731 (2014).
8. J. Hartanto and J. V. Jokerst, in *Design and Applications of Nanoparticles in Biomedical Imaging*, edited by J. Bulte and M. Modo (Springer International Publishing, Cham, 2017), pp. 299–314.
9. J. H. Ryu, S. Lee, S. Son, S. H. Kim, J. F. Leary, K. Choi, and I. C. Kwon, *J. Controlled Release* **190**, 477 (2014).
10. P. K. Robinson, *Essays Biochem.* **59**, 1 (2015).
11. M. E. Ritchie, *Sci. Rep.* **8**, 11105 (2018).
12. G. Kucsko, P. C. Maurer, N. Y. Yao, M. Kubo, H. J. Noh, P. K. Lo, H. Park, and M. D. Lukin, *Nature* **500**, 54 (2013).
13. L. A. Sonna, J. Fujita, S. L. Gaffin, and C. M. Lilly, *J. Appl. Physiol.* **92**, 1725 (2002).
14. H. T. McMahon and E. Boucrot, *Nat. Rev. Mol. Cell Biol.* **12**, 517 (2011).
15. D. Chrétien, P. Bénil, H.-H. Ha, S. Keipert, R. El-Khoury, Y.-T. Chang, M. Jastroch, H. T. Jacobs, P. Rustin, and M. Rak, *PLoS Biol.* **16**, e2003992 (2018).
16. G. Baffou, H. Rigneault, D. Marguet, and L. Jullien, *Nat. Methods* **11**, 899 (2014).
17. S. Kiyonaka, R. Sakaguchi, I. Hamachi, T. Morii, T. Yoshizaki, and Y. Mori, *Nat. Methods* **12**, 801 (2015).
18. W. Liu and B. Yang, *Sens. Rev.* **27**(4), 298–309 (2007).
19. H. A. Khalid and K. Kontis, *Sensors* **8**, 5673 (2008).
20. L. D. Carlos and F. Palacio, *Thermometry at the Nanoscale: Techniques and Selected Applications* (The Royal Society of Chemistry, 2015), pp. 1–522.
21. A. Bednarkiewicz, L. Marciniak, L. D. Carlos, and D. Jaque, *Nanoscale* **12**, 14405 (2020).
22. J. Lifante, Y. Shen, E. Ximendes, E. M. Rodríguez, and D. H. Ortgies, *J. Appl. Phys.* **128**, 171101 (2020).
23. J. Zhou, B. del Rosal, D. Jaque, S. Uchiyama, and D. Jin, *Nat. Methods* **17**, 967 (2020).
24. R. Mout, D. F. Moyano, S. Rana, and V. M. Rotello, *Chem. Soc. Rev.* **41**, 2539 (2012).
25. F. Meiser, C. Cortez, and F. Caruso, *Angew. Chem. Int. Ed.* **43**, 5954 (2004).
26. A. Gnach and A. Bednarkiewicz, *Nano Today* **7**, 532 (2012).
27. L. Marciniak, K. Prorok, and A. Bednarkiewicz, *J. Mater. Chem. C* **5**, 7890 (2017).
28. A. Gnach, T. Lipinski, A. Bednarkiewicz, J. Rybka, and J. A. Capobianco, *Chem. Soc. Rev.* **44**, 1561 (2015).
29. X. Wang, O. S. Wolfbeis, and R. J. Meier, *Chem. Soc. Rev.* **42**, 7834 (2013).
30. F. Vetrone, R. Naccache, A. Zamarrón, A. J. De La Fuente, F. Sanz-Rodríguez, L. M. Maestro, E. M. Rodríguez, D. Jaque, J. G. Sole, and J. A. Capobianco, *ACS Nano* **4**, 3254 (2010).
31. S. Uchiyama and C. Gota, *Rev. Anal. Chem.* **36**, 20160021 (2017).
32. E. Wysokińska, J. Cichos, A. Kowalczyk, M. Karbowiak, L. Strzadala, A. Bednarkiewicz, and W. Kałas, *Biomolecules* **9**, 14 (2019).
33. E. Hemmer, P. Acosta-Mora, J. Méndez-Ramos, and S. Fischer, *J. Mater. Chem. B* **5**, 4365 (2017).
34. T. M. Liu, J. Conde, T. Lipiński, A. Bednarkiewicz, and C. C. Huang, *NPG Asia Mater.* **8**, e295 (2016).
35. R. Arppe, I. Hyppänen, N. Perälä, R. Peltomaa, M. Kaiser, C. Würth, S. Christ, U. Resch-Genger, M. Schäferling, and T. Soukka, *Nanoscale* **7**, 11746 (2015).
36. S. Fischer, N. D. Bronstein, J. K. Swabeck, E. M. Chan, and A. P. Alivisatos, *Nano Lett.* **16**, 7241 (2016).
37. H. D. A. Santos, I. Zabala Gutiérrez, Y. Shen, J. Lifante, E. Ximendes, M. Laurenti, D. Méndez-González, S. Melle, O. G. Calderón, E. López Cabarcos, N. Fernández, I. Chaves-Coira, D. Lucena-Agell, L. Monge, M. D. Mackenzie, J. Marqués-Hueso, C. M. S. Jones, C. Jacinto, B. del Rosal, A. K. Kar, J. Rubio-Retama, and D. Jaque, *Nat. Commun.* **11**, 2933 (2020).
38. M. Tan, B. del Rosal, Y. Zhang, E. Martín Rodríguez, J. Hu, Z. Zhou, R. Fan, D. H. Ortgies, N. Fernández, I. Chaves-Coira, A. Núñez, D. Jaque, and G. Chen, *Nanoscale* **10**, 17771 (2018).
39. D. J. Naczynski, M. C. Tan, M. Zevon, B. Wall, J. Kohl, A. Kulesa, S. Chen, C. M. Roth, R. E. Riman, and P. V. Moghe, *Nat. Commun.* **4**, 2199 (2013).
40. Y. Fan and F. Zhang, *Adv. Opt. Mater.* **7**, 1801417 (2019).
41. G. Hong, S. Diao, J. Chang, A. L. Antaris, C. Chen, B. Zhang, S. Zhao, D. N. Atochin, P. L. Huang, K. I. Andreasson, C. J. Kuo, and H. Dai, *Nat. Photonics* **8**, 723 (2014).
42. S. Diao, G. Hong, A. L. Antaris, J. L. Blackburn, K. Cheng, Z. Cheng, and H. Dai, *Nano Res.* **8**, 3027 (2015).
43. M. Suta and A. Meijerink, *Adv. Theor. Simul.* **3**(12), 2000176 (2020).
44. M. M. Hossain, G. Lu, and Y. Yan, in *Proceedings of the IEEE International Instrumentation and Measurement Technology Conference, 2012*, pp. 1856–1860.
45. M. Dramićanin, in *Woodhead Publishing Series in Electronic and Optical Materials*, edited by M. B. T.-L. T. Dramićanin (Woodhead Publishing, 2018), pp. 215–233.
46. S. W. Allison and G. T. Gillies, *Rev. Sci. Instrum.* **68**, 2615 (1997).
47. J. M. Bohlen and G. M. Beal, *Spec. Rep.* **18**, 56 (1957), available at <https://age-consearch.umn.edu/record/17351/files/ar560111.pdf>.
48. L. Labrador-Páez, M. Pedroni, A. Speghini, J. García-Solé, P. Haro-González, and D. Jaque, *Nanoscale* **10**, 22319 (2018).
49. D. Jaque and F. Vetrone, *Nanoscale* **4**, 4301 (2012).
50. C. D. S. Brites, P. P. Lima, N. J. O. Silva, A. Millán, V. S. Amaral, F. Palacio, and L. D. Carlos, *Nanoscale* **4**, 4799 (2012).
51. C. D. S. Brites, A. Millán, and L. D. Carlos, *Handb. Phys. Chem. Rare Earths* **49**, 339 (2016).
52. M. Dramićanin, *Luminescence Thermometry: Methods, Materials and Applications* (Woodhead Publishing, Elsevier, 2018).
53. C. Abram, B. Fond, and F. Beyrau, *Prog. Energy Combust. Sci.* **64**, 93 (2018).

- <sup>54</sup>M. Suta, Ž. Antić, V. Đorđević, S. Kuzman, M. D. Dramićanin, and A. Meijerink, *Nanomaterials* **10**, 543 (2020).
- <sup>55</sup>R. R. Anderson and J. A. Parrish, *J. Invest. Dermatol.* **77**, 13 (1981).
- <sup>56</sup>S. L. Jacques, *Phys. Med. Biol.* **58**, R37 (2013).
- <sup>57</sup>J. Drabik and L. Marciniak, *ACS Appl. Nano Mater.* **3**(4), 3798–3806 (2020).
- <sup>58</sup>J. Drabik, R. Kowalski, and L. Marciniak, *Sci. Rep.* **10**, 11190 (2020).
- <sup>59</sup>L. Marciniak and A. Bednarkiewicz, *Phys. Chem. Chem. Phys.* **18**, 15584 (2016).
- <sup>60</sup>T. P. van Swieten, D. Yu, T. Yu, S. J. W. Vonk, M. Suta, Q. Zhang, A. Meijerink, and F. T. Rabouw, *Adv. Opt. Mater.* **9**, 2001518 (2021).
- <sup>61</sup>H. H. Pennes, *J. Appl. Physiol.* **85**, 5 (1998).
- <sup>62</sup>S. A. Sapareto and W. C. Dewey, *Int. J. Radiat. Oncol. Biol. Phys.* **10**, 787 (1984).
- <sup>63</sup>V. Periyasamy and M. Pramanik, *IEEE Rev. Biomed. Eng.* **10**, 122 (2017).
- <sup>64</sup>A. Sassaroli, C. Blumetti, F. Martelli, L. Alianelli, D. Contini, A. Ismaelli, and G. Zaccanti, *Appl. Opt.* **37**, 7392 (1998).
- <sup>65</sup>S. T. Flock, M. S. Patterson, B. C. Wilson, and D. R. Wyman, *IEEE Trans. Biomed. Eng.* **36**, 1162 (1989).
- <sup>66</sup>R. Agah, A. H. Gandjibakhche, M. Motamedi, R. Nossal, and R. F. Bonner, *IEEE Trans. Biomed. Eng.* **43**, 839 (1996).
- <sup>67</sup>Y. Shen, J. Lifante, N. Fernández, D. Jaque, and E. Ximendes, *ACS Nano* **14**, 4122 (2020).
- <sup>68</sup>Y. Shen, H. D. A. Santos, E. C. Ximendes, J. Lifante, A. Sanz-Portilla, L. Monge, N. Fernández, I. Chaves-Coira, C. Jacinto, C. D. S. Brites, L. D. Carlos, A. Benayas, M. C. Iglesias-de la Cruz, and D. Jaque, *Adv. Funct. Mater.* **30**, 2002730 (2020).
- <sup>69</sup>S. Balabhadra, M. L. Debasu, C. D. S. Brites, R. A. S. Ferreira, and L. D. Carlos, *J. Phys. Chem. C* **121**, 13962 (2017).
- <sup>70</sup>P. McCord Morse, H. Feshbach, and G. P. Harnwell, *Methods of Theoretical Physics, Part I* (McGraw-Hill, 1953).
- <sup>71</sup>O. Zohar, M. Ikeda, H. Shinagawa, H. Inoue, H. Nakamura, D. Elbaum, D. L. Alkon, and T. Yoshioka, *Biophys. J.* **74**, 82 (1998).
- <sup>72</sup>C. Gota, K. Okabe, T. Funatsu, Y. Harada, and S. Uchiyama, *J. Am. Chem. Soc.* **131**, 2766 (2009).
- <sup>73</sup>G. Ke, C. Wang, Y. Ge, N. Zheng, Z. Zhu, and C. J. Yang, *J. Am. Chem. Soc.* **134**, 18908 (2012).
- <sup>74</sup>S. Arai, S. C. Lee, D. Zhai, M. Suzuki, and Y. T. Chang, *Sci. Rep.* **4**, 2 (2014).
- <sup>75</sup>S. Arai, M. Suzuki, S.-J. Park, J. S. Yoo, L. Wang, N.-Y. Kang, H.-H. Ha, and Y.-T. Chang, *Chem. Commun.* **51**, 8044 (2015).
- <sup>76</sup>J. Ye, X. Dong, H. Jiang, and X. Wang, *J. Mater. Chem. B* **5**, 691 (2017).
- <sup>77</sup>R. Kriszt, S. Arai, H. Itoh, M. H. Lee, A. G. Goralczyk, X. M. Ang, A. M. Cypess, A. P. White, F. Shamsi, R. Xue, J. Y. Lee, S. C. Lee, Y. Hou, T. Kitaguchi, T. Sudhaharan, S. Ishiwata, E. B. Lane, Y. T. Chang, Y. H. Tseng, M. Suzuki, and M. Raghunath, *Sci. Rep.* **7**(1), 1383 (2017).
- <sup>78</sup>M. Lu, Y. Duan, Y. Song, J. Tan, and L. Zhou, *J. Mol. Liquids* **269**, 766 (2018).
- <sup>79</sup>Y. Yang, W. Kong, H. Li, J. Liu, M. Yang, H. Huang, Y. Liu, Z. Wang, Z. Wang, T. K. Sham, J. Zhong, C. Wang, Z. Liu, S. T. Lee, and Z. Kang, *ACS Appl. Mater. Interfaces* **7**, 27324 (2015).
- <sup>80</sup>B. del Rosal, E. Carrasco, F. Ren, A. Benayas, F. Vetrone, F. Sanz-Rodríguez, D. Ma, Á. Juarranz, and D. Jaque, *Adv. Funct. Mater.* **26**, 6060 (2016).
- <sup>81</sup>B. del Rosal, E. Ximendes, U. Rocha, and D. Jaque, *Adv. Opt. Mater.* **5**, 1600508 (2017).
- <sup>82</sup>H. Zhang, W. Han, X. Cao, T. Gao, R. Jia, M. Liu, and W. Zeng, *Microchim. Acta* **186**, 1 (2019).
- <sup>83</sup>A. Narayanaswamy, L. F. Feiner, A. Meijerink, and P. J. van der Zaag, *ACS Nano* **3**, 2539 (2009).
- <sup>84</sup>Y. P. Varshni, *Physica* **34**, 149 (1967).
- <sup>85</sup>L. M. Maestro, E. M. Rodríguez, F. S. Rodríguez, M. C. I. De La Cruz, A. Juarranz, R. Nacache, F. Vetrone, D. Jaque, J. A. Capobianco, and J. G. Solé, *Nano Lett.* **10**, 5109 (2010).
- <sup>86</sup>R. Tanimoto, T. Hiraiwa, Y. Nakai, Y. Shindo, K. Oka, N. Hiroi, and A. Funahashi, *Sci. Rep.* **6**(1), 22071 (2016).
- <sup>87</sup>O. A. Savchuk, O. F. Silvestre, R. M. R. Adão, and J. B. Nieder, *Sci. Rep.* **9**(1), 7535 (2019).
- <sup>88</sup>Y. Su, X. S. Yao, Z. Li, Z. Meng, T. Liu, and L. Wang, *Biomed. Opt. Express* **6**, 500 (2015).
- <sup>89</sup>J. Laufer, R. Simpson, M. Kohl, M. Essenpreis, and M. Cope, *Phys. Med. Biol.* **43**, 2479 (1998).
- <sup>90</sup>F. Ye, C. Wu, Y. Jin, Y.-H. Chan, X. Zhang, and D. T. Chiu, *J. Am. Chem. Soc.* **133**, 8146 (2011).
- <sup>91</sup>J. Qiao, C. Chen, L. Qi, M. Liu, P. Dong, Q. Jiang, X. Yang, X. Mu, and L. Mao, *J. Mater. Chem. B* **2**, 7544 (2014).
- <sup>92</sup>J. Liu, X. Guo, R. Hu, J. Xu, S. Wang, S. Li, Y. Li, and G. Yang, *Anal. Chem.* **87**, 3694 (2015).
- <sup>93</sup>T. Hayashi, N. Fukuda, S. Uchiyama, and N. Inada, *PLOS One* **10**(2), e0117677 (2015).
- <sup>94</sup>S. Uchiyama, T. Tsuji, K. Ikado, A. Yoshida, K. Kawamoto, T. Hayashi, and N. Inada, *Analyst* **140**, 4498 (2015).
- <sup>95</sup>X. Hu, Y. Li, T. Liu, G. Zhang, and S. Liu, *ACS Appl. Mater. Interfaces* **7**, 15551 (2015).
- <sup>96</sup>J. Qiao, Y. H. Hwang, C. F. Chen, L. Qi, P. Dong, X. Y. Mu, and D. P. Kim, *Anal. Chem.* **87**, 10535 (2015).
- <sup>97</sup>C. Wang, H. Lin, Z. Xu, Y. Huang, M. G. Humphrey, and C. Zhang, *ACS Appl. Mater. Interfaces* **8**, 6621 (2016).
- <sup>98</sup>Y. T. Wu, C. Shanmugam, W. B. Tseng, M. M. Hiseh, and W. L. Tseng, *Nanoscale* **8**, 11210 (2016).
- <sup>99</sup>Y. Wu, J. Liu, J. Ma, Y. Liu, Y. Wang, and D. Wu, *ACS Appl. Mater. Interfaces* **8**, 14396 (2016).
- <sup>100</sup>M. Nakano, Y. Arai, I. Kotera, K. Okabe, Y. Kamei, and T. Nagai, *PLoS ONE* **12**, e0172344 (2017).
- <sup>101</sup>L. Wei, Y. Ma, X. Shi, Y. Wang, X. Su, C. Yu, S. Xiang, L. Xiao, and B. Chen, *J. Mater. Chem. B* **5**, 3383 (2017).
- <sup>102</sup>N. Xie, J. Huang, X. Yang, X. He, J. Liu, J. Huang, H. Fang, and K. Wang, *Anal. Chem.* **89**, 12115 (2017).
- <sup>103</sup>Y. Wu, J. Liu, Y. Wang, K. Li, L. Li, J. Xu, and D. Wu, *ACS Appl. Mater. Interfaces* **9**, 11073 (2017).
- <sup>104</sup>E. Carrasco, B. del Rosal, F. Sanz-Rodríguez, Á. J. de la Fuente, P. H. Gonzalez, U. Rocha, K. U. Kumar, C. Jacinto, J. G. Solé, and D. Jaque, *Adv. Funct. Mater.* **25**, 615 (2015).
- <sup>105</sup>X. Zhu, W. Feng, J. Chang, Y.-W. W. Tan, J. Li, M. Chen, Y. Sun, and F. Li, *Nat. Commun.* **7**, 10437 (2016).
- <sup>106</sup>T. Miyagawa, T. Fujie, Ferdinandus, T. T. Vo Doan, H. Sato, and S. Takeoka, *ACS Appl. Mater. Interfaces* **8**, 33377 (2016).
- <sup>107</sup>E. C. Ximendes, U. Rocha, T. O. Sales, N. Fernández, F. Sanz-Rodríguez, I. R. Martín, C. Jacinto, and D. Jaque, *Adv. Funct. Mater.* **27**, 1702249 (2017).
- <sup>108</sup>B. Struve and G. Huber, *Appl. Phys. B* **36**, 195 (1985).
- <sup>109</sup>Z. Chen, K. Y. Zhang, X. Tong, Y. Liu, C. Hu, S. Liu, Q. Yu, Q. Zhao, and W. Huang, *Adv. Funct. Mater.* **26**, 4386 (2016).
- <sup>110</sup>H. Zhang, J. Jiang, P. Gao, T. Yang, K. Y. Zhang, Z. Chen, S. Liu, W. Huang, and Q. Zhao, *ACS Appl. Mater. Interfaces* **10**, 17542 (2018).
- <sup>111</sup>J. Wang, A. Jiang, J. Wang, B. Song, and Y. He, *Faraday Discuss.* **222**, 122 (2020).
- <sup>112</sup>K. Trejgis, A. Bednarkiewicz, L. Marciniak, and Ł. Marciniak, *Nanoscale* **12**, 4667 (2020).
- <sup>113</sup>S. Kiyonaka, T. Kajimoto, R. Sakaguchi, D. Shinmi, M. Omatsu-Kanbe, H. Matsuura, H. Imamura, T. Yoshizaki, I. Hamachi, T. Morii, and Y. Mori, *Nat. Methods* **10**, 1232 (2013).
- <sup>114</sup>R. Piñol, J. Zeler, C. D. S. Brites, Y. Gu, P. Téllez, A. N. Carneiro Neto, T. E. da Silva, R. Moreno-Loshuertos, P. Fernandez-Silva, A. I. Gallego, L. Martínez-Lostao, A. Martínez, L. D. Carlos, and A. Millán, *Nano Lett.* **20**, 6466 (2020).
- <sup>115</sup>M. Homma, Y. Takei, A. Murata, T. Inoue, and S. Takeoka, *Chem. Commun.* **51**, 6194 (2015).
- <sup>116</sup>T.-R. Xie, C.-F. Liu, and J.-S. Kang, *Biophys. Rep.* **3**, 85 (2017).
- <sup>117</sup>J. S. Donner, S. A. Thompson, M. P. Kreuzer, G. Baffou, and R. Quidant, *Nano Lett.* **12**, 2107 (2012).
- <sup>118</sup>J. S. Donner, S. A. Thompson, C. Alonso-Ortega, J. Morales, L. G. Rico, S. I. C. O. Santos, and R. Quidant, *ACS Nano* **7**, 8666 (2013).
- <sup>119</sup>S. J. Remington, *Protein Sci.* **20**, 1509 (2011).
- <sup>120</sup>K. K. Sharman, A. Periasamy, H. Ashworth, and J. N. Demas, *Anal. Chem.* **71**, 947 (1999).
- <sup>121</sup>J. R. Lakowicz, *Principles of Fluorescence Spectroscopy* (Springer, Boston, MA, 2006), pp. 27–61.
- <sup>122</sup>C. Matuszewska, K. Elzbiaciak-Piecka, and L. Marciniak, *J. Phys. Chem. C* **123**, 18646 (2019).

- <sup>123</sup>K. Elzbiaciak, A. Bednarkiewicz, and L. Marciniak, *Sens. Actuators, B* **269**, 96 (2018).
- <sup>124</sup>K. Kniec, M. Tikhomirov, B. Pozniak, K. Ledwa, and L. Marciniak, *Nanomaterials* **10**, 189 (2020).
- <sup>125</sup>W. Piotrowski, K. Trejgis, K. Maciejewska, K. Ledwa, B. Fond, and L. Marciniak, *ACS Appl. Mater. Interfaces* **12**, 44039 (2020).
- <sup>126</sup>K. Okabe, N. Inada, C. Gota, Y. Harada, T. Funatsu, and S. Uchiyama, *Nat. Commun.* **3**, 705 (2012).
- <sup>127</sup>L. Shang, F. Stockmar, N. Azadfar, and G. U. Nienhaus, *Angew. Chem. Int. Ed.* **52**, 11154 (2013).
- <sup>128</sup>H. Itoh, S. Arai, T. Sudhaharan, S. C. Lee, Y. T. Chang, S. Ishiwata, M. Suzuki, and E. B. Lane, *Chem. Commun.* **52**, 4458 (2016).
- <sup>129</sup>X. Qiu, Q. Zhou, X. Zhu, Z. Wu, W. Feng, and F. Li, *Nat. Commun.* **11**, 4 (2020).
- <sup>130</sup>Y. Hoshi, K. Okabe, X. K. Shibasaki, X. T. Funatsu, N. Matsuki, X. Y. Ikegaya, and X. R. Koyama, *J. Neurosci.* **38**, 5700 (2018).
- <sup>131</sup>S. Kundu, D. Mukherjee, T. K. Maiti, and N. Sarkar, *ACS Appl. Bio Mater.* **2**, 2078 (2019).
- <sup>132</sup>S. Zhou, C. Duan, and S. Han, *Dalton Trans.* **47**, 1599 (2018).
- <sup>133</sup>S. Zhou, C. Duan, M. Yin, X. Liu, S. Han, S. Zhang, and X. Li, *Opt. Express* **26**, 27339 (2018).
- <sup>134</sup>Y. Gao, F. Huang, H. Lin, J. Zhou, J. Xu, and Y. Wang, *Adv. Funct. Mater.* **26**, 3139 (2016).
- <sup>135</sup>C. Cao, X. Liu, Q. Qiao, M. Zhao, W. Yin, D. Mao, H. Zhang, and Z. Xu, *Chem. Commun.* **50**, 15811 (2014).
- <sup>136</sup>I. A. Vainshtein, A. F. Zatsopin, and V. S. Kortov, *Phys. Solid State* **41**, 905 (1999).
- <sup>137</sup>K. P. O'Donnell and X. Chen, *Appl. Phys. Lett.* **58**, 2924 (1991).
- <sup>138</sup>S. S. Savchenko, A. S. Vokhmintsev, and I. A. Weinstein, *Opt. Mater. Express* **7**, 354 (2017).
- <sup>139</sup>K. Oyama, M. Takabayashi, Y. Takei, S. Arai, S. Takeoka, S. Ishiwata, and M. Suzuki, *Lab Chip* **12**, 1591 (2012).
- <sup>140</sup>L. Yang, H. S. Peng, H. Ding, F. T. You, L. L. Hou, and F. Teng, *Microchim. Acta* **181**, 743 (2014).
- <sup>141</sup>Z. Wang, X. Ma, S. Zong, Y. Wang, H. Chen, and Y. Cui, *Talanta* **131**, 259 (2014).
- <sup>142</sup>C. Wang, L. Ling, Y. Yao, and Q. Song, *Nano Res.* **8**, 1975 (2015).
- <sup>143</sup>D. Gong, T. Cao, S. C. Han, X. Zhu, A. Iqbal, W. Liu, W. Qin, and H. Guo, *Sens. Actuators, B* **252**, 577 (2017).
- <sup>144</sup>A. Benayas, F. Ren, E. Carrasco, V. Marzal, B. del Rosal, B. A. Gonfa, Á. Juarranz, F. Sanz-Rodríguez, D. Jaque, J. García-Solé, D. Ma, and F. Vetrone, *Adv. Funct. Mater.* **25**, 6650 (2015).